Formation of clathrate hydrates: An x-ray scattering study

Dissertation

zur Erlangung des Doktors der Naturwissensschaften
der Fakultät Physik der Technischen Universität Dortmund

vorgelegt von

Felix Lehmkühler

März 2010

Gewisse Bücher scheinen geschrieben zu sein, nicht damit man etwas daraus lerne, sondern damit man wisse, daß der Autor etwas gewußt hat.

Johann Wolfgang von Goethe,
Maximen und Reflexionen

Contents

List of Figures

1 Introduction

Clathrate hydrates are inclusion compounds where guest molecules are embedded in a hydrogen bonded water network.[1] As the majority of enclosed guests are gaseous at ambient pressure and temperature conditions, clathrate hydrates are usually referred to gas hydrates. In general, gas hydrates are stable at high pressures and low temperatures. Since their discovery in the beginning of the 19th century, hydrates were nearly forgotton until they were accounted for gas pipeline plugging in the 1930s.[2] Later, huge amounts of gas hydrate – mainly methane hydrate – were detected at the ocean floor. Up to now, estimations of the effective amount are quite inaccurate. However, mining of these gas deposits is suggested to contribute to the future energy supply.[3] In recent years, hydrates are discussed to act as gas storage material. Especially a save storage of carbon dioxide (CO_2), e.g. at the ocean floor, or hydrogen (H_2) for fuel cells are highly discussed.[4] For the latter, the addition of tetrahydrofuran (THF) was demonstrated to lower the hydrate's stability pressure so that industrially desirable conditions were obtained.

Although the structure of hydrates is comparable to conventional ice, both materials differ in many properties.[5] Here, especially the guest-host interaction between embedded guest molecules and the water molecules gives rise to such deviations. In particular, a very strong guest-host interaction in THF hydrate was recently suggested based on molecular dynamics simulation, yielding a distortion of the hydrate's structure.[6] Due to this behavior and its potential application in gas storage, THF hydrate is chosen as specimen in this work. This hydrate often acts as prototype for other hydrates because it can be produced easily and is stable at ambient conditions. However, macroscopic studies of thermodynamic properties of THF hydrate revealed an anomaly which was not found in other hydrates and was thought to be originated in a certain structural change.[7]

[1] Koh, C. A. (2002). *Chem. Soc. Rev.* **31**, 157; Sloan, E.D. (2003). *Nature* **426**, 353.

[2] Hammerschmidt, E.G. (1934). *Industrial and Engeneering Chemistry* **26**, 851.

[3] Max, M. D., ed. (2000). *Natural Gas Hydrates in Oceanic and Permafrost Environments*. Kluwer Academic Publishers; Sloan, E.D. and Koh, C.A. (2008). *Clathrate Hydrates of Natural Gases*. 3rd ed. CRC Press Inc.; Schicks, J. (2008). *Chem. Unserer Zeit* **42**, 310.

[4] Brewer, P.G. et al. (1999). *Science* **284**, 943; Florusse, L.J. et al. (2004). *Science* **306**, 469; Lee, H. et al. (2005). *Nature* **434**, 743.

[5] For an overview see Sloan, E.D. and Koh, C.A. (2008). *Clathrate Hydrates of Natural Gases*. 3rd ed. CRC Press Inc.

[6] Alavi, S. et al. (2009). *J. Chem. Phys.* **130**, 174501.

[7] Leaist, D.G. et al. (1982). *J. Phys. Chem.* **86**, 4175; Waite, W.F. et al. (2005). *Proceedings of the Fifth International*

The thermodynamics of the gas hydrate formation process are well understood for more than 50 years,[8] and can be used accurately for calculating hydrate stability regions.[9] While being the topic of many experimental and computational studies,[10] the formation of hydrates on molecular length scales is not fully understood up to now. In particular, the role of the guest molecules and the structural configuration of the water molecules during and before the nucleation is controversially discussed. A deeper understanding of this process may help to tune hydrates for technological applications, such as gas storage, or may help to inhibit the growth of hydrates in pipelines. In literature, different formation models are presented, mainly based on molecular dynamics simulation.[11] Parts of these models predict the formation of hydrate precursor clusters while other interpret hydrate formation as a stochastic process without precursors. However, an experimental proof is missing.

In this thesis the hydrate formation process is studied experimentally with various x-ray scattering methods in order to favor one of these models. Therefore both, hydrate formation at the water-CO_2 interface and in the water-THF bulk mixture were studied in this work. Moreover, the study of THF hydrate at different temperatures offers the possibility to investigate the proposed structural distortion due to a strong guest-host interaction and its implications to the thermodynamic anomaly.

Since the formation of CO_2 hydrate occurs at the water-CO_2 interface, the structure of this interface is probed by x-ray reflectivity and x-ray diffraction measurements. X-ray reflectivity is a prominent tool to investigate structural properties of surfaces and interfaces.[12] It probes the electron density profile of the sample. Thus, surface and interface roughnesses and thicknesses of thin films can be measured. Owing to propagating capillary waves, liquid surfaces exhibit a surface roughness on the order of several Ångströms.[13] Furthermore, it has been demonstrated that x-ray reflectivity is feasible to investigate the properties and the formation of thin films at liquid-gas interfaces.[14] The formation of gas hydrates or hydrate precursors at interfaces would result in a rougher interface or a local change of electron density which thus will be accessible by x-ray reflectivity measurements. A new set-up design allows to perform x-

Conference on Gas Hydrates, 1725.

[8] van der Waals, J.H. and Platteeuw, J.C. (1959). *Adv. Chem. Phys.* **2**, 1.

[9] Sloan, E.D. and Koh, C.A. (2008). *Clathrate Hydrates of Natural Gases*. 3rd ed. CRC Press Inc.

[10] See for an overview, e.g. Walsh, M.R. et al. (2009). *Science* **326**, 1095; Guo, G.-J. et al. (2008). *J. Chem. Phys.* **128**, 194504; Sloan, E.D. and Koh, C.A. (2008). *Clathrate Hydrates of Natural Gases*. 3rd ed. CRC Press Inc. and references therein.

[11] Radhakrishnan, R. and Trout, B.L. (2002). *J. Chem. Phys.* **117**, 1786; Sloan, E.D. and Koh, C.A. (2008). *Clathrate Hydrates of Natural Gases*. 3rd ed. CRC Press Inc.; Rodger, P.M. (1990). *J. Phys. Chem.* **94**, 6080; Kvamme, B. (2000). *Annals of the New York Academy of Science* **912**, 496; Guo, G.-J. et al. (2009). *Phys. Chem. Chem. Phys.* **11**, 10427.

[12] Tolan, M. (1999). *X-ray Scattering from Soft Matter Thin Films*. Springer.

[13] Braslau, A. et al. (1985). *Phys. Rev. Lett.* **54**, 114.

[14] See Paulus, M. et al. (2005). *Phys. Rev. E* **72**, 061601 and references therein.

ray reflectivity experiments on liquid surfaces and interfaces at high energy beamlines.[15] This offers the possibility to investigate deep buried interfaces or special sample environments such as high pressure sample cells. In particular, the formation of CO_2 hydrate at pressures up to 35 bar can be studied as done in the framework of this thesis. In addition, the liquid-liquid water-CO_2 interface is studied by means of x-ray diffraction in order to study the formation of CO_2 hydrate crystallites.

In contrast to CO_2, THF hydrate is formed from a liquid mixture of water and THF which requires bulk sensitive methods such as x-ray Raman and Compton scattering. Non-resonant inelastic x-ray scattering including both x-ray Raman (XRS) and Compton scattering yields information on the local structure on molecular length scales.[16] In the case of XRS, the fine structure of an absorption edge is investigated. The main advantage compared to conventional x-ray absorption spectroscopy is the free choice of incident energy.[17] Hence, absorption edges in the region of soft x-rays, e.g. the oxygen K-edge, can be studied bulk sensitively. It has been shown in the past years that this adsorption edge is sensitive to the coordination and local structure in water and ice.[18] In Compton scattering experiments, the projected momentum density of the electron system in its ground state is probed.[19] This technique is in particular sensitive to the bond geometry of the sample. Similar to XRS, a lot of studies were performed in recent years analyzing water and ice systems which demonstrated the feasibility of Compton scattering to study structural properties of hydrogen bonded samples.[20] Therefore, especially the formation of hydrate precursors in a bulk mixture of water and THF and a structural change in THF hydrate can be investigated probing both the short range order by Compton scattering and the short and intermediate range order by XRS. Moreover, Compton scattering allows to extract thermodynamic properties as e.g. the configurational heat capacity, and hence makes a direct measurement of the proposed thermodynamic anomaly possible.

The thesis is organized as follows:

- In **chapter 2** the properties of clathrate hydrates are presented. This includes a description of the different structures and guest molecules, the thermodynamics, and a short overview on potential applications of gas hydrates. The chapter closes with a presentation of the different proposed hydrate formation models and a summary of previous

[15] Reichert, H. et al. (2003). *Physica B* **336**, 46; Honkimäki, V. et al. (2006). *J. Synch. Rad.* **13**, 426.
[16] Schülke, W. (2007). *Electron Dynamics by Inelastic X-ray Scattering*. Oxford University Press.
[17] Sternemann, C. et al. (2008*a*). *J. Anal. At. Spectrom.* **23**, 807.
[18] Wernet, Ph. et al. (2004). *Science* **304**, 995; Cai, Y.Q. et al. (2005). *Phys. Rev. Lett.* **94**, 025502; Bergmann, U. et al. (2007*a*). *Phys. Rev. B* **76**, 024202; Tse, J.S. et al. (2008). *Phys. Rev. Lett.* **100**, 095502; Pylkkänen, T. et al. (2010). *J. Phys. Chem. B* **114**, 3804.
[19] Cooper, M.J. et al. (2004). *X-Ray Compton Scattering*. Oxford University Press.
[20] Isaacs, E.D. et al. (1999). *Phys. Rev. Lett.* **82**, 600; Hakala, M. et al. (2004). *Phys. Rev. B* **70**, 125413; Hakala, M. et al. (2006*a*). *Phys. Rev. B* **73**, 035432; Nygård, K. et al. (2006*a*). *Phys. Rev. E* **74**, 031503; Sit, P.H.-L. et al. (2007). *Phys. Rev. B* **76**, 245413; Nygård, K. et al. (2007*a*). *Phys. Rev. Lett.* **99**, 197401.

studies of hydrate formation.

- **Chapter 3** contains the study of CO_2 hydrate formation at the water-CO_2 interface. Therefore, the theoretical background of x-ray reflectivity and processes on liquid-gas interfaces are presented first. Afterwards, the experimental set-ups for reflectivity and diffraction measurements and the sample cells used in this thesis are described. At the end the experimental results are discussed with respect to the hydrate formation process.

- **Chapter 4** is dedicated to the study of the formation and properties of THF hydrate. At first the theory of non-resonant inelastic x-ray scattering is presented with special attention to x-ray Raman scattering and Compton scattering. To demonstrate the feasibility of the scattering technique studying such samples, an overview on recent experiments on water and ice systems is given. Subsequently, the experimental set-ups are demonstrated. Finally, the experimental results are presented and are compared to computed spectra.

- The concluding **chapter 5** summarizes the results of the thesis. Furthermore, an outlook on potential consecutive studies based on this thesis is given.

2 Clathrate hydrates

Beyond the 15 currently known crystalline[1] and three amorphous phases of ice,[2] water can form additional crystalline phases called clathrate hydrates in the presence of small molecules. These hydrates are non-stoichiometric, ice-like inclusion compounds where guest molecules – mainly gases – are trapped in a water nano-cage network. Clathrate hydrates without guest do not exist, the interaction between water molecules and guest stabilizes the cage network.

During the past years hydrates have reached the focus of a general audience due to a rising number of possible applications, e.g. the storage of gases in hydrates. For these applications, a fundamental knowledge of the hydrate formation process is essential in order to inhibit or initiate the formation of hydrates.

In this chapter the different hydrate structures and guests are presented in section 2.1, followed by a summary of different applications for hydrates in section 2.2. The last section 2.3 deals with the formation of hydrates, including both an overview of the thermodynamical model of hydrate formation and the microscopic models describing the molecular arrangements leading to the nucleation of hydrates.

2.1 Structures and stability

The term clathrate describes a system of at least two different types of molecules or atoms where one forms a lattice in which the other one is trapped. In the case of hydrates water molecules form a lattice which offers cavities for guest molecules. Hydrates were first identified and described by Davy and Faraday.[3]

[1] Salzmann, C.G. et al. (2009). *Phys. Rev. Lett.* **103**, 105701.

[2] The different phases of amorphous ice and the transformation between these phases is still under investigation, see e.g. Loerting, T. et al. (2001). *Phys. Chem. Chem. Phys.* **3**, 5355; Koza, M.M. et al. (2005). *Phys. Rev. Lett.* **94**, 125506; Loerting, T. et al. (2006). *Phys. Rev. Lett.* **96**, 025702.

[3] Davy, H. (1811). *Philos. Trans. R. Soc. London* **101**, 1; Faraday, M. (1823). *Philos. Trans. R. Soc. London* **113**, 160; Max, M. D., ed. (2000). *Natural Gas Hydrates in Oceanic and Permafrost Environments*. Kluwer Academic Publishers.

2.1.1 Structures

The first analysis of the hydrate structure was performed by von Stackelberg and co-workers in the late 1940s and 1950s using x-ray diffraction.[4] They were able to classify two different hydrate structures depending mainly on the type of the enclosed guest. Both structures are cubic with space group Pm3n (structure sI) and Fd3m (structure sII), respectively. The lattice constants depend only weakly on the guest molecule and were estimated to $a_{\mathrm{I}} \approx 12.0$ Å for sI and $a_{\mathrm{II}} \approx 17.3$ Å for sII. Ripmeester et al. were able to find a hexagonal hydrate structure (structure sH) which is only stable with two different guests.[5] This structure has the space group P6/mmm and lattice constants of $a_{\mathrm{H}} \approx 12$ Å and $c_{\mathrm{H}} \approx 10$ Å. Above these three common structures, more hydrate structures may be possible, at least from a theoretical point of view.[6] Recently a high pressure structure of xenon hydrate was found which was only known hypothetically before.[7]

In hexagonal ice, the water molecules align according the ice rules of Bernal-Fowler and Pauling.[8] Here, the tetrahedrally coordinated water molecules form hexagonal rings. In gas hydrates a similar water network is formed which offers – in contrast to ice – cavities where guest molecules are embedded. As the network is stabilized solely by these guest molecules, hydrates without guest do not exist.

The three common hydrate structures sI, sII and sH are formed of different cages. In all structures the pentagonal dodecahedron (5^{12}), containing twelve regular pentagonal faces, can be found. The cage is shown in Fig. 2.1a. As for all other cage types, water molecules are placed at the vertices. Thus, a nearly tetrahedrally coordinated water network with three angles of 108° and three of 110.9° and a first neighbor environment similar to cubic or hexagonal ice is achieved. The requirements for a three-dimensional lattice with only small distortions are satisfied by additional larger cavities beside the 5^{12} cavity. These are the $5^{12}6^2$ 14-hedron, consisting of twelve pentagonal and two hexagonal faces for structure sI, the $5^{12}6^4$ 16-hedron, consisting of twelve pentagonal and four hexagonal faces for structure sII, and both the $5^{12}6^8$ 20-hedron, consisting of twelve pentagonal and eight hexagonal faces and the strongly distorted $4^35^66^3$ 11-hedron, consisting of three rectangular, six pentagonal and three hexagonal faces for structure sH. All cavity types are presented in Fig. 2.1, properties of the hydrate structures are given in Tab. 2.1. The difference between sI and sII is achieved by linking

[4] von Stackelberg, M. (1949). *Naturwissenschaften* **36**, 327; von Stackelberg, M. and Müller, H.R. (1951*a*). *Naturwissenschaften* **38**, 456; von Stackelberg, M. and Müller, H.R. (1951*b*). *J. Chem. Phys.* **19**, 1319; von Stackelberg, M. and Jahns, W. (1954). *Z. Electrochemie* **58**, 162; von Stackelberg, M. and Müller, H.R. (1954). *Z. Electrochemie* **58**, 25.

[5] Ripmeester, J.A. et al. (1987). *Nature* **325**, 135.

[6] An overview of hypothetical hydrate structures which have not been found up to now is presented in Tribello, G. A. and Slater, B. (2009). *J. Chem. Phys.* **131**, 024703 and Jeffrey, G. A. (1984). *J. Inclusion Phenom.* **1**, 211 and references therein.

[7] Yang, L. et al. (2009). *Proc. Natl. Acad. Sci.* **106**, 6060.

[8] Bernal, J.D. and Fowler, R.H. (1933). *J. Chem. Phys.* **1**, 515; Pauling, L. (1935). *J. Am. Chem. Soc.* **57**, 2680.

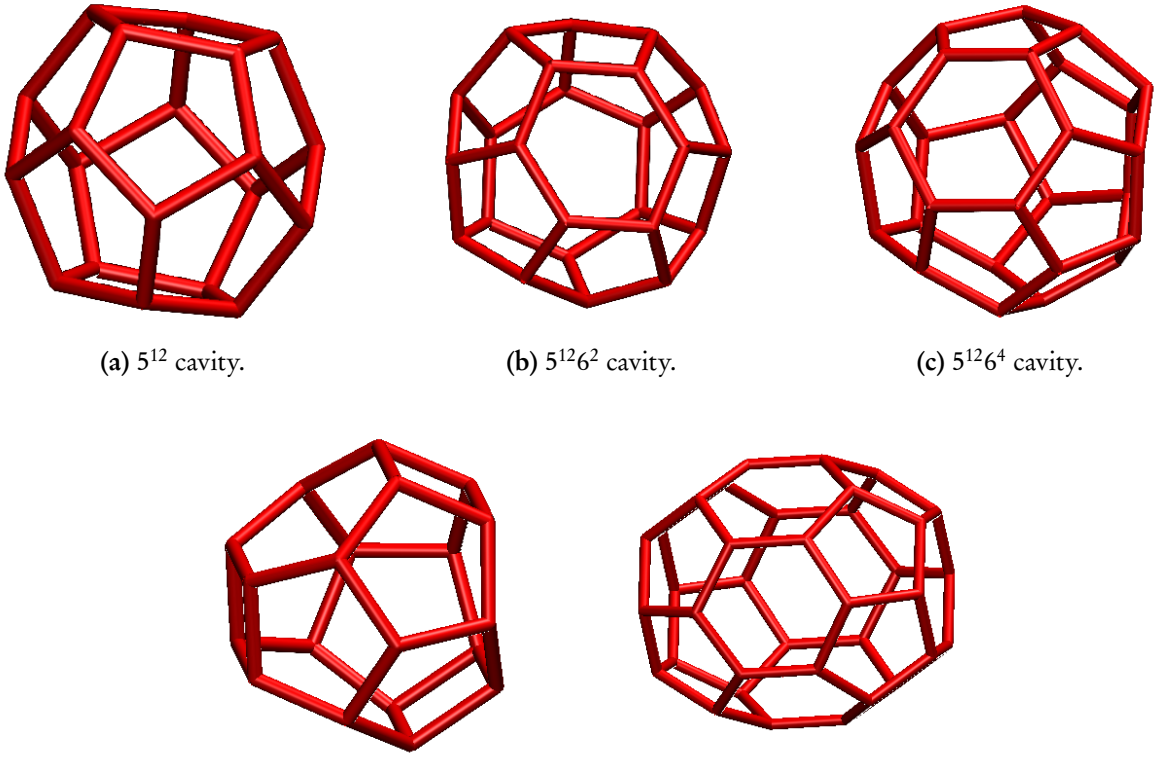

(a) 5^{12} cavity. (b) $5^{12}6^2$ cavity. (c) $5^{12}6^4$ cavity.

(d) $4^3 5^6 6^3$ cavity. (e) $5^{12}6^8$ cavity.

Figure 2.1: Cavity types which are found in sI, sII and sH hydrates.

the basic 5^{12} cavity in two different ways in order to achieve fourfold hydrogen bonds. Thus, structure sI results from vertex-linking of the 5^{12} cavities while structure sII shows face-sharing of the 5^{12} cavities in three dimensions.[9] The resulting spaces between the 5^{12} cavities are the larger cavities $5^{12}6^2$ and $5^{12}6^4$, respectively. In contrast, sH shows face-sharing in two dimensions. Snapshots of the hydrate structures together with the sites of the guest molecules are shown in Fig. 2.2.[10]

The cage occupancy of guest molecules depends strongly on the type of guest molecule and the pressure and temperature conditions. This non-stoichiometry is a characteristic feature of clathrate hydrates. CO_2 hydrate (structure sI), for instance, exhibits an occupancy of the large $5^{12}6^4$ cavities of approximately 95% – 100%, whereas only 40% – 70% of the small 5^{12} cavities are occupied by the guest molecules.[11] In contrast, in tetrahydrofuran (THF) hydrate (structure sII) any occupancy between 40% and 100% of the large cavities can be achieved by tuning the THF fraction in the water/THF mixture.[12] Here, the small cavities are not

[9] Sloan, E.D. and Koh, C.A. (2008). *Clathrate Hydrates of Natural Gases*. 3rd ed. CRC Press Inc.

[10] All snapshot structures in this thesis were created using the programme VMD available for free: *VMD Visual Molecular Dynamics*. URL: `http://www.ks.uiuc.edu/Research/vmd/`.

[11] Udachin, K.A. et al. (2001). *J. Phys. Chem. B* **105**, 4200; Klapproth, A. (2002). "Strukturuntersuchungen an Methan- und Kohlenstoffdioxid-Clathrat-Hydraten." Dissertation. Georg-August-Universität zu Göttingen.

[12] Ganji, H. et al. (2006). *J. Chem. Eng. Jpn.* **39**, 401.

Property	sI		sII		sH		
Lattice type	Primitive cubic		Face-centered cubic		Hexagonal		
Space group	Pm3n		Fd3m		P6/mmm		
Lattice parameters	$a = 12$ Å		$a = 17.3$ Å		$a = 12.2$ Å, $c = 10.1$ Å		
Cavity types	$5^{12}6^2$	5^{12}	$5^{12}6^4$	5^{12}	$5^{12}6^8$	4^35^6	5^{12}
Number per unit cell	6	2	8	16	1	2	3
Average cavity radius [Å]	4.33	3.95	4.73	3.91	5.71	4.06	3.91
Water molecules per unit cell	46		136		34		

Table 2.1: Selected properties of hydrates. Data taken from Koh, C. A. (2002). *Chem. Soc. Rev.* **31**, 157 and Sloan, E.D. and Koh, C.A. (2008). *Clathrate Hydrates of Natural Gases*. 3rd ed. CRC Press Inc.

occupied by THF molecules.

Due to the number of hexagonal faces, structure sH allows the trapping of the largest guest molecules, followed by structures sII and sI. However, not only the size ratio between guest and cage is crucial for the prediction of the formation of a certain hydrate structure. Here also the guest water interaction plays an important role. Hence, very small gas molecules like N_2 and O_2 form mainly sII hydrates. Such molecules are rather able to stabilize the small 5^{12} cage than the larger cages and form consequently structure sII because here the ratio between small and large cavities is significantly higher compared to sI.[13] Moreover, the large $5^{12}6^4$ cavity can be occupied by two molecules at high pressures. In contrast to the cubic structures, the formation of structure sH requires the presence of two different guest molecules, a large one stabilizing the large cage and a small one to stabilize the small and the medium cages.[14] An overview of hydrate forming guest molecules for sI and sII hydrates is presented in Tab. 2.2 together with the minimum pressure and maximum temperature value for a stable hydrate. In sH hydrates the small guest molecule, called help gas, occupies at least the small 5^{12} cavities, while one large molecule is occupying the large $5^{12}6^8$ cavity. As possible help gases, methane and xenon can be used.[15] Recently, hydrogen was also found to occupy the small cages and a rising number of possible structure sH hydrates containing hydrogen were identified.[16]

[13] Sloan, E.D. and Koh, C.A. (2008). *Clathrate Hydrates of Natural Gases*. 3rd ed. CRC Press Inc.
[14] Sloan, E.D. (2003). *Nature* **426**, 353.
[15] Ripmeester, J.A. and Ratcliffe, C.I. (1990). *J. Phys. Chem.* **94**, 8773.
[16] Duarte, A.R.C. et al. (2009). *J. Chem. Eng. Data* **54**, 1628.

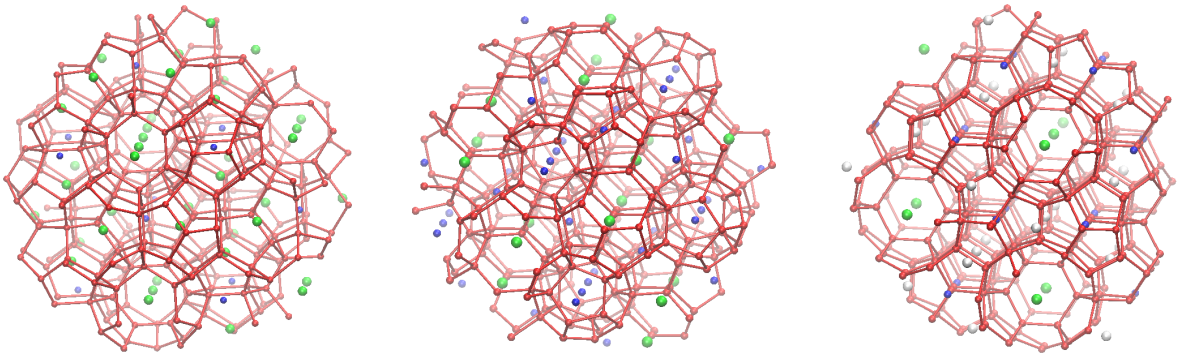

(a) Structure sI. **(b)** Structure sII. **(c)** Structure sH.

Figure 2.2: Snapshots of the three common gas hydrate structures. Sites of the water molecules are marked with red balls and are connected to emphasize the cage structure. Green balls: center of large cages; blue balls: center of small cages; white balls: center of medium cages (sH). Structures are built from coordinates given by Gutt, C. et al. (2000). *J. Chem. Phys.* **113**, 4713; Rawn, C. J. et al. (2003). *Can. J. Phys.* **81**, 431; Udachin, K. A. et al. (1997). *Supramol. Chem.* **8**, 173.

Hydrate structure	Guest	Pressure [bar]	Temperature [K]
sI	Xe	1.5	273.15
	CO_2	12.5	273.15
	CH_4	25.6	272.95
	C_2H_6	5.3	273.12
sII	Ar	88.2	272.35
	N_2	143.4	271.85
	O_2	110.6	272.15
	C_3H_8	1.76	273.15
	C_4H_8O (THF)	0.049	277.5
	H_2	2000	273.15

Table 2.2: Hydrate structure and stability of selected hydrate forming molecules. Data taken from Sloan, E.D. and Koh, C.A. (2008). *Clathrate Hydrates of Natural Gases*. 3rd ed. CRC Press Inc., Makino, T. et al. (2005). *J. Chem. Eng. Data* **50**, 2058, and Dyadin, Y. A. et al. (1999). *Mendeleev Commun.* **5**, 209.

2.1.2 Thermodynamical background

The stability region as a function of pressure, temperature and molar fraction for a certain system, such as hydrates, can be easily extracted from the corresponding phase diagram. Here, the degrees of freedom in such a system are described by Gibb's phase rule. A special feature of a mixture of water and hydrate formers is that they are in general not miscible in the liquid phase.[17] Thus, two liquid phases may coexist, whereas the hydrate serves as a mixed solid phase.

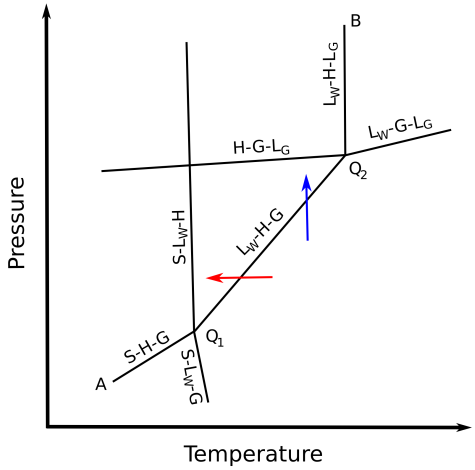

Figure 2.3: Schematic phase diagram of a water - hydrocarbon hydrate former mixture. The black lines are three-phase-equilibrium curves as indicated: S – ice, H – hydrate, G – gaseous guest, L_W – liquid water, L_G – liquid guest; the arrows demonstrate the hydrate formation processes studied in this thesis: red – THF hydrate formation by decreasing temperature, blue – CO_2 hydrate formation by increasing the pressure.

A schematic phase diagram of a mixture of water and a typical hydrocarbon hydrate former is shown in Fig. 2.3. The lines represent conditions where three phases are in equilibrium, e.g. between Q_1 and Q_2 these are liquid water, hydrate and gaseous guest. Above the line A-Q_1-Q_2-B the hydrate phase and either water or a guest phase are in equilibrium. At the quadruple point Q_1 ice, liquid water, gaseous guest, and hydrate are in equilibrium, while at Q_2 these are liquid water, hydrate, gaseous and liquid guest. For different materials, these points are found at very different conditions. For instance, CO_2-water has the quadruple point Q_2 at $T = 283$ K and $p = 43.5$ bar, for isobutane it is at $T = 275$ K and $p = 1.62$ bar. Methane-water and nitrogen-water mixtures do not have a second quadruple point Q_2, because the gases are supercritical in the corresponding temperature region.[18] The hydrate formation processes

[17] THF is an exception. However, this is valid for all hydrocarbons or CO_2 which are typical guest molecules. The following description is therefore focused on this case.

[18] More details concerning the phase diagram of hydrates can be found in Klapproth, A. (2002). "Strukturuntersuchungen an Methan- und Kohlenstoffdioxid-Clathrat-Hydraten." Dissertation. Georg-August-Universität zu Göttingen and for a large number of hydrate formers in Sloan, E.D. and Koh, C.A. (2008). *Clathrate Hydrates of Natural Gases*. 3rd ed. CRC Press Inc.

studied in this work were transitions induced by increasing the temperature at a constant pressure or by increasing the pressure at a constant temperature as marked in Fig. 2.3.[19]

2.1.3 Guest-host interaction

Up to now an empty water cage network has not been synthesized.[20] At least a certain amount of cages has to be occupied by the guest molecules to stabilize the cage network. This property is based on the hydrophobic effect. Especially for gas hydrate formation, a hydrophobic hydration caused by the interaction between water and dissolved gas molecules is interpreted as the starting point of gas hydrate nucleation.[21] In principle, higher pressures are needed for small molecules as N_2 or H_2 whereas large molecules stabilize the hydrate at significant lower pressure, e.g. tetrahydrofuran (C_4H_8O). However, this conclusion cannot be generalized. The small guest atom xenon, for instance, allows stable hydrates at a comparative low pressure of $p_{Xe} = 1.5$ bar at $T = 273.15$ K.

The guest-host interaction is also the main reason for the different properties of ice and hydrates. Although hydrate structures are similar to that of ice, both phases differ in many characteristics. Even the hydrates themselves show a different behavior depending on the enclosed guest molecules. While the strength of the hydrogen bonds is similar in both ice and hydrates,[22] the dynamics of water cage and guest molecules are coupled in hydrates.[23] These dynamic processes are frozen in at low temperatures, the hydrate lattice becomes rigid. The coupled dynamics result in slow diffusion times of water molecules which are approximately two orders of magnitude slower in hydrates compared to ice.[24] This is in general identified as the key property of clathrate hydrates in comparison to ice.

In contrast to the frozen dynamics at low temperatures, recent molecular dynamics (MD) simulations reported on a strong guest-host interaction between the polar guests THF and tert-butylmethylether and the water lattice at temperatures near the hydrate's dissociation temperature.[25] Here, the guest molecules form hydrogen bonds with the water molecules which may lead to a break-up of the cavities and thus to a decrease in the long-range order of the hydrate cage. A schematic drawing of a bond and a non-bond structure is presented in Fig. 2.4.[26] The cage deformation owing to the bond between a THF and a water molecule is

[19] However, in the case of THF the black line is the equilibrium line for the hydrate, liquid water and liquid THF.

[20] Recently different assumptions for producing empty cages have been published: Jacobson, L. C. et al. (2009). *J. Phys. Chem B* **113**, 10298.

[21] Bowron, D.T. et al. (1998). *Phys. Rev. Lett.* **81**, 4164.

[22] Bertie, J.A. and Jacobs, S.M. (1978). *J. Chem. Phys.* **69**, 4105.

[23] Tse, J.S. et al. (2001). *Europhys. Lett.* **54**, 354; Gutt, C. et al. (2002). *J. Chem. Phys.* **116**, 3795; Ripmeester, J.A. et al. (2004). *J. Phys. Chem. B* **108**, 929.

[24] Sloan, E.D. and Koh, C.A. (2008). *Clathrate Hydrates of Natural Gases*. 3rd ed. CRC Press Inc.

[25] Alavi, S. et al. (2009). *J. Chem. Phys.* **130**, 174501; Susilo, R. et al. (2009). *Chem. Phys. Chem.* **10**, 824.

[26] Structure files from Alavi, S. (2009–2010). *private communication*.

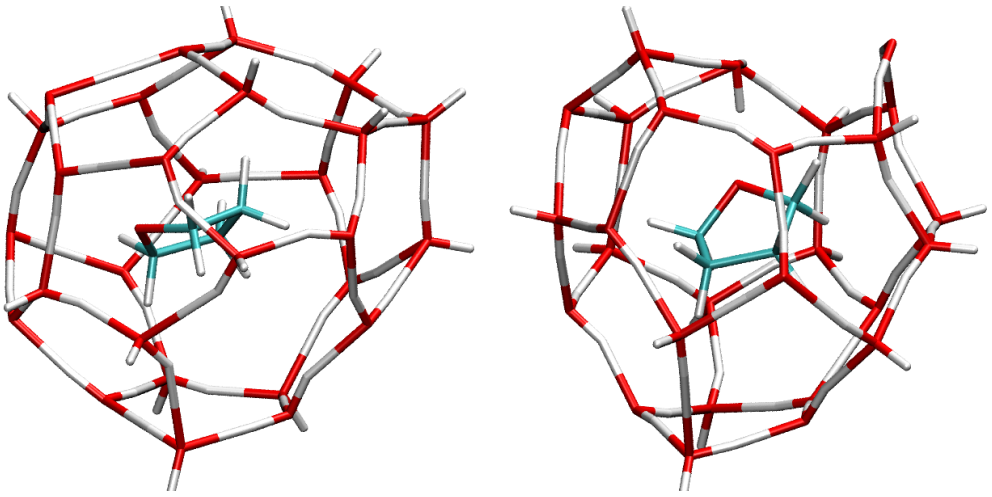

(a) Large cage without bond between THF and water.

(b) Large cage showing the formation of a bond between THF and water.

Figure 2.4: Comparison between bonded and non-bonded THF in a large sII cage.

clearly visible. As only the large cages were studied, influences from neighboring cages have not been analyzed. This bond formation is suppressed at lower temperatures. Nevertheless, such a break-up has not been studied in experiments so far.

2.1.4 Mechanical and thermal properties

In comparison to ice, hydrates exhibit different mechanical and thermal properties. It has been assumed for a long time that the mechanical strength of ice and hydrates is comparable. However, this comparability was later related to impurities of the analyzed samples. Using pure methane hydrate, the creep resistance of the hydrate was found to be approximately 20 times higher than in hexagonal ice.[27] This higher mechanical strength may be caused on the slow diffusion rate of water molecules in hydrates. Due to higher diffusion rates, ice usually deforms by propagating defects. In contrast, the bulk and shear modulus of ice and hydrates differ only slightly.[28]

Measurements of thermal properties demonstrated a large difference between ice and hydrates. The thermal conductivity in hydrates was found to be five times smaller than in ice and is thus similar to liquid water. Furthermore, the conductivity does not depend on the guest molecule or hydrate structure, all hydrates have a similar thermal conductivity.[29] As the conductivity of hydrates is proportional to temperature and does not depend on pres-

[27] Durham, W.B. et al. (2003). *Can. J. Phys.* **81**, 373.

[28] A lot of studies of the hydrate's elastic properties has been performed up to now. An overview is given in the book by Sloan and Koh (Sloan, E.D. and Koh, C.A. (2008). *Clathrate Hydrates of Natural Gases*. 3rd ed. CRC Press Inc.).

[29] See Waite, W.F. et al. (2005). *Proceedings of the Fifth International Conference on Gas Hydrates*, 1725 and references therein.

sure, a glass-like behavior which cannot be found in other crystalline materials is suggested. Recently, this behavior was explained on the basis of MD simulations by English and Tse.[30] They concluded that a potential empty hydrate cage and ice have a similar thermal conductivity, whereas in a hydrate with guests, due to collisions of the guest molecules with the water cages the heat-carrying lattice acoustic phonons are dephased and thus the thermal conductivity is decreased.[31] However, THF hydrate exhibits an anomaly at temperatures above approximately 265 K. Here, the conductivity rises sharply from 0.5 W/mK to 0.7 W/mK.[32] Similar results were found by Leaist and co-workers[33] in measurements of the heat capacity above $T = 260$ K. As other hydrates do not show such a behavior, it can be considered as a specific feature of THF hydrate, but a full understanding is still missing.

Hydrates and hexagonal ice differ also in their thermal expansion. Most surprisingly, the hydrates themselves differ between sI and sII structure. This is still an open question.[34] For instance, between 20 K and 273 K the volume of ethylen oxide hydrate (sI) is increased by 4.4%, the volume of THF hydrate (sII) increases by 3.4 %. These values are nearly the same for other guest molecules with the same hydrate structure. Hexagonal ice has a much lower thermal expansivity of approximately half of the hydrates. Once again this can be explained with the behavior of the guest molecules and the interaction between guest and water cage. Collisions of guest molecules and the water cage result in weakened water hydrogen bonds and an increased thermal expansivity of hydrates compared to ice.[35] The arrangement of the water molecules plays only a minor role.[36]

2.2 Applications

In this section a short overview on applications of clathrate hydrates is given. Most of them are proposed applications and thus are subject of current research.

Pipeline plugging

After the first identification of clathrate hydrates in the beginning of the 19th century, hydrates fell quickly into oblivion. They were only seen as a curiosity without practical value. When the gas industry began to build up gas and petroleum pipelines in the 1930s, wax-like

[30] English, N.J. and Tse, J.S. (2009). *Phys. Rev. Lett.* **103**, 015901.
[31] A glass-like thermal conductivity can also be found in other clathrates, see e.g. Nolas, G.S. et al. (1998). *Appl. Phys. Lett.* **73**, 178.
[32] Waite, W.F. et al. (2005). *Proceedings of the Fifth International Conference on Gas Hydrates*, 1725.
[33] Leaist, D.G. et al. (1982). *J. Phys. Chem.* **86**, 4175.
[34] Hester, K.C. et al. (2007). *J. Phys. Chem. B* **111**, 8830.
[35] Tse, J.S. (1987). *J. De Physique* **48**, 543.
[36] Tanaka, H. et al. (1997). *J. Phys. Chem. B* **101**, 6560.

(a) Gas hydrate from ocean floor. **(b)** Burning methane hydrate.

Figure 2.5: Hydrates from ocean floor as possible energy source.

incrustations were found inside the pipes which plugged them.[37] These materials were identified as clathrate hydrates constituted of a gas mixture of hydrocarbon gases.[38] Such hydrates are stable at significantly lower pressures compared to methane hydrate. A first step to prevent the formation of hydrates in pipelines was to use dried gases where the water amount was lowered. Furthermore, the pipeline system is often heated to keep the temperature above the hydrate formation temperature. Another possibility is the use of thermodynamic inhibitors like alcohol. These molecules build up hydrogen bonds with the remained water molecules. Thus, the water activity is decreased and the formation of hydrates is suppressed.[39] Alternatively, the use of so-called kinetic inhibitors is proposed to yield better results at lower costs.[40] For these inhibitors lower dosages are necessary compared to the thermodynamic inhibitors.

Energy source

Since the 1960s hydrates of natural gases were found in perma frost[41] and deep sea regions[42]. As most of these hydrates are pure methane hydrates, they act as potential natural reservoirs for energy recovery, see Fig. 2.5.[43] The stored gas amount in such hydrates is still under discussion. The most recent and accepted model by Klauda and Sandler yields an amount of

[37] Max, M. D., ed. (2000). *Natural Gas Hydrates in Oceanic and Permafrost Environments*. Kluwer Academic Publishers.
[38] Hammerschmidt, E.G. (1934). *Industrial and Engeneering Chemistry* **26**, 851.
[39] Koh, C. A. (2002). *Chem. Soc. Rev.* **31**, 157.
[40] The total cost for hydrate inhibition with thermodynamic inhibitors in pipelines was estimated to be more than 220 million US$ per year, see Sloan, E.D. (2003). *Nature* **426**, 353.
[41] Makogon, Y.F. (1965). *Gazov. Promst.* **5**, 14.
[42] Max, M. D., ed. (2000). *Natural Gas Hydrates in Oceanic and Permafrost Environments*. Kluwer Academic Publishers.
[43] Both photographs are taken from *Wikipedia*. URL: `http://en.wikipedia.org/`.

$120 \cdot 10^{15}$ m^3 which is huge compared to the assumed conventional stored methane amount in natural gas of $0.15 \cdot 10^{15}$ m^3.[44] However, it is not clear whether most of the hydrate occurs as pure blocks or in sediments. Due to the pressure and temperature conditions, hydrates can be found in perma frost regions in several 100 m depth, oceanic hydrates are mainly present at the edges of the tectonic plates.[45] A conventional mining is not possible because the hydrate may dissociate immediately after it has been removed from its deposit. Here a controlled, slow dissociation and subsequent pumping of methane or the replacing of methane with other gases may be more realistic.[46] This offers another application for gas hydrates: flue gas, especially carbon dioxide, sequestration at the ocean floor.

Flue gas recovery and CO_2 storage

Currently, safe possibilities for recovery and storage of climate gases, especially carbon dioxide, are intensively discussed. It has been demonstrated that THF hydrate is well suited to recover CO_2 from flue gases.[47] Furthermore, CO_2 sequestration[48] and here especially the storage of CO_2 in hydrates at the ocean floor is debated.[49] Liquid CO_2 is injected into the ocean, typically at a depth below 400 m, where the hydrate is formed immediately. Due to a larger density compared to the sea water, the hydrate will stay at the ocean floor. However, such hydrates may easily dissipate in the ocean and the gas will be released back to the atmosphere,[50] while the gas release is suppressed by hydrate storage in sediments.[51] An advancement of the pure carbon dioxide sequestration in hydrates is the replacement of methane by CO_2 in the already existing deep sea hydrates. Due to a lower free energy CO_2 replaces methane molecules in hydrates.[52] However, this process may take up to several 100 hours[53] and a at the end only a maximum of 65% of the methane can be replaced by CO_2. Better results are expected with hydrates in sediments and with the use of carbon dioxide/water emulsions instead of pure liquid CO_2.[54] Unfortunately, long-period effects of this storage to the oceanic environment are unknown.

[44] Klauda, J.B. and Sandler, S.I. (2005). *Energy Fuels* **19**, 459.
[45] Sloan, E.D. (2003). *Nature* **426**, 353.
[46] Schicks, J. (2008). *Chem. Unserer Zeit* **42**, 310; Boswell, R. (2009). *Science* **325**, 957.
[47] Kang, S. P. and Lee, H. (2000). *Environ. Sci. Technol.* **34**, 4397; Fan, S. et al. (2009). *Energy Fuels* **23**, 4202.
[48] See for an overview the special issue to carbon dioxide sequestration in Science: Smith, H.J. et al. (2009). *Science* **325**, 1641–1652.
[49] Brewer, P.G. et al. (1999). *Science* **284**, 943.
[50] Teng, H. et al. (1999). *Int. J. Energy Res.* **23**, 295; Schicks, J. (2008). *Chem. Unserer Zeit* **42**, 310.
[51] House, K.Z. et al. (2006). *PNAS* **103**, 12291.
[52] Dornan, P. et al. (2007). *J. Chem. Phys.* **127**, 124510.
[53] Lee, H. et al. (2003). *Angew. Chem. Int. Ed.* **42**, 5048; Yoon, J. et al. (2004). *J. Phys. Chem. A* **108**, 5057; Park, Y. et al. (2006). *PNAS* **103**, 12690.
[54] Zhou, X. et al. (2008). *Energy Fuels* **22**, 1759.

Hydrogen storage

A practical method for hydrogen storage, e.g. in hydrogen fuel cells, has to satisfy a certain number of requirements,[55] such as ambient or low pressure and temperature conditions. For this purpose, the storage of hydrogen in hydrates is a promising alternative which is currently under research.

Hydrogen hydrate has been synthesized for the first time by Dyadin et al.[56] Later, the detection of the characteristic double occupancy of the large cavities[57] offered the possibility of hydrogen storage in hydrates. The pure H_2 hydrate is not suitable for this issue, because a pressure of 2000 bar is necessary for a stable hydrate. However, a mixed THF-H_2 hydrate was found to have a minimum stability pressure of approximately 50 bar.[58] In contrast, more recent studies were not able to support the initially suggested storage capacities and reported smaller fractions of stored H_2.[59] However, owing to the lack of consistent results of the hydrate's storage capacity this topic is still highly debated. During the last years the storage of H_2 in structure sH hydrate has become object of research because the larger cavities and thus lower water fractions would allow higher guest concentrations.[60]

2.3 Hydrate formation

For a rising number of applications a detailed knowledge of the microscopic hydrate formation process is necessary. In general, the formation of hydrates can be subdivided in the initial nucleation on molecular lengths scales and the subsequent crystal growth process. This work is mainly focused on the nucleation in a liquid mixed phase of water and hydrate former.[61] Furthermore, hydrates can also form at ice-gas interfaces, but this process differs significantly from the formation from liquids[62] and is not part of this thesis.

A successful thermodynamical model describing the hydrate formation process has been published 50 years ago. An overview is presented in section 2.3.1. In order to describe the formation process on molecular length scales, several theoretical models have been published. These can be classified in cluster models predicting hydrate precursor clusters and stochastic

[55] Struzhkin, V.V. et al. (2007). *Chem. Rev.* **107**, 4133; van den Berg, A.W.C. and Areán, C.O. (2008). *Chem. Commun.* **13**, 668.
[56] Dyadin, Y. A. et al. (1999). *Mendeleev Commun.* **5**, 209.
[57] Mao, W. L. et al. (2002). *Science* **297**, 2247.
[58] Florusse, L.J. et al. (2004). *Science* **306**, 469.
[59] Hester, K.C. et al. (2006). *J. Phys. Chem.* **110**, 14024; Strobel, T.A. et al. (2006). *J. Phys. Chem. B* **110**, 17121; Ogata, K. et al. (2008). *Chem. Eng. Sci.* **63**, 5714; Mulder, F.M. et al. (2008). *Chem. Phys. Chem.* **9**, 1331; Sugahara, T. et al. (2009). *J. Am. Chem. Soc.* **131**, 14616.
[60] Duarte, A.R.C. et al. (2009). *J. Chem. Eng. Data* **54**, 1628; Schicks, J. (2008). *Chem. Unserer Zeit* **42**, 310; Strobel, T. A. et al. (2008). *J. Phys. Chem. B* **112**, 1885; Papadimitriou, N. I. et al. (2008). *Mendeleev Commun.* **112**, 14206.
[61] In the following, the phrases nucleation and formation are used equally.
[62] Staykova, D.K. et al. (2003). *J. Phys. Chem. B* **107**, 10299.

models without precursors. However, none of those has been verified experimentally so far. The most important models are presented in section 2.3.2, followed by an overview on previous studies of the hydrate formation including both computational and experimental work in section 2.3.3.

2.3.1 Thermodynamical model

Van der Waals and Platteeuw developed a model describing the hydrate formation process thermodynamically which is able to account for the the non-stoichiometry of hydrates.[63] The empty water cavities are interpreted as adsorption seats for guest molecules. Therefor, some assumptions were postulated:

- The cavities are spherical and can only hold one guest molecule.
- The enclosed molecules do not distort the water lattice and the interaction between the guest molecules is negligible.
- The assumptions of classical statistics are valid.

The distribution function of the guest molecules was calculated to[64]

$$\xi = \exp\left(-\frac{F_0}{k_\mathrm{B}T}\right)\sum_{N_{M_i}}\prod_i\left(\frac{N_i!}{(N_i-N_{M_i})!N_{M_i}!}\cdot(b_{M_i}\lambda_M)^{N_{M_i}}\right), \tag{2.1}$$

with F_0 the free energy of the guest; Boltzmann's constant k_B, temperature T; N_1, N_2 the number of corresponding cage types[65]; N_{M_1}, N_{M_2} the number of molecules in the corresponding cages; λ_M the activity; and b_{M_i} the distribution function of molecule M in cage i. The activity can be calculated via the chemical potential μ_M of guest molecule M yielding $\mu_M = k_\mathrm{B}T\ln(\lambda_M)$. The application of the binomial theorem and the calculation of the thermodynamical potential yields the occupancy θ_i of the cavities as function of the guest's partial pressure. It is similar to a Langmuir isotherm[66]

$$\theta_i = \frac{C_{M_i}p_M}{1+C_{M_i}p_M}, \tag{2.2}$$

[63] van der Waals, J.H. and Platteeuw, J.C. (1959). *Adv. Chem. Phys.* **2**, 1.

[64] Gutt, C. (2001). "Methan- und Xenonhydrat. Struktur und Dynamik." Dissertation. Christian-Albrechts-Universität zu Kiel.

[65] This means the large and small cages in sI and sII hydrate. The structure sH was not known when the model was developed.

[66] A more detailed summary is given in Klapproth, A. (2002). "Strukturuntersuchungen an Methan- und Kohlenstoffdioxid-Clathrat-Hydraten." Dissertation. Georg-August-Universität zu Göttingen and Gutt, C. (2001). "Methan- und Xenonhydrat. Struktur und Dynamik." Dissertation. Christian-Albrechts-Universität zu Kiel.

with C_{M_i} a Langmuir constant for molecule M in cavity i and the partial pressure p_M.

In order to gain information about the phase diagram and the stability of the hydrate, the chemical potential μ_H of the hydrate has to be known. It can be calculated yielding

$$\mu_H = \mu_0 + k_B T \sum_i \nu_i \ln(1 - \theta_i), \tag{2.3}$$

with μ_0 the chemical potential of the hypothetical empty lattice and ν_i the number of cages of type i relative to the number of water molecules in the unit cell. To form a hydrate from water or ice, μ_H has to be smaller than the corresponding potentials of water or ice. Thus, it is possible to calculate the minimum occupancy or pressure, which is necessary for a stable hydrate. Such hydrate phase diagrams (see section 2.1.2) can be modeled with high accuracy.

2.3.2 Hydrate formation on molecular length scales

In the literature, mainly three competing hydrate formation models are presented. These are the cluster nucleation theory[67], the local structuring hypothesis[68], and a surface driven model.[69] In the latter, an interface between water and hydrate former is necessary for formation of nucleation seeds. In general, the other two models also prefer the formation next to the interface, but with sufficient concentrations of the hydrate former also the formation in the bulk mixture becomes possible. A schematic comparison of the models is presented in Fig. 2.6. As the cluster nucleation theory and the surface driven model predict hydrate precursors, both models are subsummed in the figure and in the following referred to as cluster models.

Cluster models

The cluster nucleation theory was first proposed by Sloan.[70] It is based on the arrangement of water molecules around dissolved gas molecules. Such a structure consisting of guest and water molecules is called cluster. As pure water exists without clusters, such clusters form, e.g., owing to hydrophobic interactions.[71] At pressures and temperatures allowing the formation of hydrates, these clusters form immediately. Depending on the type of guest molecules and the corresponding hydrate structure, the clusters are composed of the guest molecule surrounded by 20 - 28 water molecules. By sharing faces the clusters agglomerate to larger units,

[67] Sloan, E.D. and Koh, C.A. (2008). *Clathrate Hydrates of Natural Gases*. 3rd ed. CRC Press Inc.
[68] Radhakrishnan, R. and Trout, B.L. (2002). *J. Chem. Phys.* **117**, 1786.
[69] Rodger, P.M. (1990). *J. Phys. Chem.* **94**, 6080; Kvamme, B. (2000). *Annals of the New York Academy of Science* **912**, 496.
[70] Sloan, E.D. and Fleyfel, F. (1991). *AIChE J.* **37**, 1281; Sloan, E.D. and Koh, C.A. (2008). *Clathrate Hydrates of Natural Gases*. 3rd ed. CRC Press Inc.
[71] Bowron, D.T. et al. (1998). *Phys. Rev. Lett.* **81**, 4164.

which can break up subsequently (see Fig. 2.6 b, c). After a critical cluster size is achieved, the macroscopic hydrate growth sets in. This model is very successful in explaining long induction times for hydrate formation, e.g., for propane hydrate. As a sII hydrate former, propane molecules have to be surrounded by 28 water molecules leading to significantly longer induction times compared to sI hydrate formers.

Similar to the cluster nucleation theory, the surface driven nucleation model also predicts the appearance of hydrate precursors. This model was first developed by Rodger and resulted from MD simulations of water-methane interfaces.[72] Within this model, gas molecules adsorb onto the water or ice surface. Subsequently, water molecules arrange around the adsorbed gas molecules and form partial cavities that are similar to the completed hydrate cages. A sufficient adsorption coverage will afterwards lead to a kinetically stabilized interface and the hydrate crystal growth sets in. An extension of this model was later presented by Kvamme et al.[73] Upon gas adsorption, liquid-like clusters containing water and gas molecules are formed supported by wave motion of the water surface. By agglomeration and growth of these clusters, the hydrate nucleation process sets in.

Recently, Guo et al. developed a cage adsorption hypothesis based on adsorption of methane molecules in partially and fully formed water cages as a result of MD simulations.[74] Owing to the proposed hydrate formation at the water-methane interface and similarities to the surface driven model, it can also be interpreted as an extension of the latter one. After dissolution of methane, cages form spontaneously and adsorb the methane molecules. These cages may act as precursors for the formation process. By absorbing more methane, the cages stabilize and a amorphous hydrate phase grows. After a certain size is achieved, the amorphous phase is transformed into a crystalline hydrate phase.

Stochastic models

Based on MD simulations of the water-liquid CO_2 interface, Radhakrishnan and Trout proposed the local structuring hypothesis for hydrate nucleation.[75] First they found that a hydrate formation via the cluster nucleation theory is highly unlikely because the energy barrier for cluster agglomeration is larger than for cluster disintegration. In contrast, they proposed a fully stochastic formation model. This model is schematically shown in Fig. 2.6 a-d-e. Thermal fluctuations cause guest molecules to be arranged in the liquid mixture with water at positions similar to their positions in the hydrate phase. The structure of the water molecules is also perturbed. If such locally ordered arrangements exceed the dimensions of a critical nucleus, hydrate nucleation sets in. As this process is fully stochastic, no hydrate precursor

[72] Rodger, P.M. (1990). *J. Phys. Chem.* **94**, 6080.
[73] Kvamme, B. (2000). *Annals of the New York Academy of Science* **912**, 496.
[74] Guo, G.-J. et al. (2009). *Phys. Chem. Chem. Phys.* **11**, 10427.
[75] Radhakrishnan, R. and Trout, B.L. (2002). *J. Chem. Phys.* **117**, 1786.

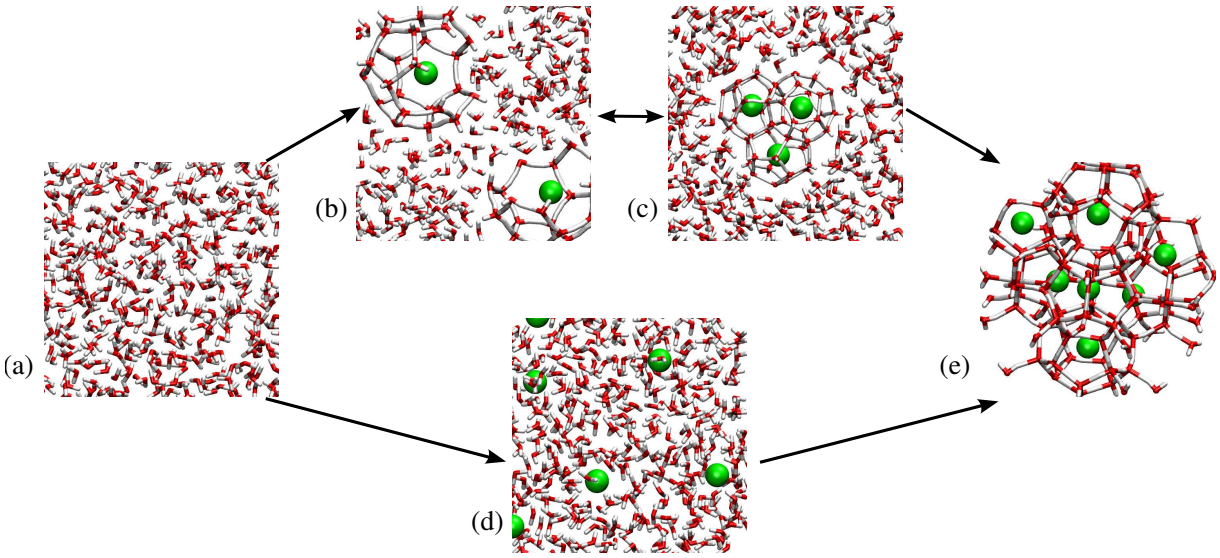

Figure 2.6: Hydrate formation models. (a) Initial condition: water without dissolved guest molecules. (b) Upon dissolution water clusters form around guest molecules. (c) Cluster agglomeration. (d) Stochastic arrangement of water and guests. (e) Hydrate growth. The path (a-b-c-e) demonstrates a formation with hydrate precursors, the path (a-d-e) a stochastic model without precursors.

clusters are formed in a supercooled mixture. Within this model, the size of the critical nucleus was estimated to $d_{\text{crit}} \lesssim 14.5$ Å, which is well below the value of $d_{\text{class}} \approx 32$ Å estimated with classical nucleation theory.[76]

2.3.3 Previous studies of hydrate formation

In order to favor one of these models, several MD simulations have been performed. By fixing CO_2 molecules at the positions they occupy in the hydrate, Hirai et al. found a special case of the local structuring hypothesis.[77] Here, the water molecules arrange similar to the study of Radhakrishnan and Trout. In studies of the methane-water interface Moon and co-workers found no evidence that the solvation shell around the dissolved methane molecules resembles a clathrate cage and may thus act together with the methane molecule as precursor.[78] Therefore, they also supported a local order model of nucleation like the local structuring hypothesis. Guo et al.[79] studied the methane-water interface and found compatible structures to the clusters predicted by Rodger.[80] However, they concluded that the formation and agglomeration of these clusters is very unlikely and hence a stochastic model seems to be more adequate. Above these, other studies also favored the local structuring hypothesis, e.g. due

[76] Larson, M.A. and Garside, J. (1986). *Chem. Eng. Sci.* **41**, 1285.
[77] Hirai, S. et al. (1997). *Energy Convers. Manage.* **38**, S301.
[78] Moon, C. et al. (2003). *J. Am. Chem. Soc.* **125**, 4706.
[79] Guo, G.-J. et al. (2007). *J. Phys. Chem. C* **111**, 2595.
[80] Rodger, P.M. (1990). *J. Phys. Chem.* **94**, 6080.

to the need of a certain order of water and guest similar to the local structuring hypothesis[81] or the demonstration that the full formation of a naturally formed dodecahedral water cluster, which may act as hydrate precursor, is very unlikely.[82] A recent MD simulation study on microsecond time scales of methane hydrate formation revealed a spontaneous hydrate nucleation.[83] In particular, the positions of the guest molecules affect this process and the formation of the small 5^{12} cavity is favored. Due to the larger ratio of these cavities in sII hydrate, motifs of this structure are present in the early stage of methane hydrate together with unusual $5^{12}6^3$ cavities.[84] However, cluster fragments which may act as precursors, were not identified in this study.

In contrast to these studies, Zhang and co-workers were able to identify cage fragments which seemed to be hydrate structure sI cavities.[85] In their study they focused on the formation behavior with additives and hence they did not analyze the pure formation process more explicitly. Moreover, in an earlier study of Guo et al. the lifetimes found for empty water cages and cages filled by methane molecules were in good agreement as predicted by the cluster nucleation theory.[86]

Beyond these computational studies a lot of experimental work has been performed to examine the formation of hydrates. However, most of the studies focused on the growth process because the often used scattering methods or calorimetric measurements are sensitive to the formation of crystallites, but cannot be used to study changes in the local structure of the water-guest mixture on a molecular level which is the aim of this thesis. Takeya et al. reported a formation on a macroscopic level at a liquid-liquid interface where the initial nucleation starts at the water surface.[87] According to this study, needle-like hydrate clusters grow towards the water bulk. The hydrate formation from water and gaseous CO_2 was reported by Morgan and co-workers who observed the growing hydrate crystals optically and by means of calorimetric methods.[88] Here, gaseous CO_2 was bubbled through the water bulk for several minutes to induce the hydrate formation. A different approach has been followed by Ohmura et al.[89] In order to observe methane hydrate formation the authors used water spraying and, by optical observation, found a hydrate formation that starts at the water surface. As stated before, neither hydrate precursor formation nor the initial nucleation can be observed with these methods. Koh and co-workers showed time-resolved macroscopic hydrate formation in

[81] Hawtin, R.W. et al. (2008). *Phys. Chem. Chem. Phys.* **10**, 4853.
[82] Guo, G.-J. et al. (2008). *J. Chem. Phys.* **128**, 194504.
[83] Walsh, M.R. et al. (2009). *Science* **326**, 1095.
[84] Vatamanu, J. and Kusalik, P.G. (2006). *J. Am. Chem. Soc.* **128**, 15588.
[85] Zhang, J. et al. (2008). *J. Phys. Chem. B* **112**, 10608.
[86] Guo, G.-J. et al. (2004). *J. Chem. Phys.* **124**, 1542.
[87] Takeya, S. et al. (2000). *J. Phys. Chem. B* **104**, 4164.
[88] Morgan, J.J. et al. (1999). *Environ. Sci. Technol.* **33**, 1448.
[89] Ohmura, R. et al. (2002). *Energy Fuels* **16**, 1141.

the stirred water-CO_2 bulk mixture by means of X-ray diffraction.[90] The authors were not able to favor one hydrate formation model as they were performing measurements in a disturbed system, where seeds for macroscopic hydrate formation are offered. However, they proposed a dynamic intermediate phase during the hydrate formation and growth process. By neutron diffraction measurements on methane hydrate formation and dissociation, Thompson et al. were able to identify how small hydrate clusters influence the surrounding water molecules.[91] Studies of the hydration shell by neutron diffraction[92] and nuclear magnetic resonance (NMR) experiments[93] were able to identify a loosely organized water network around dissolved molecules which seem to differ from expected hydrate precursors. However, these findings were also not suited to favor a formation model.

[90] Koh, C.A. et al. (1996). *J. Phys. Chem.* **100**, 6412.
[91] Thompson, H. et al. (2006). *J. Chem. Phys.* **124**, 164508.
[92] Koh, C.A. et al. (2000). *J. Chem. Phys.* **113**, 6390.
[93] Gao, S. et al. (2005). *Ind. Eng. Chem. Res.* **44**, 7373.

3 Carbon dioxide hydrate formation at interfaces

Beside methane and hydrogen, carbon dioxide (CO_2, see Fig. 3.1) is the most important guest molecule in studies on gas hydrates. Therefore, it was chosen in this thesis to study the hydrate formation process at the water-CO_2 interface. In contrast to methane or hydrogen, it is possible to investigate both liquid-liquid and liquid-gas interfaces, because CO_2 is not in the supercritical phase at experimental formation conditions. Hence, both x-ray reflectivity measurements at the liquid-gas and x-ray diffraction measurements at the liquid-liquid interface were performed in order to study the formation of hydrate precursors and the growth of small hydrate crystallites.

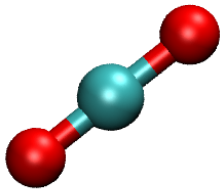

Figure 3.1: Carbon dioxide molecule. Red balls are the oxygen atoms, the turquoise ball the carbon atom. The molecular diameter is approximately $d_{CO2} = 5.12$ Å matching thus perfectly in the cavities of a structure sI hydrate.

First, the theoretical background of x-ray reflectivity is given in this chapter.[1] Subsequently, properties of liquid-gas interfaces are discussed, in particular the adsorption of gas molecules and the surface roughness due to capillary wave motion. Then the experimental set-ups and procedures are presented, followed by the data analysis and discussion.

3.1 X-ray reflectivity at surfaces and interfaces

X-ray reflectivity (XRR) is a well established technique to study properties of a sample's surface with atomic resolution. It is sensitive to molecular thin layers and allows to determine

[1] As x-ray diffraction is part of many textbooks (e.g. Als-Nielsen, J. and McMorrow, D. (2001). *Elements of Modern X-ray Physics*. John Wiley & Sons, Ltd), an overview on this technique is not given here.

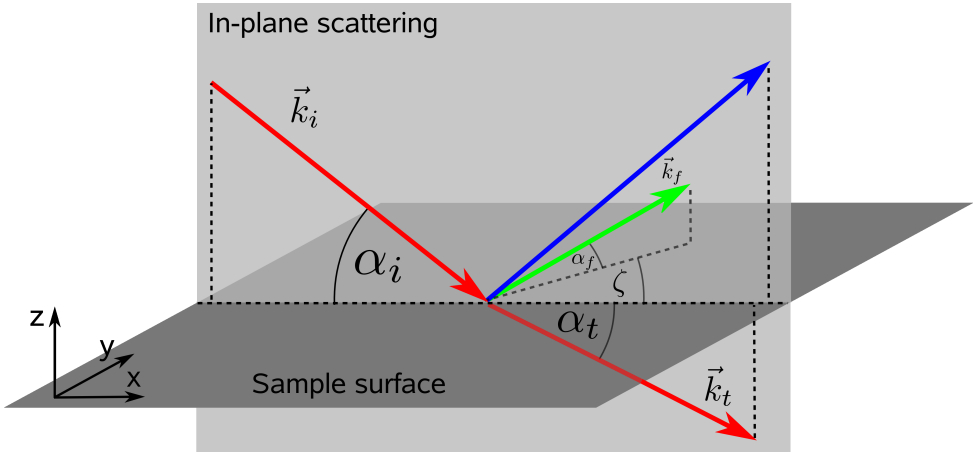

Figure 3.2: Scattering geometry of surface x-ray scattering experiments. For x-ray reflectivity only the specular scattered intensity is detected: $\alpha_i = \alpha_r, \zeta = 0°$. The blue line represents the case of reflectivity measurements.

the sample's surface roughness. The basic theory of x-ray reflectivity is discussed in the following paragraphs. After the scattering geometry has been defined, the scattering from a smooth surface is discussed in the terms of optics. Afterwards, a mathematical description in the framework of the first-order Born approximation is presented.

3.1.1 Scattering geometry

The schematic scattering geometry for x-ray scattering experiments on surfaces is shown in Fig. 3.2. The incident x-ray beam, described by a plane wave with wave vector $\vec{k}_i$, hits the sample at the angle α_i. It is scattered at the angle α_f between sample surface and beam, and the angle ζ between the plane of incidence defined by the incident beam and the surface normal, with wave vector $\vec{k}_f$. Part of the beam is transmitted into the sample at the refractive angle α_t. In the case of $\zeta = 0°$, the geometry is called *in-plane*. X-ray reflectivity measurements are a special case of in-plane scattering with $\alpha_i = \alpha_f$. Therefore, it is also called *specular scattering*, any change of the requirements $\alpha_f = \alpha_i$ and $\zeta = 0°$ probe *diffuse scattering*.[2]

For a mathematical description of the scattering process, the x-ray beams are identified by electromagnetic waves with wave vectors $\vec{k}_i, \vec{k}_t, \vec{k}_f$ as indicated in Fig. 3.2. The scattered radiation is usually analyzed as a function of the wave vector transfer $\vec{q} = \vec{k}_f - \vec{k}_i$. The wave vector transfer can be calculated using Fig. 3.2:

[2]It is important to note, that diffuse scattering also occurs in the case of specular scattering, but cannot be separated from the measured intensity. For the practical procedure to correct such contributions, see section 3.4.

$$\vec{q} = \begin{pmatrix} q_x \\ q_y \\ q_z \end{pmatrix} = |\vec{k}_i| \begin{pmatrix} \cos(\alpha_f)\cos(\theta) - \cos(\alpha_i) \\ \cos(\alpha_f)\sin(\theta) \\ \sin(\alpha_i) + \sin(\alpha_f) \end{pmatrix}, \tag{3.1}$$

with $|\vec{k}_i| = \frac{2\pi}{\lambda}$ and the wavelength λ. In the case of XRR ($\alpha_f = \alpha_i, \zeta = 0$), Eq. 3.1 simplifies to:

$$\vec{q}_{\mathrm{XRR}} = \begin{pmatrix} 0 \\ 0 \\ q_z \end{pmatrix} = \frac{4\pi}{\lambda} \begin{pmatrix} 0 \\ 0 \\ \sin(\alpha_i) \end{pmatrix}. \tag{3.2}$$

Thus, in XRR experiments only wave vector transfers perpendicular to the sample surface are accessible yielding information about the lateral averaged vertical density profile. In order to gain lateral information on the sample surface, e.g. two-dimensional molecular ordering, it is necessary to achieve $q_x \neq 0$ or $q_y \neq 0$. This is usually done by choosing $\zeta \neq 0°$ or, in particular for small q_x, $\zeta = 0°, \alpha_i \neq \alpha_f$. The resulting scattering method is called *grazing incidence diffraction* (GID). However, as this is not part of this work, the next paragraphs are focused only on XRR measurements.

3.1.2 Smooth surfaces

In reflectivity experiments, the sample is characterized by its index of refraction n. For an arrangement of N atoms per unit cell that are approximated as harmonic oscillators with resonance frequencies ω_j, it is expressed as[3]

$$n^2(\vec{r}) = 1 + N\frac{e^2}{\epsilon_0 m_e}\sum_{j=1}^{N}\frac{f_j}{\omega_j^2 - \omega^2 - 2i\omega\eta_j}, \tag{3.3}$$

where e is the electron charge, m_e the electron mass, ω the frequency of the incoming beam, and η_j are damping factors. The oscillator strengths f_j are in general complex numbers:

$$f_j = f_j^0 + f_j'(\omega) + i f_j''(\omega). \tag{3.4}$$

[3] Tolan, M. (1999). *X-ray Scattering from Soft Matter Thin Films*. Springer.

Here, $f_j'(\omega)$ and $f_j''(\omega)$ take into account dispersion and absorption corrections. For x-rays, $\omega > \omega_j$ becomes valid and Eq. 3.3 can be simplified to[4]

$$n = 1 - \delta + i\beta, \tag{3.5}$$

with the dispersion $\delta = \frac{\lambda^2}{2\pi} r_e \rho$, where r_e denotes the classical electron radius and ρ the electron density, and the absorption $\beta = \frac{\lambda}{4\pi}\mu$, where μ denotes the linear absorption coefficient. Depending on the wavelength of the incident radiation and the sample density, δ is usually on the order of $10^{-7} - 10^{-5}$, whereas β is typically $1-3$ orders of magnitude smaller.

The condition of continuous electromagnetic waves at smooth surfaces leads to the Fresnel formulas for the reflectivity coefficient r and transmission coefficient t, respectively:

$$r = \frac{k_{i,z} - k_{t,z}}{k_{i,z} + k_{t,z}}, \qquad t = \frac{2k_{i,z}}{k_{i,z} + k_{t,z}}, \tag{3.6}$$

where z denotes the z-coordinate of the corresponding wave vector. Owing to the small deviation from 1 of the index of refraction, the beam polarization can be neglected. Using Snell's law

$$\cos(\alpha_i) = n\cos(\alpha_t) \tag{3.7}$$

and a Taylor expansion for α_t yielding $\alpha_t = \sqrt{\alpha_i^2 - 2\delta}$ with neglected absorption, α_t becomes zero for $\alpha_i^2 = 2\delta =: \alpha_c^2$. For $\alpha_i < \alpha_c$ the transmission angle α_t is a complex number. The angle α_c defines the critical angle for external total reflection. Above this angle, the penetration depth increases exponentially. The reflected intensity, also called Fresnel reflectivity, $R = |r|^2 =: R_F$ equals 1 for $\alpha_i \leq \alpha_c$, whereas for $\alpha_i > \alpha_c$ it decreases rapidly. The Fresnel reflectivity R_F and the transmission function $T = |t|^2$ are shown in Fig. 3.3. The maximum of T at $\alpha_i/\alpha_c = 1$ is originated from constructive interference of reflected and transmitted waves.[5] For larger incident angles, T reaches unity. However, only R is analyzed in the reflectivity measurements in this thesis, the next paragraph focuses on the influence of surface roughness and thin layers only on the reflectivity curve.

3.1.3 First-order Born approximation

In principle, in terms of optics the description of XRR is quite simple and has a great practical value, e.g. for data analysis using the Parratt algorithm.[6] A sufficient mathematical approach is formulated with the kinematical or first-order Born approximation. Within this approach,

[4] Als-Nielsen, J. and McMorrow, D. (2001). *Elements of Modern X-ray Physics*. John Wiley & Sons, Ltd; Tolan, M. (1999). *X-ray Scattering from Soft Matter Thin Films*. Springer.
[5] Tolan, M. (1999). *X-ray Scattering from Soft Matter Thin Films*. Springer.
[6] A detailed description is given in the appendix A and Parratt, L.G. (1954). *Phys. Rev.* **95**, 359.

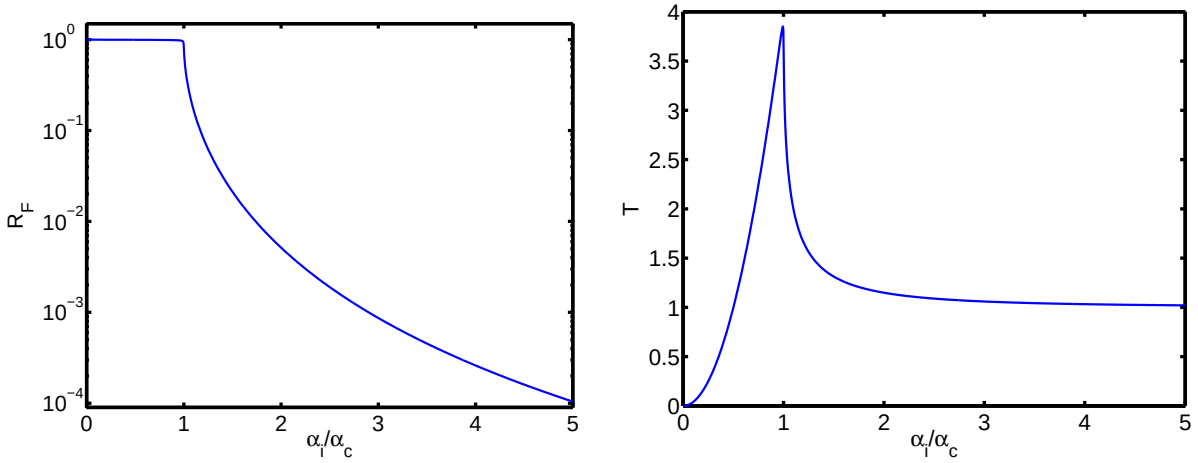

(a) Fresnel reflectivity $R_F = |r|^2$. **(b)** Fresnel transmission $T = |t|^2$.

Figure 3.3: Reflected intensity and transmission for smooth surfaces as function of the normalized incident angle α_i/α_c.

only single scattering events are taken into account. It holds for incident angles α_i larger than approximately the triple critical angle.[7] Then, the scattering amplitude is proportional to the Fourier transform of the electron density $\rho(\vec{r})$ and is calculated to[8]

$$A(\vec{q}) = -r_e \int_V \rho(\vec{r}) e^{i\vec{q}\cdot\vec{r}} \mathrm{d}^3 r. \tag{3.8}$$

For liquid surfaces, certain simplifications can be considered:

- The electron density is constant above and below the surface.
- The incident wave is damped exponentially with increasing penetration depth.
- Surface fluctuations only consist of vertical particle motions described by a height-height correlation function $C_{zz}(\vec{r})$. With this function, a RMS (Root Mean Square) surface roughness σ can be calculated.

These simplifications are valid for XRR, but cannot be used for diffuse scattering at large wave vector transfers.[9] Eq. 3.8 can be transferred to a surface integral, yielding

$$A(\vec{q}) = \frac{i r_e \Delta\rho}{q_z} \int_S e^{i\vec{q}\cdot\vec{r}} \mathrm{d}^2 r, \tag{3.9}$$

where S is the illuminated surface area and $\Delta\rho$ the electron density difference between the two media forming the interface. The differential scattering cross section $\frac{\mathrm{d}\sigma}{\mathrm{d}\Omega}$ is defined as

[7] Tolan, M. (1999). *X-ray Scattering from Soft Matter Thin Films*. Springer.
[8] Als-Nielsen, J. and McMorrow, D. (2001). *Elements of Modern X-ray Physics*. John Wiley & Sons, Ltd.
[9] Paulus, M. et al. (2008*a*). *Phys. Rev. B* **78**, 235419.

the absolute square of the scattering amplitude A. It describes the intensity per solid angle $\mathrm{d}\Omega$ and serves as the experimental measure in scattering experiments. Using a height-height correlation function $C_{zz}(\vec{r})$ for the mathematical description of the surfaces, one obtains[10]

$$\frac{\mathrm{d}\sigma}{\mathrm{d}\Omega} = \left(\frac{r_e \Delta\rho}{q_z}\right)^2 \frac{S_0}{\sin(\alpha_i)} e^{-q_z^2\sigma^2} \int e^{q_z^2 C_{zz}(\vec{r})} e^{-i(q_x x + q_y y)} \mathrm{d}x\mathrm{d}y, \tag{3.10}$$

where $\frac{S_0}{\sin(\alpha_i)}$ denotes the illuminated surface area which decreases with increasing incident angle α_i. With the condition $C(\vec{r}) \to 0$ for $x, y \to \infty$, Eq. 3.10 can be separated into two summands, the first describing the specular, the second the diffuse scattering:

$$\begin{aligned}
\frac{\mathrm{d}\sigma}{\mathrm{d}\Omega} &= \left(\frac{\mathrm{d}\sigma}{\mathrm{d}\Omega}\right)_{\text{spec}} + \left(\frac{\mathrm{d}\sigma}{\mathrm{d}\Omega}\right)_{\text{diff}} \\
&= \left(\frac{2\pi r_e \Delta\rho}{q_z}\right)^2 \frac{S_0}{\sin(\alpha_i)} e^{-q_z^2\sigma^2} \delta(q_x)\delta(q_y) \\
&+ \left(\frac{r_e \Delta\rho}{q_z}\right)^2 \frac{S_0}{\sin(\alpha_i)} e^{-q_z^2\sigma^2} \int \left(e^{q_z^2 C_{zz}(x,y)} - 1\right) e^{-i(q_x x + q_y y)} \mathrm{d}x\mathrm{d}y.
\end{aligned} \tag{3.11}$$

The δ-functions guarantee the conditions for specular scattering ($\alpha_i = \alpha_f$, $\zeta = 0°$). Following Eq. 3.11, in XRR experiments also a certain amount of diffusely scattered radiation is measured which has to be corrected for. The correction procedure chosen in this work is presented in the experimental section. With the definition $\left(\frac{\mathrm{d}\sigma}{\mathrm{d}\Omega}\right)_{\text{Fres}} = \left(\frac{2\pi r_e \Delta\rho}{q_z}\right)^2 \frac{S_0}{\sin(\alpha_i)}$ one obtains finally for the reflectivity

$$\left(\frac{\mathrm{d}\sigma}{\mathrm{d}\Omega}\right)_{\text{spec}} = \left(\frac{\mathrm{d}\sigma}{\mathrm{d}\Omega}\right)_{\text{Fres}} e^{-q_z^2\sigma^2}, \tag{3.12}$$

see Fig. 3.4a. It can be shown that $\left(\frac{\mathrm{d}\sigma}{\mathrm{d}\Omega}\right)_{\text{Fres}}$ corresponds to the expression for the Fresnel reflectivity describing the reflectivity of a smooth surface for $\alpha_i \gg \alpha_c$.[11] By calculating the solid angle $\mathrm{d}\Omega$, the intensity for the reflectivity from a smooth surface normalized by the incident intensity can be determined:

$$I_{\mathrm{F}}(q_z) = \frac{(4\pi r_e \Delta\rho)^2}{q_z^4}. \tag{3.13}$$

[10] Sinha, S.K. et al. (1988). *Phys. Rev. B* **38**, 2297.

[11] Sinha, S.K. et al. (1988). *Phys. Rev. B* **38**, 2297; Als-Nielsen, J. and McMorrow, D. (2001). *Elements of Modern X-ray Physics*. John Wiley & Sons, Ltd.

The exponential in Eq. 3.12 describes the influence of the surface roughness σ. Obviously, the roughness damps the reflected intensity in comparison with the Fresnel reflectivity, see Fig. 3.4a. Furthermore, due to the divergence for $q_z \to 0$, Eq. 3.13 cannot hold for small q_z as mentioned above. To avoid these shortcomings of the kinematical approximation, I_F from Eq. 3.13 is usually replaced by the Fresnel reflectivity $R_F = |r|^2$ from Eq. 3.6, yielding

$$R(q_z) = R_F e^{-q_z^2 \sigma^2} \tag{3.14}$$

for the reflectivity of a rough surface. In this derivation it was assumed that the interface has an error-function shape.[12] By allowing arbitrary shape functions, the following expression is obtained:[13]

$$R(q_z) = R_F(q_z) \cdot \left| \frac{1}{\rho_\infty} \int \frac{\mathrm{d}\rho(z)}{\mathrm{d}z} e^{i q_z z} \mathrm{d}z \right|^2, \tag{3.15}$$

where ρ_∞ denotes the averaged electron density of the sample. Especially for liquid surfaces with a surface roughness due to capillary wave motion one obtains[14]

$$R(q_z) = R_F e^{-\sigma^2 q_z^2} \frac{1}{\sqrt{\pi}} \Gamma((1 - q_z^2 k_B T/(2\pi\gamma))/2, 2\pi^2 (q_z \Delta\alpha/2)^2/q_{uc}^2), \tag{3.16}$$

where $\Gamma(x, y)$ is the incomplete Gammafunction, γ the surface tension, and q_{uc} a cut-off wave vector. More details of capillary wave theory are given in section 3.2.2.

This mathematical description of a single surface can be expanded to layer systems. Assuming an electron density profile of the sample, which can be described by a sum of two Heaviside functions whose transition is modeled by a certain interfacial roughness, one obtains for the specular part of the differential cross section[15]

$$\left(\frac{\mathrm{d}\sigma}{\mathrm{d}\Omega}\right)_{\text{spec}} = \frac{1}{q_z^2} \left(\Delta\rho_1^2 e^{-q_z^2 \sigma_1^2} + \Delta\rho_2^2 e^{-q_z^2 \sigma_2^2} + 2\Delta\rho_1 \Delta\rho_2 \cos(q_z l) e^{-\frac{q_z^2}{2}(\sigma_1^2 + \sigma_2^2)} \right). \tag{3.17}$$

Therein, $\Delta\rho_{1/2}$ denote the electron density differences at the substrate-layer and layer-vacuum interfaces, $\sigma_{1/2}$ the roughnesses of the substrate and layer, respectively, and l the layer thickness. In Fig. 3.4b the cross section is plotted for two different layer thicknesses. The existence of a layer becomes visible in the oscillations, called Kiessig-fringes.[16] They allow to estimate

[12] Sinha, S.K. et al. (1988). *Phys. Rev. B* **38**, 2297; Tolan, M. (1999). *X-ray Scattering from Soft Matter Thin Films*. Springer; Ghaderi, T. (2006). "X-ray Intensity Correlation Spectroscopy from Fluid Surfaces." PhD thesis. Universität Dortmund.

[13] Tolan, M. (1999). *X-ray Scattering from Soft Matter Thin Films*. Springer.

[14] Ghaderi, T. (2006). "X-ray Intensity Correlation Spectroscopy from Fluid Surfaces." PhD thesis. Universität Dortmund.

[15] Paulus, M. (2006). "Röntgenstreuung an Flüssigkeits-Gas Grenzflächen." PhD thesis. Universität Dortmund.

[16] Kiessig, H. (1931). *Ann. Phys.* **402**, 769.

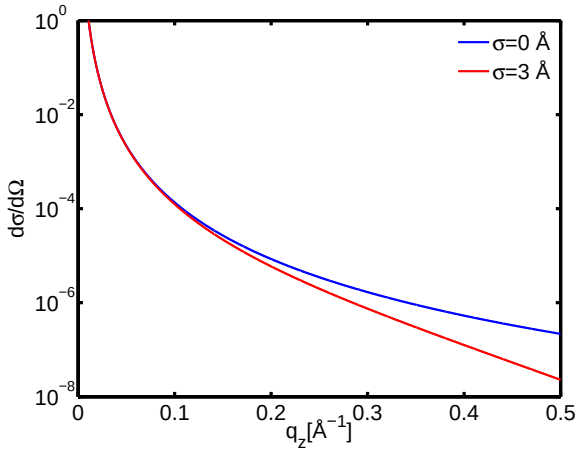

(a) Influence of surface roughness on Eq. 3.12.

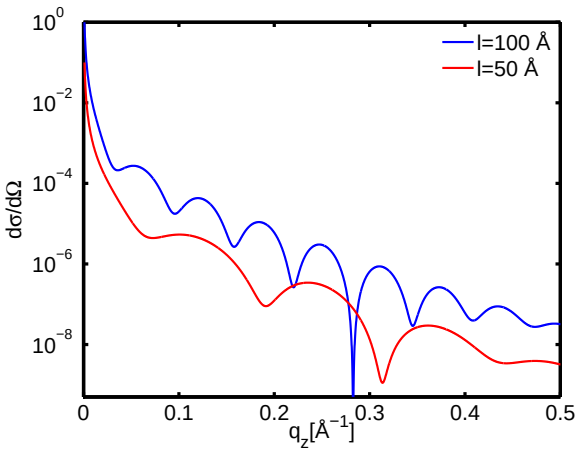

(b) Influence of layer thickness. Curves are shifted for clarity.

Figure 3.4: Sensitivity of XRR cross sections to surface roughness and layer thickness. A comparison with Fig. 3.3 demonstrates the shortcomings of the kinematical approximation for small q_z. The substrate is assumed to have an electron density similar to water and a roughness of $\sigma_1 = 3$ Å, the layer's density is lowered to 75% of the water density and the roughness was set to $\sigma_2 = 6$ Å.

the layer thickness via $l = 2\pi/\Delta q_z$, with the difference of two subsequent minima of the oscillations Δq_z. Again, for small q_z, calculations from the kinematical approximation show differences from an XRR experiment. Especially the region of total reflection cannot be modeled accurately. Here, better results can be achieved by replacing q_z with $\tilde{q}_z = 2k \sin(\sqrt{\alpha_i^2 + \alpha_c^2})$.[17] Thus, XRR measurements give access to roughnesses, layer thicknesses and density differences. However, high intensities are necessary to access a large q_z-range because of the relation $R \propto q_z^{-4}$ (Eq. 3.13). This condition is achieved for 3rd generation synchrotron radiation sources where the experiments in this thesis were performed. An overview on the analysis of XRR experiments is presented in the appendix section A.

3.2 Liquid-gas interfaces

Interfaces between liquids and gases are very common in nature. Thus, they are in the focus of research for several decades. Especially x-ray reflectivity measurements are able to analyze the two main processes at such interfaces: the adsorption of gas molecules on a liquid surface and the surface roughening due to capillary waves. Both are discussed in this section. A hydrate or hydrate precursor formation at the water-CO_2 interface will be found in deviations from adsorption and capillary wave theory of experimental data obtained from XRR measurement.

[17] Tolan, M. (1999). *X-ray Scattering from Soft Matter Thin Films*. Springer.

3.2.1 Adsorption

At interfaces between liquids or solids and gases the adsorption of gas molecules on the surface may occur.[18] The adsorbed molecules form a liquid-like layer. Depending on the interfacial tension between substrate and adsorbate, different types of adsorption exist.[19] These are a complete wetting, where the adsorbed molecules form a complete layer, and a partial adsorption where islands are formed on the surface. By changing the temperature or the composition of the substrate, a transition between these two types may occur.[20] In this section, only the complete wetting is discussed because the measured values for the interfacial tension of water and liquid CO_2 suggests a complete adsorption for this system.[21]

The adsorption of gas molecules on surfaces is originated in van der Waals forces between substrate surface and the gas phase. These forces are caused by fluctuations of dipoles. Here, the type of dipoles, e.g. permanent or secondary, is not crucial. The main property of this interaction is the r^{-6} proportionality for the attractive interaction. To model repulsion for short distances, a term proportional to $-r^{-12}$ can be utilized. Altogether, the Lennard-Jones potential U_{LJ} is used to describe the van der Waals interaction mathematically:[22]

$$U_{\mathrm{LJ}}(r) = -4\epsilon_{\mathrm{LJ}}\left[\left(\frac{\sigma_{\mathrm{LJ}}}{r}\right)^6 - \left(\frac{\sigma_{\mathrm{LJ}}}{r}\right)^{12}\right], \tag{3.18}$$

where $\epsilon_{\mathrm{LJ}}, \sigma_{\mathrm{LJ}}$ are substance-specific parameters which describe the magnitude and the range of the interaction. An overview of Lennard-Jones constants for different substances is given by Yaws.[23] The constraints for stable films for a system consisting of a liquid substrate, a gas phase, and a liquid adsorbed layer are minima of the free energy F. Such minima mark stable thermodynamical states. For the given system, the free energy per area can be written as[24]

$$F = \gamma_{\mathrm{S}} + \gamma_{\mathrm{L}} - \frac{A_{\mathrm{eff}}}{12\pi l^2} + l k_{\mathrm{B}} T \Delta\rho_p \ln\left(\frac{p}{p_0}\right), \tag{3.19}$$

where $\gamma_{\mathrm{S/L}}$ denote the surface tension of the substrate and the adsorbed layer, respectively, l the layer thickness, k_{B} Boltzmann's constant, $\Delta\rho_p$ the particle density difference between substrate and layer, p the gas pressure, and p_0 the condensation pressure of the gas at the

[18] See, e.g. Paulus, M. et al. (2005). *Phys. Rev. E* **72**, 061601 and Shokuie, K. et al. (2007). *Thin Solid Films* **515**, 5660.

[19] This is depicted by Young's equation, see Israelachvili, J. (2000). *Intermolecular & Surface Forces*. Academic Press Inc.

[20] Bertrand, E. et al. (2000). *Phys. Rev. Lett.* **85**, 1282; Bonn, D. and Ross, D. (2001). *Rep. Prog. Phys.* **64**, 1085.

[21] Uchida, T. et al. (2000). "Laboratory studies on the formation and dissociation processes of CO_2-hydrate crystals - measurements of interfacial tension between CO_2 and water." *Proceedings of the International Symposium on Deep Sea Sequestration of CO_2*, 1–4–1.

[22] Ibach, H. and Lüth, H. (2002). *Festkörperphysik*. Springer.

[23] Yaws, C.L. (1987). *The Properties of gases and liquids*. McGraw-Hill.

[24] Paulus, M. et al. (2005). *Phys. Rev. E* **72**, 061601.

temperature T. The magnitude of the interaction is given by the so-called Hamaker constant A_{eff}. It can be calculated in the framework of the Lifshitz theory from the indices of refraction and the permittivity for visible light of the involved phases. By neglecting retardation effects one yields[25]

$$A_{\text{eff}} \approx \frac{3}{4} k_{\text{B}} T \left(\frac{\epsilon_{\text{S}} - \epsilon_{\text{L}}}{\epsilon_{\text{S}} + \epsilon_{\text{L}}}\right)\left(\frac{\epsilon_{\text{G}} - \epsilon_{\text{L}}}{\epsilon_{\text{G}} + \epsilon_{\text{L}}}\right) + \frac{3}{8\sqrt{2}} h\nu_e \frac{(n_{\text{S}}^2 - n_{\text{L}}^2)(n_{\text{G}}^2 - n_{\text{L}}^2)}{\sqrt{n_{\text{S}}^2 + n_{\text{L}}^2}\sqrt{n_{\text{G}}^2 + n_{\text{L}}^2}(\sqrt{n_{\text{S}}^2 + n_{\text{L}}^2} + \sqrt{n_{\text{G}}^2 + n_{\text{L}}^2})}. \tag{3.20}$$

Here, the indices S, L, G denote the substrate, layer, and gas phase, respectively, $\nu_e \approx 3 \cdot 10^{15}$ Hz is an averaged absorption frequency. It has to be noted that Eq. 3.20 gives only an estimation for A_{eff}. Experimentally obtained values differ from calculated values, in general a good agreement is achieved when experimental and theoretical values are in the same order of magnitude.[26] Minima of F with respect to the layer thickness l can be calculated by differentiation of Eq. 3.19, yielding

$$l_m = \left(\frac{A_{\text{eff}}}{6\pi\Delta\rho_p k_{\text{B}} T \ln(p/p_0)}\right)^{1/3}. \tag{3.21}$$

These minima of F as a function of pressure p are called adsorption isotherm, which is in this case related to a Frenkel-Halsey-Hill isotherm.[27] Obviously, the layer thickness l_m diverges for $p \to p_0$, which corresponds to macroscopic condensation. Furthermore, A_{eff} has to be negative, a positive Hamaker constant would lead to a partial adsorption or the absence of any adsorption.[28]

The dynamics of the substrate surface and the adsorbed layer were neglected in the derivation of Eq. 3.21. Fluctuations at both surfaces also affect the properties, e.g. the thickness, of an adsorbed layer. Especially the roughness of thin films was found to be strongly dependent on the layer thickness. These effects are discussed in the following section.

3.2.2 Capillary waves

Liquid surfaces are characterized by a surface roughness on the order of several Ångströms.[29] This roughness is caused by capillary waves[30] and can be determined by x-ray reflectivity

[25] Israelachvili, J. (2000). *Intermolecular & Surface Forces*. Academic Press Inc.

[26] For an overview of different sample systems see Lietz, D. (2007). "Hochenergiereflektometrie an Festkörper-Gas und Festkörper-Flüssigkeits-Grenzflächen." Diploma thesis. Universität Dortmund.

[27] Frenkel, J. (1946). *Kinetic Theory of Liquids*. Oxford University Press; Halsey, G.D. (1948). *J. Chem. Phys.* **16**, 931; Hill, T.L. (1949). *J. Chem. Phys.* **17**, 590.

[28] Bonn, D. and Ross, D. (2001). *Rep. Prog. Phys.* **64**, 1085.

[29] Braslau, A. et al. (1985). *Phys. Rev. Lett.* **54**, 114.

[30] Buff, F.P. et al. (1965). *Phys. Rev. Lett.* **15**, 621.

measurements. These capillary waves are originated by thermal fluctuations. Their amplitude is defined by the surface tension γ and temperature T. The starting point for calculation of the capillary wave roughness is the energy per area ΔU, which is necessary to bend the liquid surface. ΔU consists of a term that describes the energy which is needed to work against the surface tension and another term describing the force needed to lift the surface against gravitation, yielding[31]

$$\Delta U = \frac{\gamma}{2}\int |\nabla h(\vec{r}_{||})|^2 \mathrm{d}^2 r_{||} + \frac{\rho_m g}{2}\int h^2(\vec{r}_{||})\mathrm{d}^2 r_{||}, \tag{3.22}$$

where $h(\vec{r}_{||})$ is the vertical displacement at position $\vec{r}_{||}$ in the liquid's surface plane, ρ_m the mass density, and g the gravitational acceleration. By replacing $h(\vec{r}_{||})$ with its Fourier transform $\tilde{h}(\vec{q}_{||})$ and application of the equipartition theorem, the result

$$\langle \tilde{h}(\vec{q}_{||})\tilde{h}(-\vec{q}_{||})\rangle = \frac{k_\mathrm{B}T}{4\pi^2\gamma}\frac{1}{q_{||}^2 + q_\mathrm{grav}^2} \tag{3.23}$$

is obtained for the averaged displacement.[32] Here, $\vec{q}_{||} = (q_x, q_y)$ and $q_\mathrm{grav} = \sqrt{\rho_m g/\gamma}$ denotes a cut-off wave vector. Below q_grav gravitational waves are dominant compared to capillary waves. Integration of Eq. 3.23 finally yields the capillary wave roughness σ of a free surface:

$$\sigma^2 = \int_{q_\mathrm{grav}}^{q_\mathrm{uc}} \langle \tilde{h}(\vec{q}_{||})\tilde{h}(-\vec{q}_{||})\rangle \mathrm{d}^2 q_{||} = \frac{k_\mathrm{B}T}{2\pi\gamma}\ln\left(\frac{q_\mathrm{uc}}{q_\mathrm{grav}}\right). \tag{3.24}$$

The upper wave vector cut-off q_uc is usually defined via the diameter d_m of the molecules forming the liquid, yielding $q_\mathrm{uc} \approx 2\pi/d_m$. Furthermore, in x-ray reflectivity experiments the experimental resolution has to be taken into account. Thus, the gravitational cut-off q_grav has to be replaced by a larger resolution cut-off q_lc. In the case of synchrotron radiation, this can be calculated via the opening angle of the detector $\Delta\alpha_f$ yielding $q_\mathrm{lc} \approx \frac{1}{2} q_z \Delta\alpha_f$.[33]

To calculate roughnesses of arbitrary surfaces, an adequate mathematical description has to be found. Here, a statistical approach using height-height correlation functions is very successful.[34] The correlation function is defined as

$$C_{zz}(\vec{R}_{||}) = \frac{1}{A}\int_A h(\vec{r}_{||})h(\vec{r}_{||} + \vec{R}_{||})\mathrm{d}^2 r_{||} =: \langle h(\vec{r}_{||})h(\vec{r}_{||} + \vec{R}_{||})\rangle_{\vec{r}_{||}}, \tag{3.25}$$

[31] Braslau, A. et al. (1988). *Phys. Rev. A* **38**, 2457; Tolan, M. (1999). *X-ray Scattering from Soft Matter Thin Films*. Springer.
[32] Braslau, A. et al. (1988). *Phys. Rev. A* **38**, 2457.
[33] Braslau, A. et al. (1985). *Phys. Rev. Lett.* **54**, 114; Braslau, A. et al. (1988). *Phys. Rev. A* **38**, 2457; Tolan, M. (1999). *X-ray Scattering from Soft Matter Thin Films*. Springer.
[34] Doerr, A.K. et al. (1999). *Phys. Rev. Lett.* **83**, 3470.

with a vector $\vec{R}_{||}$ lying in the surface plane. The surface roughness is determined by

$$\sigma^2 = C_{zz}(0) = \langle h^2(\vec{r}_{||})\rangle_{\vec{r}_{||}}. \tag{3.26}$$

Using the Fourier transform $\tilde{C}_{zz}(\vec{q}_{||})$ of $C_{zz}(\vec{R}_{||})$ and the Wiener-Khinchin theorem[35] the roughness can be calculated from Eq. 3.23:

$$\sigma^2 = \int_{q_{lc}}^{q_{uc}} \tilde{C}_{zz}(\vec{q}_{||})\mathrm{d}^2 q_{||} = \int_{q_{lc}}^{q_{uc}} \langle \tilde{h}(\vec{q}_{||})\tilde{h}(-\vec{q}_{||})\rangle \mathrm{d}^2 q_{||}. \tag{3.27}$$

The cut-offs define the experimentally obtainable finite q region. Moreover, the roughnesses of thin liquid, e.g. adsorbed, films can be calculated. In several experiments it was found that the roughness of an adsorbed layer is a function of the layer's thickness.[36] This is originated in a stronger interaction between substrate and layer, which results in decreased wave amplitudes at small thicknesses.[37] The interaction of the two interfaces is described by the system's free energy F. In order to handle F mathematically, it is expressed by a Taylor expansion around the minimum l_m. Usually, an expansion to second order is sufficient for layer thicknesses down to several 10 Å.[38] In the framework of this *harmonic approximation*, the expression

$$\sigma^2_{2,\mathrm{harm}} = \frac{k_B T}{4\pi\gamma_L}\left(\frac{\gamma_S}{\gamma_S+\gamma_L}\ln\left(\frac{q_{uc}^2(\varkappa+q_{lc}^2)}{q_{lc}^2(\varkappa+q_{uc}^2)}\right)+\ln\left(\frac{\varkappa+q_{uc}^2}{\varkappa+q_{lc}^2}\right)\right) \tag{3.28}$$

is obtained for the layer roughness,[39] with $\varkappa = \frac{B(\gamma_S+\gamma_L)}{\gamma_S\gamma_L}$ and $B = \left.\frac{\partial^2 F}{\partial l^2}\right|_{l_m}$. A similar expression is found for the substrate's roughness, but it has been shown that this roughness is not strongly affected by the properties of the layer for $\gamma_S \gg \gamma_L$ and can be assumed to be constant.[40] However, for layer thicknesses $l_m \leq 60$ Å Eq. 3.28 yields in general layer roughnesses which exceed experimentally obtained values by a few Ångströms. Therefore, an anharmonic expansion to

[35] Tolan, M. (1999). *X-ray Scattering from Soft Matter Thin Films*. Springer.
[36] See e.g. Heilmann, R.K. et al. (2001). *Phys. Rev. E* **63**, 205405; Shokuie, K. et al. (2007). *Thin Solid Films* **515**, 5660; Tolan, M. (1999). *X-ray Scattering from Soft Matter Thin Films*. Springer and references therein.
[37] Doerr, A.K. et al. (1999). *Phys. Rev. Lett.* **83**, 3470.
[38] Li, M. et al. (2001). *Phys. Rev. Lett.* **86**, 5934.
[39] Paulus, M. et al. (2005). *Phys. Rev. E* **72**, 061601.
[40] Paulus, M. (2006). "Röntgenstreuung an Flüssigkeits-Gas Grenzflächen." PhD thesis. Universität Dortmund.

fourth order provides better results. In this framework, the layer roughness is calculated to[41]

$$\sigma^2_{2,\mathrm{anharm}} = \frac{k_\mathrm{B}T}{4\pi a}\ln\left(\frac{\varkappa/2+q^2_\mathrm{uc}}{\varkappa/2}\right)\left(1-D\frac{k_\mathrm{B}T}{8\pi}\left(\frac{1}{aB}-\frac{1}{aB+q^2_\mathrm{uc}}\right)\right) + \frac{1}{2\pi}\int_{q_\mathrm{lc}}^{q_\mathrm{uc}}\frac{\beta^2}{\beta^2+q^2l_m^4}\frac{k_\mathrm{B}T}{\gamma_\mathrm{S}q^2}\mathrm{d}^3q, \tag{3.29}$$

with $D = \left(\frac{\partial^4 G}{\partial l^4}\right)_{l_m}$, $a = \frac{\gamma_\mathrm{S}\gamma_\mathrm{L}}{2\gamma_\mathrm{S}+2\gamma_\mathrm{L}}$ and $\beta^2 = \frac{A_\mathrm{eff}}{2\pi\gamma_\mathrm{L}}$. Furthermore, the layer thickness is slightly increased within the anharmonic approximation compared to Eq. 3.21:

$$l_\mathrm{anharm} = l_m + 2\frac{\sigma_{2,\mathrm{harm}}}{l_m}, \tag{3.30}$$

with the roughness $\sigma_{2,\mathrm{harm}}$ from the harmonic approximation in Eq. 3.28.

3.3 Experimental details

In the framework of this thesis, x-ray reflectivity and x-ray diffraction measurements on CO_2 hydrate formation at liquid-gas and liquid-liquid water-CO_2 interfaces were performed. The stability pressure of CO_2 hydrate is $p = 12.5$ bar at $T \approx 273$ K, see Tab. 2.2. Therefore, reflectivity measurements of the liquid-gas interface were performed up to the CO_2 condensation pressure of $p_0 \approx 35$ bar at $T = 273.3$ K, while x-ray diffraction spectra at the liquid-liquid interface were measured at $p \approx 36$ bar and $T = 273.3$ K. Such high gas pressures demand the design of accurate sample environments. Conventional sample cells cannot be used due to a plenty of unusual constraints, e.g., high gas pressures and temperature stability. These special cells require particular beamlines with high energy x-rays. In this chapter, the sample cells are presented together with the experimental set-ups of the beamlines where the experiments were carried out, and experimental details.

3.3.1 X-ray reflectivity measurements at the water - gaseous CO_2 interface

In order to satisfy the requirements of x-ray reflectivity experiments at high gas pressures, a special high pressure sample cell is necessary to study the water - CO_2 interface at hydrate formation conditions. Due to the robust design of such cells, high energy x-rays are inevitable for the measurements. In this section, both the sample cells and the experimental set-up are presented.

[41] Li, M. and Schlossman, M.L. (2002). *Phys. Rev. E* **65**, 061608; Paulus, M. et al. (2005). *Phys. Rev. E* **72**, 061601.

Sample cell

The high pressure reflectivity experiments require the use of a stainless steel sample cell with solid aluminum windows (instead of conventional transparent foils like Polyimid). Moreover, a flat water surface is needed. Due to the surface tension of water, a meniscus is formed which results in a bent surface. Therefore, the cell was designed with a diameter large enough to neglect the meniscus. To satisfy these requests, a cylindrical cell with an inner diameter of 124 mm and a wall thickness of 20 mm was used in this work, see Fig. 3.5.[42]

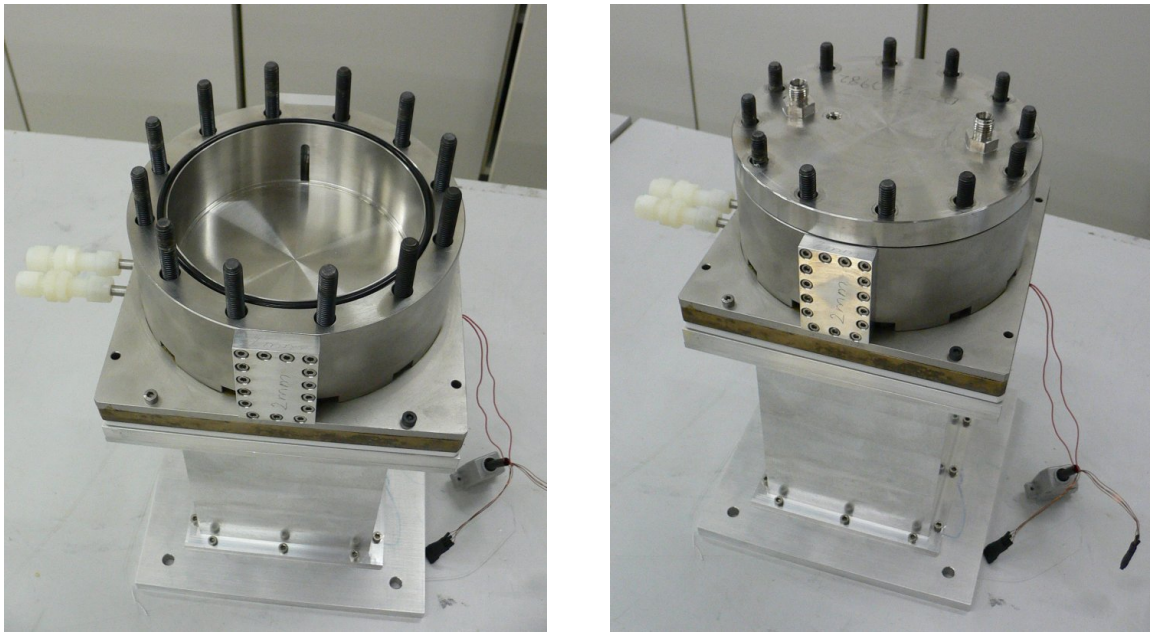

Figure 3.5: Photographs of the high pressure reflectivity cell. Left: Opened cell. Right: Closed cell.

The cell has an inner volume of approximately 500 ml. In order to achieve a sufficient water meniscus, a 1 mm high edge is milled out the cell wall. A 17 mm thick cap is fixed by twelve M8 bolts that are placed equidistantly in the wall. At two opposing positions, cutouts are milled with a height of 28.5 mm and width of 5 mm. Here, the aluminum windows with a thickness of 2 mm are fixed with 15 M3 bolts from the outside. The cap and the two windows are sealed with Viton O-rings. Three holes for gas in- and outlet and for two Pt100 temperature sensors are drilled through the cap. The cell is cooled by a brass board placed under the cell. This board is flushed by a cooling liquid, e.g., isopropanol or ethanol. For a good temperature stability, a heating foil is placed into a copper board under the cell. The temperature sensors and the heating foil are connected to a Lakeshore controller. A temperature stability of $\Delta T = 0.02$ K during the measurements is achieved. The stability of this sample cell was

[42] Details of the cell are given in Lietz, D. (2007). "Hochenergiereflektometrie an Festkörper-Gas und Festkörper-Flüssigkeits-Grenzflächen." Diploma thesis. Universität Dortmund; Paulus, M. et al. (2008*b*). *J. Synch. Rad.* 15, 600.

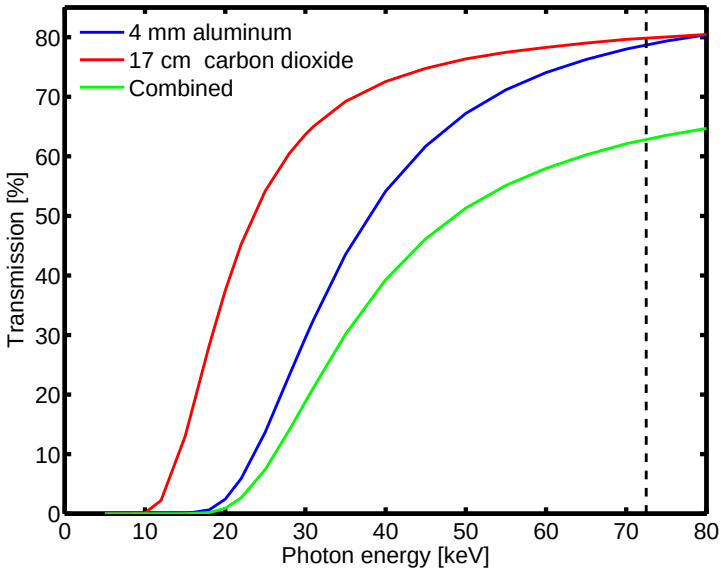

Figure 3.6: X-ray transmission as function of x-ray energy of the aluminum windows, the CO_2 atmosphere at $p = 30$ bar, and the combination of both. The energy at ID15A of $E = 72.5$ keV is marked as dashed black line.

tested for pressures up to 120 bar allowing working pressures up to 40 bar. To prevent pressures above 40 bar, a security valve is mounted at the gas outlet and opens when the pressure inside the cell exceeds 40 bar.

The need for high energy x-rays for reflectivity experiments at CO_2 pressures up to 35 bar is demonstrated in Fig. 3.6.[43] Here, the absorption of x-rays by the aluminum windows and the gas atmosphere at $p = 30$ bar, assuming a beam path through the gas volume of 17 cm, is shown as function of x-ray energy. The transmission of the gas atmosphere increases at lower pressures. It is clearly visible that at x-ray energies of $E = 8$ - 12 keV the transmission is nearly zero. At the energy of $E = 72.5$ keV the x-ray transmission is approximately 60 %. Thus, this experiment has to be performed at such high x-ray energies.

Reflectivity setup at ID15A of ESRF

The x-ray reflectivity experiment was performed using the high energy micro-diffraction (HEMD) setup at beamline ID15A of ESRF at an incident energy of $E = 72.5$ keV.[44] The source of the x-ray beam is a seven pole asymmetric wiggler with a critical energy of $E_c = 44.1$ keV. X-ray energies below 40 keV are absorbed by a water-cooled Al absorber placed in the white beam. The white beam is monochromatized by a pair of asymmetrically cut and bent Si crystals in a fixed exit Laue geometry.[45] In such a way, an energy resolution of $\Delta E \approx 2 \cdot 10^{-3}$ at

[43] The transmission curves were calculated using *NIST XCOM*. URL: `http://physics.nist.gov/PhysRefData/Xcom/html/xcom1.html`.
[44] *Beamline ID15*. URL: `http://www.esrf.eu/UsersAndScience/Experiments/StructMaterials/ID15`.
[45] Suortti, P. and Schulze, C. (1995). *J. Synch. Rad.* **2**, 6.

incident energies around 70 keV is achieved.[46] The monochromatic beam is focused by compound refractive lenses (CRL) to a spot size of 8×16 μm^2 (v×h), yielding a primary intensity of approximately $2 \cdot 10^{10}$ photons per second in the focused beam. A triangular plexiglas plate acting as absorber can be moved into the beam to reduce the count rate of the detector. The incident energy is monitored by a Si PIN diode. In order to allow reflectivity measurements at liquid surfaces and interfaces, the x-ray beam can be tilted by a pair of triangular Si crystals up to incident angles of approximately $\alpha_i = 2°$.[47] This angle corresponds to a maximum obtainable wave vector transfer of $q_z = 2.5$ Å^{-1} at $E = 72.5$ keV. In contrast to other reflectivity setups for liquid surfaces, the sample position has not to be changed for different incident angles. Thereby, disturbances of the sample originated by moving the sample or by vibrations of the diffractometer motors can be prevented. These disturbances would, e.g., lead to higher roughnesses of liquid surfaces. A photograph and a schematic drawing of the HEMD set-up for liquid surfaces at ID15A is presented in Fig. 3.7 together with a high pressure sample cell, similar to the one used in this work.

Experimental procedure

All measurements were performed at $T = 273.3$ K in order to avoid the formation of ice. The vertical gap of the detector slit was set to 1 mm, guaranteeing a reasonable signal-to-noise ratio by sufficient count rates. The water used in the experiment was filtered by a Millipore apparatus, CO_2 purchased by Air Liquide had a purity of 99.998%. After filling the sample cell with water resulting in a well defined meniscus, the cell was flushed with CO_2 for several minutes to achieve a pure CO_2 atmosphere inside the sample cell. Then a gas pressure of $p = 1$ bar was adjusted and the reflectivity was measured. Following the reflectivity measurement, the detector was moved horizontally by 0.1° to an out-of-plane position in order to measure the diffusely scattered intensity which is necessary for an accurate background subtraction. Afterwards, the gas pressure was raised. This procedure was repeated for several pressures up to the condensation pressure of $p_0 = 34.99$ bar. At high pressures above 33 bar, multiple measurements were performed to detect changes at the water/CO_2 interface. Altogether, a pressure above 33 bar was set for approximately 8 hours. During the whole measurements the sample was not stirred or disturbed to prevent hydrate nucleation seeds.

3.3.2 X-ray diffraction at liquid - liquid interfaces

As x-ray diffraction measurements at the liquid water - liquid CO_2 interface had to be performed beyond the condensation pressure of CO_2, again special sample cells and high energy

[46] Reichert, H. et al. (2003). *Physica B* **336**, 46.
[47] Details of this so called *liquid monochromator* can be found in Honkimäki, V. et al. (2006). *J. Synch. Rad.* **13**, 426.

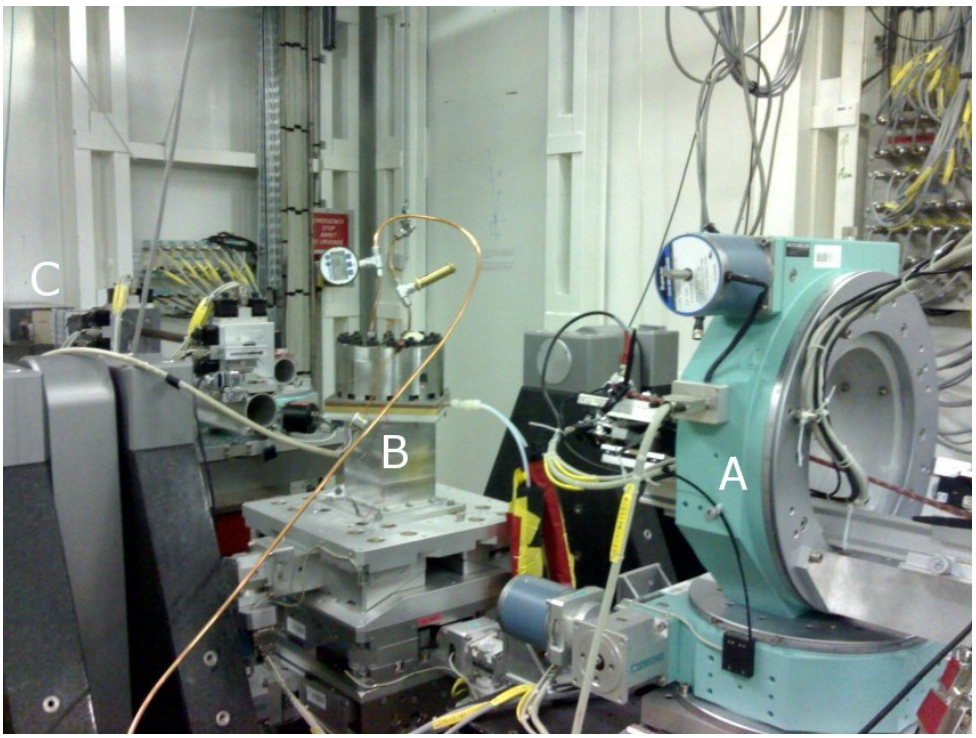

(a) Photograph of the experimental setup. The *liquid monochromator* (A), the sample cell together with a height adapter and copper pipe fixed on the top of the cell for gas inlet (B), and the detector (C) are visible.

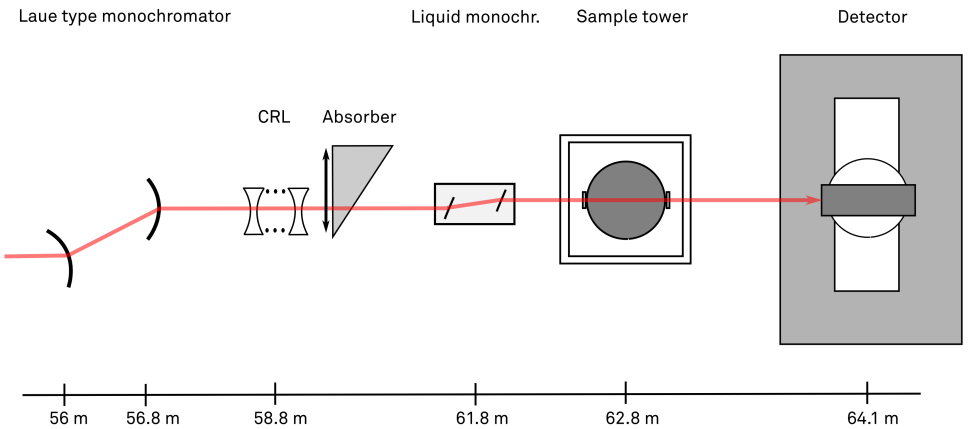

(b) Schematic drawing showing the components of the HEMD setup for liquid surfaces (top view). Some components, e.g. diodes, are not shown. The approximate positions of components are given with respect to the origin of the beam (shown as red line).

Figure 3.7: Experimental setup for high energy x-ray reflectivity at ID15A.

x-rays are necessary. In contrast to x-ray reflectivity measurements, a small sample volume is required to reduce the penetration path through the sample. Hence, new sample cells had to be designed. These are discussed in this section, followed by a description of the experimental set-ups at DELTA and ESRF.

Sample cells

For x-ray diffraction measurements at BL9 of DELTA, a new cell, based on the reflectivity cell described in section 3.3.1 was designed, see Fig. 3.8a. The width of the sample volume is 4 cm. The cell consists of 2 cm thick stainless steel walls, the cap (thickness 15 - 17 mm) is fixed with ten M10 bolts. Similar to the reflectivity cell, 5 mm wide and 25 mm high openings were milled out at opposing positions at the cell. 1 mm thick aluminum windows are screwed on these openings with 16 M3 bolts. Here the beam penetrates the cell. Such a window design increases the effective beam path through the sample to 8 cm. To decrease it to 4 cm, Polyimid foils where glued inside the cell covering approximately 70% of the height of the openings. Since scattering from various positions of the samples and thus different distances to the detector results in inaccuracies in the determination of scattering angles, a thinner sample provides a higher space resolution on the detector. Therefore, an aluminum inset was built which decreases the sample thickness to 6 mm. Using this option, the aluminum windows are redundant, as this inset is milled to a thickness of 1 mm at the window positions.

The sample temperature is measured by two Pt100 elements using a Lakeshore temperature controller. The sample cell is cooled by a cooling plate placed under the sample which is flushed by a water - glycol mixture. A heating foil is positioned between cell and cooling plate. Thus, a temperature stability of approximately 0.01 K was achieved during the measurements.

An adapted version of this sample cell was designed for the x-ray diffraction measurements performed at beamline ID15B of ESRF, see Fig. 3.8b.[48] This cell consists of a specific aluminum alloy that has a similar durability as stainless steel, with the advantage of a lower attenuation of x-rays. Another advantage of this cell design is the redundancy of windows and thus potential pressure leaks. To decrease shadowing of the scattered x-rays due to the narrow windows the second window is milled cone-shaped with an opening angle of 32°. Furthermore, this cell allows to check the sample optically during the experiment by two 30 mm thick Plexiglas windows. The sample temperature was measured and controlled in a similar way as for the other cell.

[48] A detailed description of this cell can be found in Conrad, H. (2007). "Tetrahydrofuran clathrate hydrate formation studied by X-ray Raman scattering." Diploma thesis. Technische Universität Dortmund.

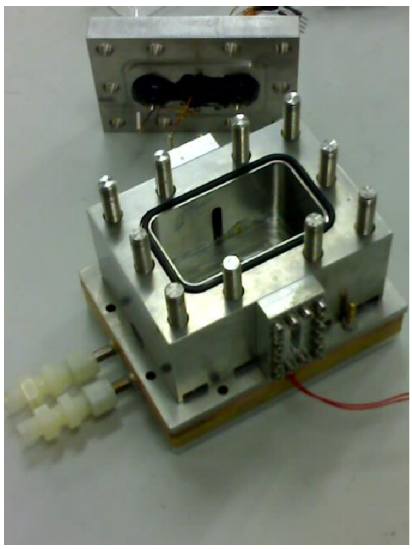

(a) Opened sample cell for diffraction experiments at BL9 of DELTA. The Pt100 sensors are visible at the cap.

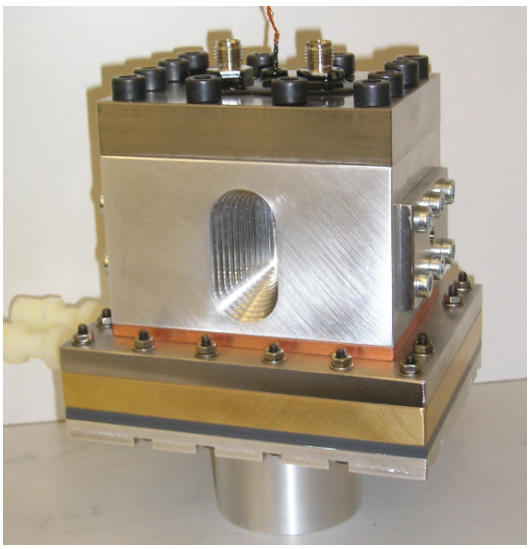

(b) Sample cell for diffraction experiments at ID15B of ESRF. A mounting of a Plexiglas window can be seen at the right side.

Figure 3.8: Sample cells for diffraction experiments at liquid-liquid interfaces.

Diffraction setup at BL9 of DELTA

Parts of the x-ray diffraction measurements were performed at the multiple purpose beamline BL9 of DELTA, using the set-up for wide and small angle x-ray scattering, see Fig. 3.9.[49] At this beamline, the x-ray beam is produced by a superconducting asymmetric wiggler (SAW) with a critical energy of $E_c = 7.9$ keV. The beam is monochromatized by a Si(311) double-crystal monochromator, allowing x-ray energies between 4 keV and 30 keV. In order to penetrate both aluminum windows and the liquid-liquid interface, a energy of $E = 27$ keV was chosen, yielding a total x-ray transmission of approximately 10%. At this energy a typical photon flux of approximately $7 \cdot 10^8$ $s^{-1}mm^{-2}$ at a storage ring current of 100 mA is obtained.[50] The incoming beam size is defined by several slits (Entrance, B, and D in Fig. 3.9b) to a beam size of 0.2×1 mm^2 (v×h). An auto-absorber system allows to limit the count rate for the detector, the fast shutter system blocks the beam quickly without closing the main shutter to protect the detector from overexposure. The incident beam intensity is monitored before and behind the absorber system. Behind the sample, a MAR345 image plate detector is placed to detect a full diffraction pattern within short time scales in the range of minutes. This detector has an active area of 345 mm diameter and allows a minimum pixel size of $100 \times 100\,\mu m^2$. Here, a pixel size of $150 \times 150\,\mu m^2$ was used resulting in significant shorter read out times of approximately 90 s. A small beam stop made of lead was placed in front of the detector at the position of the direct beam. The detector was placed as close as possible at

[49] Details for this set-up are given in Krywka, C. et al. (2007). *J. Synch. Rad.* **14**, 244.
[50] Paulus, M. et al. (2008*b*). *J. Synch. Rad.* 15, 600.

a distance of $d_{\text{sam-det}} \approx 35$ cm behind the sample, in order to gain a large q-range

Diffraction setup at ID15B of ESRF

In general, the diffraction set-up at ID15B is similar to the set-up at BL9. An overview on the properties of ID15B can be found in section 4.5.1. The important differences between both set-ups are the higher energy of $E = 87$ keV and the use of the fast Thales Pixium 4700 detector at ID15B.[51] This detector has an active area of 381.9×294.1 mm^2 at pixel sizes of $154 \times 154\,\mu$m^2. In contrast to the MAR image plate, fast read out times of a few µs allow diffraction experiments with time resolutions on the order of seconds. Due to the higher energy compared to BL9, the sample to detector distance was chosen to $d_{\text{sam-det}} \approx 117$ cm. The beam size was 0.1×0.3 mm^2 (v×h).

Experimental procedure

After the cell had been filled with water, the sample temperature was chosen to approximately $T = 273.3$ K in both experiments. The position of the interface was obtained by a height scan using a PIN diode, which was placed before the 2D detectors. This diode was moved out of the beam afterwards. CO_2 was filled into the cell at a pressure above 35 bar leading to condensation of CO_2 onto the water surface. A few mm thick macroscopic CO_2 layer was formed. Before and during the diffraction measurements, the position of the interface was checked once again using the diode. At beamline BL9, exposure times of $t_e = 20$-60 s were chosen, yielding, together with the read out time of 90 s, a diffraction pattern every 2-3 min. In contrast, at ID15B an exposure time of $t_e = 4$ s was chosen. Owing to the negligible read out times and by adding a break after each scan of 5 s, the time difference between two diffraction patterns was 9 s. Measurements were taken for a few hours using the same sample. It has to be emphasized that the sample was not mechanically disturbed in order to avoid nucleation seeds. Thus, the experiment at BL9 provides a good overview about the hydrate growth process at the interface whereas the measurements performed at ID15A are well suited for the investigation of the time evolution.

3.4 Results and discussion

In order to confirm a model describing the hydrate formation at water-CO_2 interfaces, the experimental data has to be analyzed accurately. Thus, an overview of the raw data handling and the analysis procedure of the experimental reflectivity and diffraction data is given in this chapter. Afterwards, results of the experiments at liquid-gas and liquid-liquid interfaces are

[51] Daniels, J.E. and M.Drakopoulos (2009). *J. Synch. Rad.* **16**, 463.

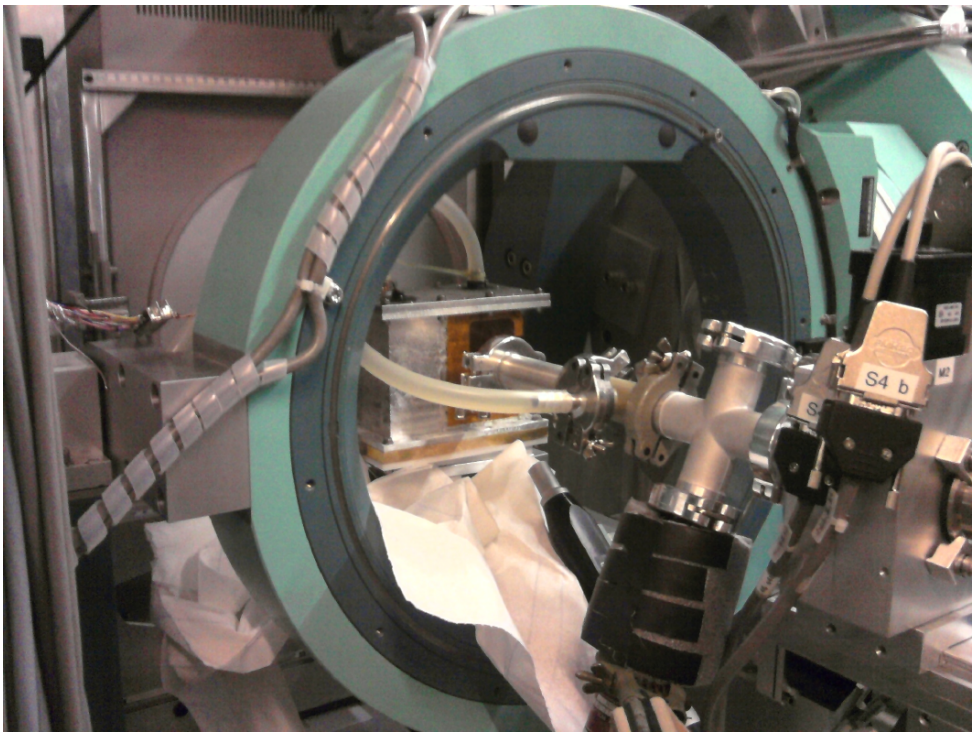

(a) Photograph of the experimental x-ray diffraction setup at BL9.

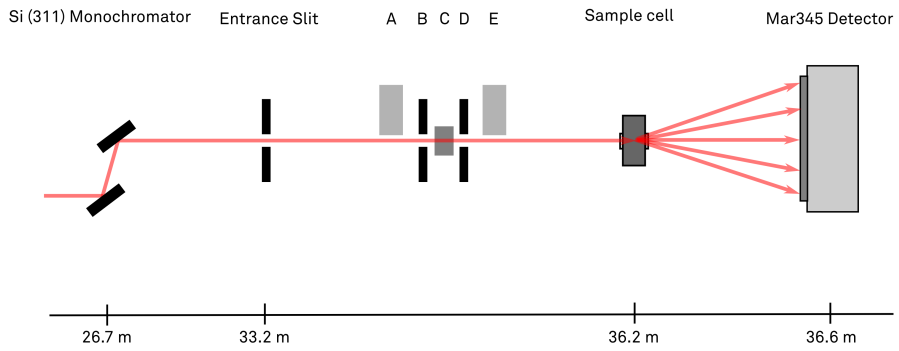

(b) Schematic drawing showing the components of the x-ray diffraction setup (top view): monitoring detectors A and E, slits B and D, and absorber/fast shutter system C. Slit D defines the beam size. The approximate distances are given with respect to the source point of the beam (shown as red line).

Figure 3.9: Experimental setup for x-ray diffraction at BL9.

discussed with respect to the formation of CO_2 hydrate. Finally, a conclusion to the hydrate formation models based on the experimental findings is stated.

3.4.1 Water - gaseous CO_2 interface

In this section, the results of the x-ray reflectivity measurements at the liquid water - gaseous CO_2 interface are presented. First, the measured reflectivities were normalized to the signal of the monitor detector. The different absorber factors were determined by measuring overlapping intervals of the incident angle for each absorber stage and the data were shifted until both intervals agreed. Afterwards, the data were corrected for diffuse scattering background by a subtraction of the corresponding signal. These corrected data were analyzed applying the effective-density-model.[52] To keep the number of free parameters small, the water roughness σ_S and dispersion δ_S were determined from the measurement at $p_{CO2} = 1$ bar. At this pressure, a pure liquid surface without adsorbed gas can be assumed within the experimental resolution. The required values for the absorption β_S were calculated from the density of water and were not changed for all measurements. These substrate values were used in the refinement of the other measurements as starting values, see Tab. 3.1. Special attention was spent on the formation of a layer above the water and its density, roughness and thickness.

Property	Water	Liquid CO_2	CO_2 hydrate
Density [g/cm^3]	0.9998	0.927	1.09-1.13[a]
Electron density [e/Å^3]	0.336	0.279	0.367[b]
Surface roughness (calculated) [Å]	3.1	12.6	–
Surface tension [mN/m]	75.64	4.54	–
Molecule radius [Å]	1.93	2.56	–

Table 3.1: Tabulated properties of water, liquid CO_2 and CO_2 hydrate at $T = 0°C$. Data taken from Lide, D.R., ed. (2003–2004). *Handbook of Chemistry and Physics*. 84th ed. Taylor & Francis; *NIST Chemistry WebBook*; Sloan, E.D. (2003). *Nature* **426**, 353. [a]Depending on the occupancy of the cavities, see Uchida, T. (1997). *Waste Management* **17**, 343. [b]Assuming the maximum possible occupancy.

As the formation of hydrate precursors or hydrate crystallites is predicted at the water-CO_2 interface, these structures would disturb the water surface. Hence, a change in the water's roughness can be interpreted as the formation of hydrate precursors or formed hydrate clusters. The first chosen pressure of 12 bar is still below the stability pressure for CO_2 hydrate, which is approximately $p_{hyd} = 12.5$ bar at the chosen temperature, see section 2.1. Thus, this

[52]See appendix A and Tolan, M. (1999). *X-ray Scattering from Soft Matter Thin Films*. Springer.

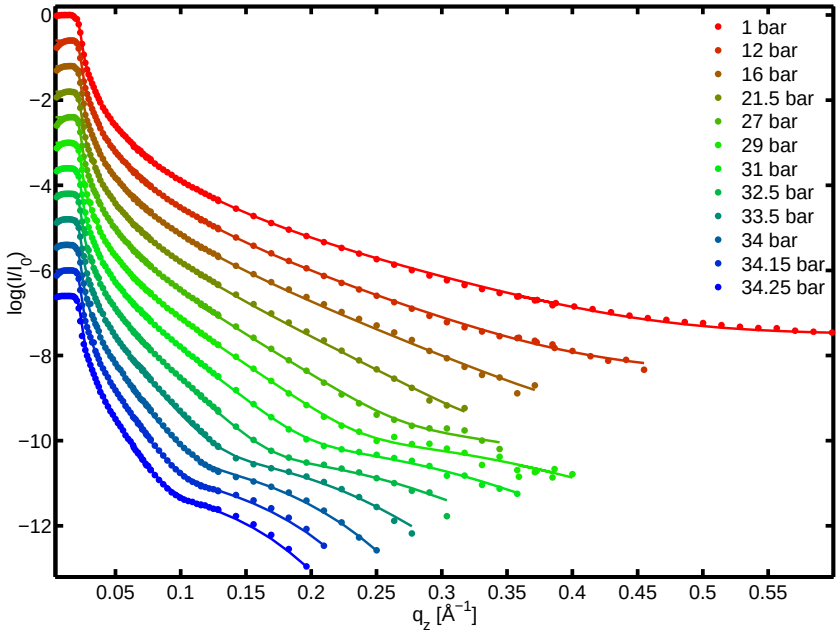

Figure 3.10: CO_2 pressure dependent reflectivities of the water-CO_2 interface. Solid lines represent corresponding fits. For clarity, the curves are shifted.

measurement acts as reference without occurrence of hydrate or hydrate precursors which can only form at higher pressures.

The experimental data, together with the refinements, are presented in Fig. 3.10 as function of the wave vector transfer q_z for all measured pressures. Approximately eight orders of magnitude of intensity are accessible at lower CO_2 pressures, while due to the increasing absorption of the denser gas phase and increased diffused scattered x-rays at higher pressures, only seven orders of magnitude are accessible. Thus, a decreasing q_z-range can be examined with rising pressure. The good agreement of experimental data and refinement is emphasized by normalizing the reflectivity to Fresnel reflectivity, see Fig. 3.11a. Thus, the box model, i.e. a constant electron density of the adsorbed layer, together with tanh-shaped interfaces for modelling the electron density, is fully sufficient for the analyzed sample system. The resulting electron density profiles of the samples are shown in Fig. 3.11b. At $p_{CO2} = 1$ bar an electron density of $\delta_S = (0.335 \pm 0.008)$ e/Å^3 and a roughness of $\sigma_S = (3.2 \pm 0.1)$ Å was refined for the water substrate. Both agree with the tabulated value $\delta_W = 0.336$ e/Å^3 and the capillary wave roughness calculated from Eq. 3.24 of $\sigma_W = 3.1$ Å for the given experimental set-up with $q_{lc} \approx 4 \cdot 10^4$ m^{-1}. This result supports the assumption that no significant gas adsorption, which would lead to a larger surface roughness, occurs at this pressure.

Assuming the formation of a layer on the water surface, no increase in the water roughness with increasing CO_2 pressure is found. Most importantly, this is also the case at pressures that allow the formation of gas hydrates. From $p_{CO2} = 27$ bar on, the formation of a layer is clearly visible in the oscillations of the reflectivity curves. Note that at lower pressures, a refinement

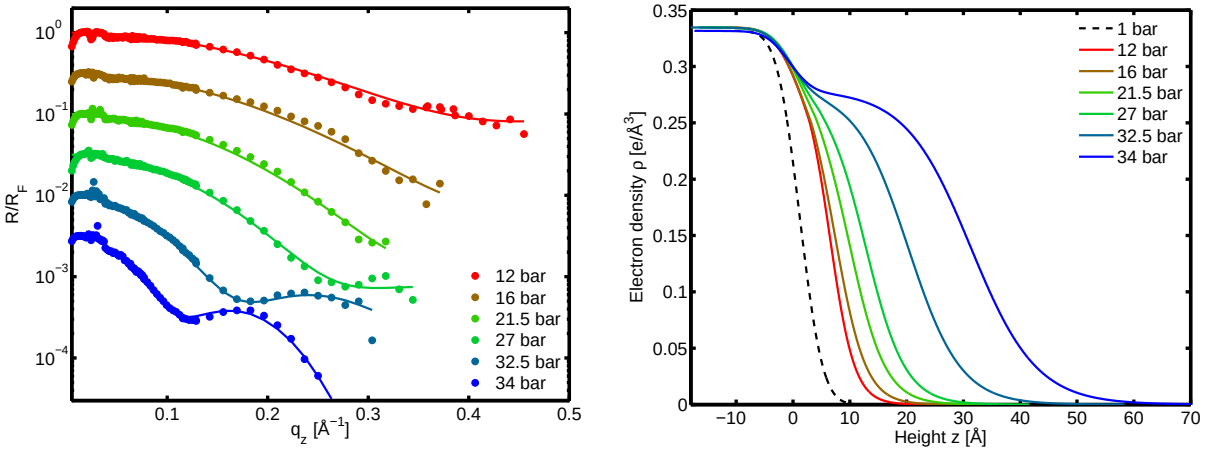

(a) Reflectivities normalized to Fresnel reflectivity R_F. Solid lines represent fits, the curves are shifted for clarity.

(b) Corresponding electron density profiles.

Figure 3.11: Normalized reflectivities and corresponding electron density profiles of selected pressures.

without a CO_2 layer is also possible, resulting in an increase of the surface roughness. However, at least for $p_{CO2} = 12$ bar such an increased surface roughness cannot be explained by a formation of hydrate precursors as described above. Therefore, the decreased intensity compared to $p = 1$ bar can only be attributed to the formation of a thin CO_2 layer. Moreover, as adsorption theory predicts the adsorption of gas molecules with rising pressure[53] this process has to be taken into account in any case. The layer thickness increases as a function of CO_2 pressure, whereas its electron density stays constant at $\delta_L = (0.282 \pm 0.008)$ e/Å^3, see Fig. 3.11b. This value is in very good agreement to liquid CO_2, see Tab. 3.1. Furthermore, as the density of CO_2 hydrate is approximately 30% higher than the measured value,[54] the pure adsorption of CO_2, instead of CO_2 hydrate formation and growth, was observed. The roughness σ of the adsorbed layer increases from (3.8 ± 0.3) Å at $p_{CO2} = 12$ bar to (11.3 ± 1.0) Å at $p_{CO2} = 34.25$ bar. To understand the nature of the increase of layer thickness and layer roughness, the following analysis is focused on these properties in the framework of adsorption and capillary wave theory as presented in chapter 3.2.

The layer thickness as a function of CO_2 pressure is shown in Fig. 3.12a. It can be estimated with an accuracy of $\Delta l_m = 0.7$-1 Å. At pressures near the condensation pressure p_0, the thickness increases rapidly. Following Eq. 3.21, an adsorption isotherm can be fitted to the data yielding an effective Hamaker constant of $A_{eff} = (-3.2 \pm 0.5) \cdot 10^{-19}$ J. This result deviates approximately by one order of magnitude from the calculated value using Eq. 3.20 of $A_{eff,th} = -3.09 \cdot 10^{-20}$ J. Here, $\epsilon_{CO2} = 1.57$ and $n_{CO2} = 1.55$ were used for liquid CO_2.[55] How-

[53] Paulus, M. et al. (2005). *Phys. Rev. E* **72**, 061601.
[54] Uchida, T. (1997). *Waste Management* **17**, 343; Aya, I. et al. (1997). *Energy* **22**, 263.
[55] May, E.F. et al. (2005). *Int. J. Thermophys.* **26**, 563; Tuan, D.Q. and Ilangantileke, S.G. (1997). *J. Food Engeneer-*

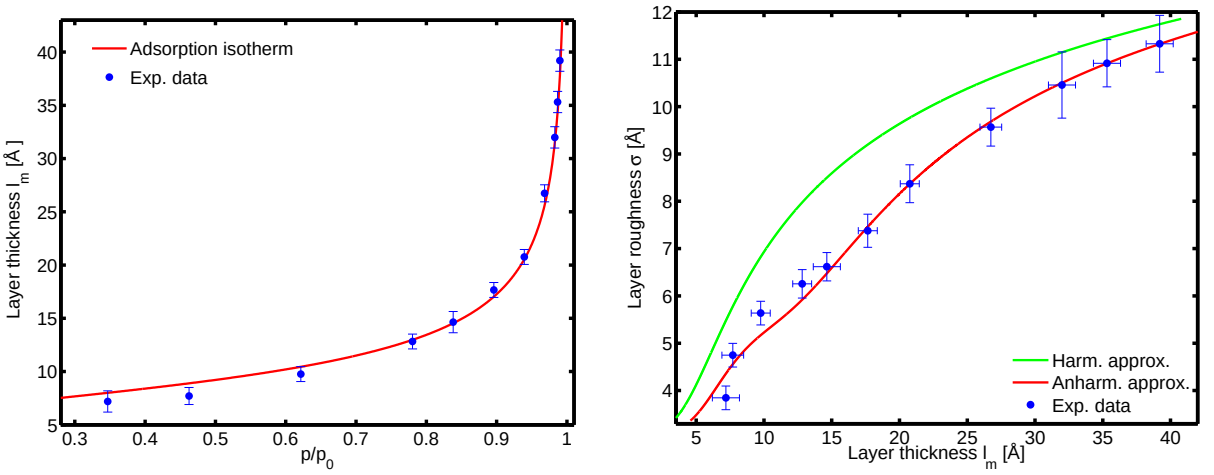

(a) Adsorption isotherm. **(b)** Layer roughness as a function of layer thickness.

Figure 3.12: Adsorption isotherm and layer roughness as function of layer thickness. The experimental data was obtained from the refinements of the reflectivities.

ever, the theoretical formula for calculation of the effective Hamaker constant gives only an estimation and fails also for other sample systems.[56] For calculation of $A_{\text{eff,th}}$, macroscopic obtained values of liquid CO_2 had to be used, which differ from the properties of thin films.[57]

In the framework of capillary wave theory a deeper analysis of the layer properties is performed in the following. Therefore, the layer roughness is analyzed as a function of the layer thickness, see Fig. 3.12b. As in other adsorption studies,[58] the roughness of the layer reaches the bulk value (see Tab. 3.1) at pressures near the condensation pressure p_0. The harmonic approximation fails to describe the experimental data, in agreement with several other studies, see section 3.2.2. The extension to the anharmonic approximation yields a very good agreement with the experiment. Using Eq. 3.30, the Hamaker constant in the framework of the anharmonic approximation is refined to $A_{\text{eff,anharm.}} = (-8.0 \pm 1.0) \cdot 10^{-19}$ J. This value is about a factor of two larger than the conventionally fitted value but does also not agree with the theoretical value. By the refinement of Eq. 3.29 the surface tension of the adsorbed layer can be determined to $\gamma_L = (1.75 \pm 0.1)$ mN/m. This deviation from the bulk value of $\gamma_{CO2} = 4.5$ mN/m by a factor $\simeq 2.5$ was reported to be a property of thin adsorbed liquid films.[59] However, this behavior has not been fully understood so far.

Owing to the very good agreement with adsorption and capillary wave theory, the pure adsorption of CO_2 instead of the formation of gas hydrate or hydrate precursors was found.

ing **31**, 47.

[56] See, e.g., Paulus, M. et al. (2005). *Phys. Rev. E* **72**, 061601; Lietz, D. (2007). "Hochenergiereflektometrie an Festkörper-Gas und Festkörper-Flüssigkeits-Grenzflächen." Diploma thesis. Universität Dortmund for an overview.

[57] Paulus, M. (2006). "Röntgenstreuung an Flüssigkeits-Gas Grenzflächen." PhD thesis. Universität Dortmund.

[58] See Paulus, M. et al. (2005). *Phys. Rev. E* **72**, 061601; Paulus, M. et al. (2008*c*). *Surf. Interface Anal.* **40**, 1226 and references therein.

[59] See for instance Paulus, M. et al. (2005). *Phys. Rev. E* **72**, 061601 and references therein.

The adsorbed CO_2 film shows similar characteristics as observed in other systems. Since hydrate precursors should form instantaneously after the adsorption of a few nm thick liquid CO_2 layer,[60] a hydrate formation without hydrate precursors at the water-CO_2 liquid-gas interface is supported. In order to generalize these findings, x-ray diffraction measurements at the liquid-liquid water-CO_2 interface has also been performed.

3.4.2 Water - liquid CO_2 interface

Due to the similar density of liquid water and liquid CO_2, measurements of x-ray reflectivities at this interface are in general very challenging concerning the sample environment. Furthermore, the electron density difference between both phases is only $\Delta\rho = 0.058$ e/Å^3 (see Tab. 3.1), yielding a significantly smaller critical angle compared to the liquid-gas interface which cannot be separated from the incident beam. Therefore, x-ray diffraction measurements in transmission geometry were performed at the liquid-liquid interface.

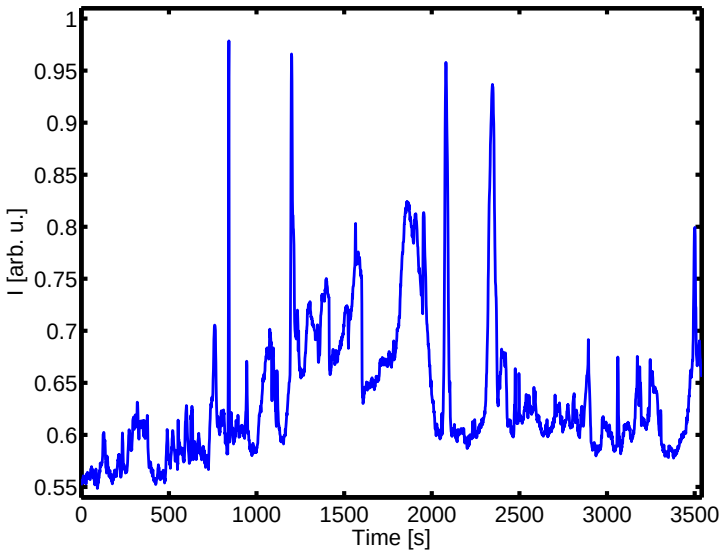

Figure 3.13: Timescan of the (231) Bragg reflection of CO_2 hydrate measured at the liquid-liquid interface.

For this purpose, the CO_2 pressure was raised to $p_{CO2} = 36$ bar, resulting in a macroscopic thick liquid CO_2 layer. Afterwards, the point detector was set to the angle of the expected (231) Bragg reflection of CO_2 hydrate which is the reflection with the highest intensity.[61] Then a timescan with 1 s stepsize was performed. The results are shown in Fig. 3.13. Here, the occurrence of hydrate Bragg reflections is shown as a very dynamic process. In particular, the very intense reflections, e.g. after 840 s and 2080 s, are only visible for 3-15 s. Besides,

[60] Kvamme, B. (2000). *Annals of the New York Academy of Science* **912**, 496; Sloan, E.D. and Koh, C.A. (2008). *Clathrate Hydrates of Natural Gases*. 3rd ed. CRC Press Inc.

[61] See Takeya, S. et al. (2006). *Chem. Eng. Sci.* **61**, 2670 and appendix C.

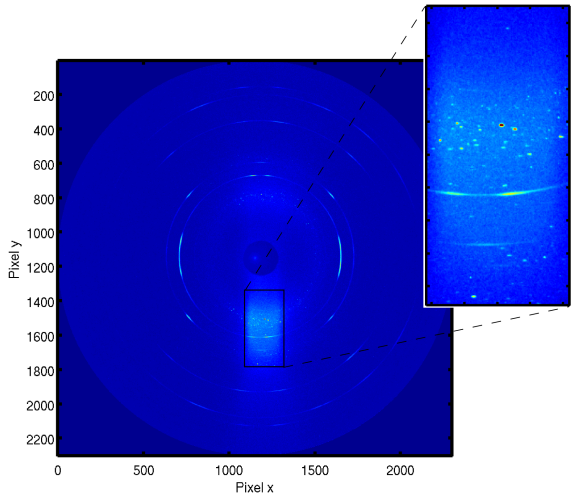

(a) Full MAR345 diffraction pattern. Due to shadowing from the sample cell, Bragg reflections from CO_2 hydrate are only visible in a small area which is shown as enhancement.

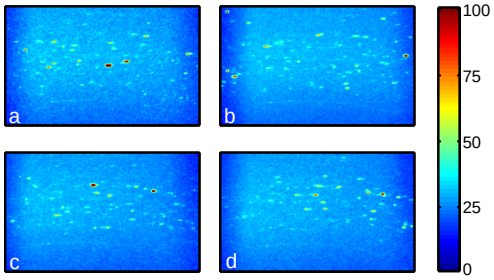

(b) MAR345 Diffraction images showing the region where the (231) reflection is observed. The intensity scale (arbitrary units) is presented right. (a) After filling with CO_2. (b) After 60 min. (c) 95 min. (d) 97 min.

Figure 3.14: MAR345 diffraction patterns measured at the liquid-liquid interface. The textured rings are originated from scattering from the aluminum windows, the light blue colored area around the peaks represents the liquid structure factor.

also longer living reflections were detected, e.g. after 1860 s. These reflections were visible for approximately 100 s. Summing up, the formation of CO_2 hydrate crystallites at the interface was observed. However, it is not obvious why these reflections occur and disappear. The most likely reasons for these dynamics are movements of small hydrate crystallites at the interface or a descent into the water phase. Therefore, diffraction experiments using 2D detectors were performed.

In Fig. 3.14a a full MAR345 spectrum taken at BL9 of DELTA is shown. Owing to the narrow windows of the cell (see section 3.3.2), the cell shadows a large part of the detector and thus only a small rectangular part of the image can be used which is shown as enhancement. As mentioned in section 3.3.2, a new diffraction pattern was recorded approximately every 2-3 min at the liquid-liquid water-CO_2 interface. Bragg reflections originating from CO_2 hydrate were visible from the first diffraction pattern, less than 10 minutes after the liquid CO_2 was adsorbed onto the water surface. As proposed from the timescan in Fig. 3.13, only several peaks originated from individual crystallites instead of Debye-Scherrer like powder rings are observable. The dynamics of the peak formation are presented in Fig. 3.14b. Here, the region of the (213) reflections is shown. The reflections cannot be indexed because of the sample cell's thickness of 4 cm yielding an angular accuracy of $\Delta\theta \approx \pm 1°$. Hence, in the shown region also other reflections can be observed, such as the (222) and (203) Bragg reflection (see appendix C). Various reflection peaks can be observed on the one pattern and disappear in the following

pattern. It can be deduced that hydrate crystallites form stochastically. Most importantly, even after approximately two hours this dynamic process does not change significantly and thus no macroscopic freezing could be observed on these time scale. However, the used time resolution do not allow a further estimation of the mobility of the formed crystallites and the dynamics of the formation process. For this issue, diffraction experiments with the fast Pixium detector were performed. Here, similar to the experiments with the MAR image plate and the point detector, Bragg reflections occur and disappear during the whole experiment. In these patterns three different kinds of hydrate Bragg reflections can be classified:

- Long living reflections visible in many pattern.
- Very strong reflections occurring and disappearing during a few patterns.
- Weak reflections only observable in single patterns.

This fully agrees with the measurements using the point detector, where the weak reflections were difficult to separate from the background. Moreover, the weak reflections cannot be classified sufficiently because they are suppressed compared to the signal originated from the aluminum windows. By using, e.g., thinner windows or an amorphous window material a more detailed analysis of such weak reflections will become possible.

The long living reflections can be interpreted as grown crystallites whose dynamics have become rigid, e.g. because it grows at the windows. In contrast, the strong reflections represent moving crystallites or the formation process of such an crystallite which fulfills the Bragg conditions for a short time. The same behavior should be observable for smaller crystallites leading to the weak peaks.

For a fundamental analysis, a series of diffraction patterns covering 300 s was integrated, see Fig. 3.15. Although the detailed formation of a single crystallite is inhibited by such a representation, the changes with time are clearly visible. As the sample cell was thinner and the distance between sample and detector was larger compared to the measurements at DELTA, the angular accuracy can be neglected and the reflections can be indexed. All observed reflections can be linked with a CO_2 hydrate structure as indexed. Reflections without index are higher order reflections from the aluminum windows due to scattering of higher harmonic x-rays.[62] In particular, Bragg reflections originated from hexagonal ice were not observed. In Fig. 3.15 several peaks are only visible in one pattern, whereas the peaks with high intensities are observable in a few patterns. Furthermore, the hydrate (112) reflection can be observed during the complete series. This is in agreement with the classification done before.

[62] For example, the peak at $q \approx 2.25$ Å^{-1} fits to the (313) aluminum reflection assuming scattering of the 3rd harmonic. Such peaks can in principle be eliminated by an appropriate background substraction which was, however, not possible because the beam was moving slightly during the experiment. This was leading to a slight change of the exposed sample position and thus differences in the peak intensity. Therefore, the correction was not performed which has moreover no influence on the hydrate formation study.

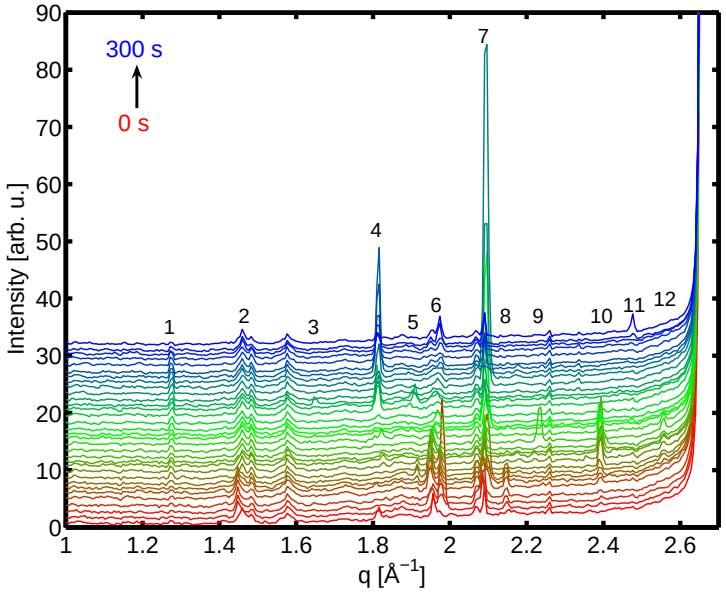

Figure 3.15: Integrated diffraction patterns. The time increment between two subsequent spectra is 9 s. Reflections originated from CO_2 hydrate are indexed from 1 - 12, corresponding to the following reflections (order 1-12): (112), (202), (103), (222), (203), (231), (004), (104), (033)/(114), (214), (323), (224). Starting at $q = 2.6$ Å^{-1} the Al (111) reflection becomes dominant.

3.4.3 Conclusions

With respect to the gas hydrate formation process the liquid-gas water-CO_2 interface shows in comparison to the liquid-liquid interface a very different behavior. The adsorption of gas molecules on the water surface leads in principle to a high supply of CO_2 at the surface but does not trigger the gas hydrate formation process. However, neither hydrate nor hydrate precursor formation could be observed. Instead, the reflectivity curves indicate the pure adsorption of a liquid-like CO_2 layer on the water surface which shows thicknesses and roughnesses in agreement with adsorption and capillary wave theory. These observations are also in agreement with a study of the water-propane interface.[63] In contrast, the formation of CO_2 hydrate crystallites was observed at the water-liquid CO_2 interface. Here, the presence of a macroscopic amount of liquid CO_2 induces the local formation of mobile CO_2 hydrate crystallites. Differing from Koh et al.[64] the sample was not disturbed and shows thus hydrate formation without offering nucleation seeds. Obviously, this formation at the interface happens fully stochastically and was found to start directly after formation of the macroscopic thick CO_2 layer.

Owing to the absence of any hydrate precursors at the liquid-gas interface, the instant, stochastically distributed formation of hydrate crystallites at the liquid-liquid interface, a hy-

[63] Paulus, M. et al. (2008*c*). *Surf. Interface Anal.* **40**, 1226.
[64] Koh, C.A. et al. (1996). *J. Phys. Chem.* **100**, 6412.

drate formation model without precursors like the local structuring hypothesis is favored. The formation on locally limited areas suggests a rather stochastic process in contrast to the cluster models proposed by Sloan, Rodger, and Kvamme.[65] Various Bragg reflections with different lifetimes and intensities were measured, suggesting the spontaneous and local occurrence of different crystallites. However, these findings are limited to CO_2 so far and have to be compared with, e.g. other hydrate former.

[65] Sloan, E.D. and Koh, C.A. (2008). *Clathrate Hydrates of Natural Gases*. 3rd ed. CRC Press Inc.; Rodger, P.M. (1990). *J. Phys. Chem.* **94**, 6080; Kvamme, B. (2000). *Annals of the New York Academy of Science* **912**, 496.

4 Formation and configurational energetics of tetrahydrofuran hydrate

Differing from most of gaseous guests enclosed in hydrates, tetrahydrofuran (THF) hydrate is built up from a liquid mixture of THF and water. THF forms the hydrate structure sII and occupies only the large cages because of its molecular diameter of approximately 5.9 Å,[1] see Fig. 4.1. This makes THF hydrate a promising candidate for gas storage where the gas molecules, e.g. H_2 or CO_2, can occupy the small 5^{12} cavities. As pure THF hydrate can easily be synthesized, its properties have been analyzed in many studies. Thus, it often acts as a prototype for the studies of hydrates. For THF hydrate, the hydrate formation can be studied from a liquid mixture bulk sensitively in contrast to other guests such as CO_2. Changes in the local structure can be analyzed to study the formation of hydrate precursors and possible structural changes in THF hydrate. This is allowed by the use of non-resonant inelastic x-ray scattering from core shell electrons, i.e. x-ray Raman scattering, at the oxygen K-edge and Compton scattering which probe bulk properties of the sample on molecular length scales.

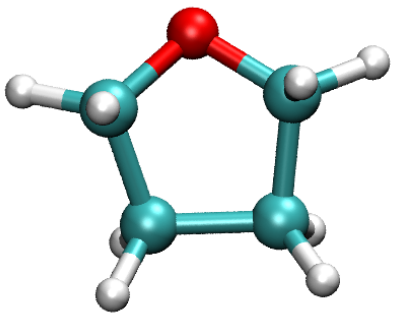

Figure 4.1: Tetrahydrofuran molecule (C_4H_8O). Due to its size the molecule does only fit in the large $6^4 5^{12}$ cavity of the hydrate structure sII. Turquoise balls represent carbon atoms, white balls hydrogen, and the red ball oxygen.

Furthermore, structural changes of THF hydrate at low temperatures can be investigated by these techniques. As discussed in section 2.1.3, the dynamics of guest molecules may freeze at low temperatures. MD simulations of THF hydrate show that the orientation of the

[1] Prasad, P.S.R. et al. (2007). *Spectrochim. Acta, Part A* **68**, 1096.

guest molecule is isotropic near the dissociation temperature, while at $T \leq 100$ K the guest molecules prefer only a few orientations.[2] At approximately $T = 10$ K the guest molecules become fully rigid with fixed orientation.[3] Such a behavior is supported by neutron diffraction experiments which show a constant lattice parameter of THF hydrate below $T \approx 75$ K.[4] The dynamics of the guest and host molecules and thus of the guest-host interaction have been studied in several nuclear magnetic resonance (NMR) experiments.[5] As a main result, the freezed dynamics of the guest molecule, mainly THF, was demonstrated by larger correlations times at lower temperatures. In order to expand these findings, Compton scattering experiments can be used to study weak changes in structure or guest-host interaction in THF hydrate originated by, e.g. an orientational change of guest molecules as function of temperature. Furthermore, Compton scattering offers the possibility to extract thermodynamic properties of THF hydrate by investigating the sample on molecular length scales in contrast to conventional calorimetric techniques. Thus, the reported anomaly of thermodynamic properties as discussed in section 2.1.4 can be studied on these length scales which are otherwise only accessible by simulations.

In this chapter, first a theoretical overview on non-resonant inelastic x-ray scattering is given including x-ray Raman and Compton scattering. The computational methods which allow the calculation of XRS and Compton spectra are discussed. Afterwards, recent x-ray spectroscopy studies on the local structure of water and ice are presented to show how these methods can be used to investigate the hydrate formation process and to develop a fundamental background for the analysis of the measurements of the THF-water mixture and THF hydrate. In the subsequent section the sample cells used in the experiments are presented. In the following two sections, the experimental set-ups and the results of the XRS and Compton scattering measurements are discussed. Finally, the results are summarized and discussed with respect to the hydrate formation process and structural changes in the hydrate as function of temperature.

4.1 Theory of non-resonant inelastic x-ray scattering

Inelastic x-ray scattering has become a very powerful tool to study electronic and structural properties of matter.[6] In inelastic x-ray scattering experiments, an incoming photon with

[2] Alavi, S. et al. (2006). *J. Chem. Phys.* **124**, 014704.
[3] Garg, S.K. et al. (1974). *J. Magn. Reson.* **15**, 295.
[4] Jones, C.Y. et al. (2003). *J. Phys. Chem. B* **107**, 6026.
[5] See e.g. Garg, S.K. et al. (1974). *J. Magn. Reson.* **15**, 295; Garg, S.K. et al. (1978). *J. Magn. Reson.* **31**, 399; Jacobs, D.M. et al. (1997). *J. Phys. Chem. A* **101**, 5241; Nowaczyk, A. et al. (2009). *Phys. Rev. B* **80**, 144303 and references therein.
[6] A comprehensive overview is given by Schülke in Schülke, W. (1991). "Inelastic scattering by electronic excitations."*Handbook on Synchrotron Radiation*. Ed. by Brown, G.S. and Moncton, D.E. North-Holland and Schülke, W. (2007). *Electron Dynamics by Inelastic X-ray Scattering*. Oxford University Press.

wave vector $\vec{k}_1$ and energy $\hbar\omega_1$ is scattered by the sample into a photon with wave vector $\vec{k}_2$ with energy $\hbar\omega_2$. The probed length scale is given by $2\pi/q$ with the modulus $q = |\vec{q}| = \sqrt{\omega_1^2 + \omega_2^2 - 2\omega_1\omega_2\cos(\theta)}$ of the wave vector transfer $\vec{q} = \vec{k}_1 - \vec{k}_2$ at the scattering angle θ resulting in a momentum transfer $\hbar\vec{q}$. Excitations are analyzed via the energy transfer $\hbar\omega = \hbar\omega_1 - \hbar\omega_2$ to the sample. A schematic drawing of the scattering process is shown in Fig. 4.2.

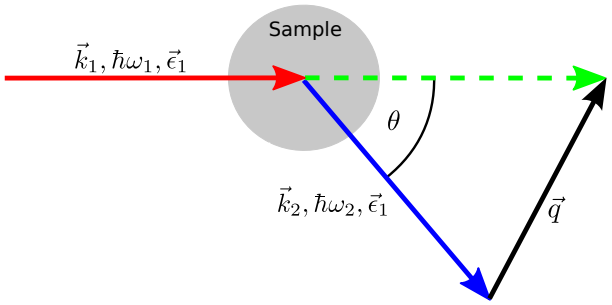

Figure 4.2: Schematic drawing of the inelastic scattering process. $\vec{\epsilon}_1, \vec{\epsilon}_2$ are the photon polarization vectors of the incoming and scattered x-rays.

The measured quantity in inelastic x-ray scattering experiments is the double differential scattering cross section (DDSCS) $\frac{d^2\sigma}{d\Omega_2 d\hbar\omega_2}$ which denotes the current of photons scattered into the solid angle element $[\Omega_2, \Omega_2 + d\Omega_2]$ and into the energy range $[\hbar\omega_2, \hbar\omega_2 + d\hbar\omega_2]$ normalized to the incident current relating to the solid angle element $d\Omega_2$ and the energy element $d\hbar\omega_2$.

From the theoretical point of view, the DDSCS is usually treated in lowest order perturbation theory from the Hamiltonian H_{int} describing the interaction between an electromagnetic field and the sample's electrons by application of Fermi's golden rule. In the non-relativistic case H_{int} can be written as[7]

$$H_{\text{int}} = \sum_j \frac{e^2}{2m_e c^2} \vec{A}_j^2 + \sum_j \frac{e}{m_e c} \vec{p}_j \cdot \vec{A}_j, \tag{4.1}$$

where e is the electron's charage, m_e its mass, $\vec{A}_j$ the vector potential of the electromagnetic field, and $\vec{p}_j$ the momentum of the jth electron. In the first order perturbation theory, the first term in Eq. 4.1 describes non-resonant inelastic scattering processes and for $\omega_1 = \omega_2$ elastic scattering. Since the second term only contributes in second-order perturbation theory, it gives rise to resonant inelastic scattering for incident energies $\hbar\omega_1 \approx E_B$ with E_B the binding energy of a bound electron. In this thesis only non-resonant inelastic x-ray scattering (NRIXS) is applied so that the following discussion focuses only on the derivation of the

[7] Hämäläinen, K. and Manninen, S. (2001). *J. Phys.: Condens. Matter* **13**, 7539.

non-resonant part of the DDSCS, which can be expressed in the Born approximation[8] by

$$\left.\frac{\mathrm{d}^2\sigma}{\mathrm{d}\Omega\mathrm{d}\hbar\omega_2}\right|_{\mathrm{NR}} = r_e^2(\vec{\epsilon}_1\cdot\vec{\epsilon}_2)^2\left(\frac{\omega_2}{\omega_1}\right)\sum_{\mathrm{i,f}}\left|\left\langle \mathrm{f}\left|\sum_j e^{i\vec{q}\cdot\vec{r}_j}\right|\mathrm{i}\right\rangle\right|^2\delta(E_\mathrm{f}-E_\mathrm{i}-\hbar\omega), \tag{4.2}$$

where r_e is the classical electron radius, $|\mathrm{i}\rangle, |\mathrm{f}\rangle$ are the initial and final state, respectively, and $\vec{r}_j$ is the position operator of the jth electron. The δ-function guarantees the energy conservations. Eq. 4.2 is usually written as

$$\left.\frac{\mathrm{d}^2\sigma}{\mathrm{d}\Omega\mathrm{d}\hbar\omega_2}\right|_{\mathrm{NR}} = \left(\frac{\mathrm{d}\sigma}{\mathrm{d}\Omega}\right)_{\mathrm{Th}}\frac{\omega_2}{\omega_1}S(\vec{q},\omega), \tag{4.3}$$

with the dynamic structure factor

$$S(\vec{q},\omega) = \sum_{\mathrm{i,f}}\left|\left\langle \mathrm{f}\left|\sum_j e^{i\vec{q}\cdot\vec{r}_j}\right|\mathrm{i}\right\rangle\right|^2\delta(E_\mathrm{f}-E_\mathrm{i}-\hbar\omega), \tag{4.4}$$

and Thomson's scattering cross section $\left(\frac{\mathrm{d}\sigma}{\mathrm{d}\Omega}\right)_{\mathrm{Th}}$ describing the electron-photon coupling. The dynamic structure factor $S(\vec{q},\omega)$ contains all structural information of the electronic system that can be extracted from the NRIXS spectrum. However, in experiments only finite energy and momentum transfers are achievable which can be partitioned into four cases:[9]

1. Phonon excitations: $q r_c \approx 1, \hbar\omega \approx \hbar\omega_{\mathrm{Ph}}$. The characteristic length r_c is the distance between the atoms and ω_{Ph} is the phonon frequency.

2. Valence electron excitations: $q r_c \approx 1, \hbar\omega \approx \hbar\omega_{\mathrm{P}}$. Here, r_c is an interparticle distance and ω_{P} the plasmon frequency. Thus, collective plasmon excitations and particle-hole excitations can be probed.

3. X-ray Raman scattering (XRS): Inner-shell excitations can be studied with $\hbar\omega \approx E_{\mathrm{B}}$, where E_{B} is the binding energy of the probed core electron.

4. Compton scattering: For large energy transfers $\hbar\omega \gg E_c$ and momentum transfers $q r_c \gg 1$ the ground state of the electron-momentum distribution can be investigated. Here, E_c denotes a characteristic energy of the system such as the binding energy of core electrons or the Fermi energy and r_c is again a typical particle distance.

[8] van Hove, L. (1954). *Phys. Rev.* **95**, 249.

[9] Schülke, W. (1991). "Inelastic scattering by electronic excitations."*Handbook on Synchrotron Radiation*. Ed. by Brown, G.S. and Moncton, D.E. North-Holland; Schülke, W. (2007). *Electron Dynamics by Inelastic X-ray Scattering*. Oxford University Press.

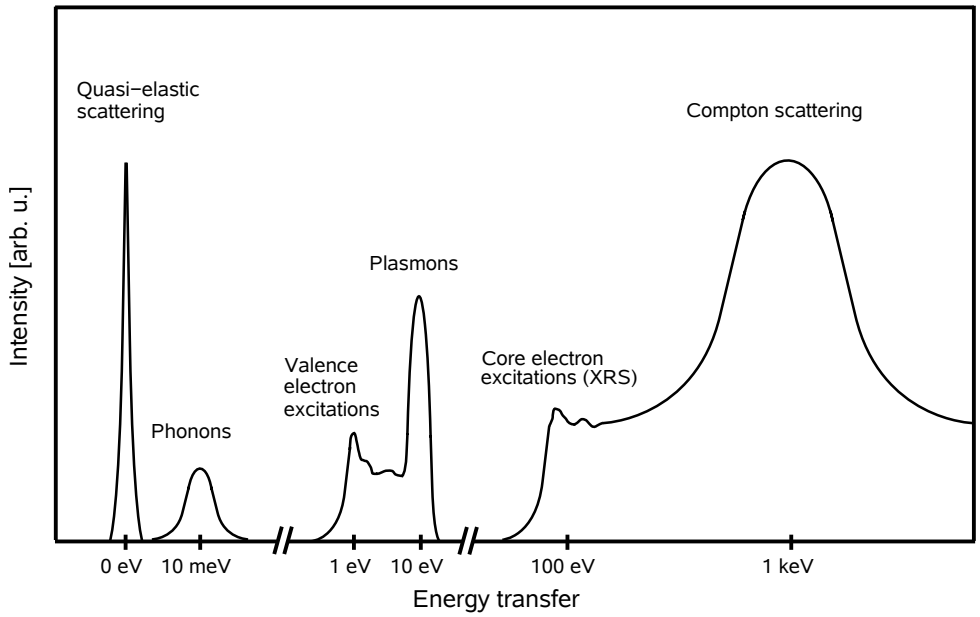

Figure 4.3: Schematic overview spectrum showing excitations obtainable by NRIXS. The energy transfers represent only the corresponding order of magnitude.

A schematic overview of these typical excitations is given in Fig. 4.3. This work focuses on XRS and Compton scattering. Thus, the further theoretical description is restricted to both cases.

4.1.1 X-ray Raman scattering

In the XRS process, the energy transfer is in the range of the binding energy of a core electron. Hence, excitations from these tightly bound states above the Fermi energy E_F are accessible. The probability for such an excitation depends on the density of unoccupied states (uDOS) and on the matrix element for the excitation channel. The matrix element in Eq. 4.4 can be expanded in a Taylor series assuming orthogonal initial and final states, yielding for a single particle

$$\langle \mathrm{f}|e^{i\vec{q}\cdot\vec{r}}|\mathrm{i}\rangle = i\langle \mathrm{f}|\vec{q}\cdot\vec{r}|\mathrm{i}\rangle - \frac{1}{2}\langle \mathrm{f}|(\vec{q}\cdot\vec{r})^2|\mathrm{i}\rangle + \mathcal{O}((\vec{q}\cdot\vec{r})^3). \tag{4.5}$$

The first term describes dipole transitions and dominates for small $\vec{q}\cdot\vec{r}$. In this so called *dipole limit* of XRS, formally the same information as for x-ray absorption spectroscopy (XAS) is obtained.

At higher momentum transfers, the contribution of the higher-order terms in Eq. 4.5 is increased and thus multipole transitions become accessible. By variation of the momentum transfer $\hbar q$ it is possible to investigate the core shell excitations symmetry selectively[10] which

[10]Soininen, J. A. et al. (2006). *J. Phys.: Condens. Matter* **18**, 7327; Sternemann, C. et al. (2008*a*). *J. Anal. At. Spectrom.* **23**, 807.

cannot be studied in XAS experiments. The probability for non-dipole transitions increases at larger momentum transfers.[11] This allows to access additional information of the sample's electronic states.[12] A quantitative analysis of the momentum transfer dependence of XRS is given by the real-space multiple scattering approach.[13] The dynamic structure factor for an isotropic sample then becomes

$$S(\vec{q},\omega) = \sum_l \left|M_l(\vec{q},E)\right|^2 \rho_l(E), \tag{4.6}$$

with the transition matrix elements $M_l(\vec{q},E)$ describing the transitions from the initial state $|\mathrm{i}\rangle$ to an excited state with energy $E = \hbar\omega + E_\mathrm{i}$ and l-type angular symmetry, and the density of unoccupied states $\rho_l(E)$. Thus, $S(\vec{q},\omega)$ is understood as a linear combination of transitions with various symmetries. If both the transition matrix elements and experimental values of $S(\vec{q},\omega)$ are known for at least several $\vec{q}$ values, the symmetry-projected unoccupied density of states (lDOS) can in principle be accessed.[14]

In the single particle approximation, the similarity for XRS for small q and XAS becomes obvious by comparing the dynamic structure factor for XRS with the cross section of XAS:[15]

$$\begin{aligned} \sigma_\mathrm{XAS}(\omega_1) &\propto \omega_1 |\vec{\epsilon}_1 \cdot \langle \mathrm{f}|\vec{r}|\mathrm{i}\rangle|^2 \delta(\hbar\omega_1 + E_\mathrm{i} + E_\mathrm{f}) \\ S_\mathrm{XRS}(\vec{q},\omega) &= |\vec{q} \cdot \langle \mathrm{f}|\vec{r}|\mathrm{i}\rangle|^2 \delta(\hbar\omega + E_\mathrm{i} + E_\mathrm{f}), \end{aligned} \tag{4.7}$$

with the energy of the initial and final state, E_i and E_f, respectively. Here, the wave vector transfer $\vec{q}$ corresponds to the polarization vector $\vec{\epsilon}_1$ in XAS, whereas the incident energy $\hbar\omega_1$ in XAS experiments is related to the energy transfer $\hbar\omega$ in XRS.[16] In XAS experiments, the incident photon energy has to be chosen in the range of the studied absorption edges. In contrast, XRS allows the free choice of the incident energy while the energy transfer is close to the electron's binding energies. Thus, especially absorption edges in the soft x-ray region can be probed bulk sensitively which is difficult to achieve by XAS because of its surface sensitivity. Due to the similarity of XRS and XAS, both the x-ray absorption near edge structure (XANES) and the extended x-ray absorption fine structure (EXAFS) can be studied by XRS. In this thesis, the XANES of the oxygen K-edge of THF-water mixtures and THF hydrate is

[11] Krisch, M.H. et al. (1997). *Phys. Rev. Lett.* **78**, 2843; Nagasawa, H. et al. (1997). *J. Phys. Soc. Jpn.* **66**, 3139.

[12] See, e.g. studies on complex materials such as Si clathrates (Sternemann, H. et al. (2007). *Phys. Rev. B* **75**, 245102) or rare-earth compounds (Gordon, R.A. et al. (2008). *Europhys. Lett.* **81**, 26004).

[13] Soininen, J.A. et al. (2005). *Phys. Rev. B* **72**, 045136; Soininen, J. A. et al. (2006). *J. Phys.: Condens. Matter* **18**, 7327.

[14] See Soininen, J. A. et al. (2006). *J. Phys.: Condens. Matter* **18**, 7327. Here, a rising number of experiments have been performed, e.g. for beryllium (Sternemann, C. et al. (2004). *Phys. Rev. B* **68**, 035111) and MgO_2 (Mattila, A. et al. (2005). *Phys. Rev. Lett.* **94**, 247003).

[15] Mizuno, Y. and Ohmura, Y. (1967). *J. Phys. Soc. Jpn.* **22**, 445.

[16] Mizuno, Y. and Ohmura, Y. (1967). *J. Phys. Soc. Jpn.* **22**, 445; Suzuki, T. (1967). *J. Phys. Soc. Jpn.* **22**, 1139.

investigated by XRS. As discussed above, to study the oxygen K-edge by XAS experiments, the incident energy has to be in the region of the edge, which is around $E = 540$ eV in this case. However, probing this absorption edge by XAS, the use of special sample environments, e.g. vacuum conditions, is required that is impractical for liquid samples. Moreover, the low penetrations depth of soft x-rays obscures studies of bulk properties, which is necessary to investigate the sample's local structure. Nevertheless, with electron energy loss spectroscopy (EELS) in principle the same information as XRS are accessible, including the possibility of q-dependent measurements. Compared to XRS, EELS has certain advantages, such as higher possible energy resolutions, but the high amount of multiple scattering events and again a limited penetration depth make EELS unpractical to study liquids and ice-like systems such as THF hydrate.[17] Therefore, more details to the interpretation of XRS data, in particular for water and ice, are presented in section 4.2

4.1.2 Compton scattering

In the regime of Compton scattering, i.e. high energy and momentum transfers, the *impulse approximation* is used to simplify Eq. 4.2.[18] By using its time-dependent formulation, the dynamic structure factor becomes

$$S(\vec{q},\omega) = \frac{1}{2\pi\hbar}\int e^{-i\omega t}\langle \mathrm{i}|\sum_j e^{-i\vec{q}\cdot\vec{r}_j} e^{iHt/\hbar}\sum_{j'} e^{i\vec{q}\cdot\vec{r}'_j} e^{-iHt/\hbar}|\mathrm{i}\rangle \mathrm{d}t. \tag{4.8}$$

The impulse approximation consists of approximating the exponentials

$$e^{iHt} \approx e^{iH_0 t/\hbar} e^{iVt/\hbar} e^{-[H_0,V]t^2/(2\hbar^2)}, \tag{4.9}$$

and

$$e^{[H_0,V]t^2/(2\hbar^2)} \simeq 1, \tag{4.10}$$

where the Hamiltonian $H = H_0 + V$ is separated into a kinematic term H_0 of a free electron and a constant potential V. The physical significance of the impulse approximation is that the scattering process is fast compared to relaxations of the system, see appendix B. Then, the excited electron can be considered as a nearly free electron.[19] Finally, the dynamic structure

[17] Sternemann, C. et al. (2008*a*). *J. Anal. At. Spectrom.* **23**, 807.

[18] See Eisenberger, P. and Platzman, P.M. (1970). *Phys. Rev. A* **2**, 415. More details on the impulse approximation are presented in appendix B. A comprehensive overview on Compton scattering is given in Cooper, M.J. et al. (2004). *X-Ray Compton Scattering*. Oxford University Press and Schülke, W. (2007). *Electron Dynamics by Inelastic X-ray Scattering*. Oxford University Press.

[19] Schülke, W. (2007). *Electron Dynamics by Inelastic X-ray Scattering*. Oxford University Press.

factor can be written as

$$S(\vec{q},\omega) = \left(\frac{1}{2\pi\hbar}\right)^3 \int |\langle \mathrm{i}|\vec{p}\rangle|^2 \delta\left(\frac{\hbar^2 q^2}{2m_e} + \hbar\vec{p}\cdot\vec{q}/m_e - \hbar\omega\right) \mathrm{d}\vec{p}, \tag{4.11}$$

with $\hbar^2 q^2/(2m_e)$ the non-relativistic Compton shift for an electron at rest and $\hbar\vec{p}\cdot\vec{q}/m_e$ the Doppler shift of an electron with momentum $\vec{p}$ in its initial state.[20]

The integrand in Eq. 4.11 represents the electron momentum density of the scattering system in the ground state $|\mathrm{i}\rangle$. Hence, it gives rise to the probability of finding the ground state electron with a given momentum $\vec{p}$. With the real space electron wave function $\psi(\vec{r})$ and its Fourier transform $\chi(\vec{p})$, the electron momentum density $\rho(\vec{p})$ is written as:

$$\rho(\vec{p}) = \left(\frac{1}{2\pi\hbar}\right)^3 |\langle \mathrm{i}|\vec{p}\rangle|^2 = |\chi(\vec{p})|^2 = \left(\frac{1}{2\pi\hbar}\right)^3 \left|\int \psi(\vec{r}) e^{-i\vec{p}\cdot\vec{r}} \mathrm{d}\vec{r}\right|^2. \tag{4.12}$$

By choosing $\vec{q}$ to point in z-direction, the DDSCS becomes

$$\frac{\mathrm{d}^2\sigma}{\mathrm{d}\Omega \mathrm{d}\hbar\omega_2} = \left(\frac{\mathrm{d}\sigma}{\mathrm{d}\Omega}\right)_{\mathrm{Th}} \frac{\omega_2}{\omega_1}\frac{m_e}{\hbar q} \iint \rho(p_x,p_y,p_z)\mathrm{d}p_x\mathrm{d}p_y = \left(\frac{\mathrm{d}\sigma}{\mathrm{d}\Omega}\right)_{\mathrm{Th}} \frac{\omega_2}{\omega_1}\frac{m_e}{\hbar q} J(p_z), \tag{4.13}$$

with the so-called (directional) Compton profile $J(p_z)$ and

$$p_z = \frac{m_e\omega}{q} - \frac{\hbar q}{2} \approx m_e c \frac{\omega_1 - \omega_2 - (\hbar\omega_1\omega_2/m_e)(1-\cos(\theta))}{\sqrt{\omega_1^2 + \omega_2^2 - 2\omega_1\omega_2\cos(\theta)}}. \tag{4.14}$$

$J(p_z)$ can be interpreted as the projection of the electron momentum density $\rho(\vec{p})$ along the direction of the wave vector transfer $\vec{q}$. The total Compton profile $J(p_z)$ consists of contributions from core and valence electrons. Here, core Compton profiles can be calculated in a sufficient approximation.[21] Finally, experimentally obtained Compton profiles have to be normalized to the number of electrons per atom N, yielding

$$\int J(p_z)\mathrm{d}p_z = N. \tag{4.15}$$

Relativistic effects

The derivation of the DDSCS has been performed in the non-relativistic case. Such a description holds in principle for incident x-ray energies $E \lesssim 15$ keV,[22] but because Compton experiments are usually performed at significantly higher energies, relativistic effects have

[20] Schülke, W. (2007). *Electron Dynamics by Inelastic X-ray Scattering*. Oxford University Press.
[21] Holm, P. and Ribberfors, R. (1989). *Phys. Rev. A* **40**, 6251.
[22] Ribberfors, R. (1975*a*). *Phys. Rev. B* **12**, 2067.

also to be taken into account. An approximate relativistic treatment yields a correction to the DDSCS[23]

$$\frac{\mathrm{d}^2\sigma}{\mathrm{d}\Omega\mathrm{d}\hbar\omega_2} = \frac{r_e^2}{2}\frac{\omega_2}{\omega_1}X(p_z)\frac{m_e}{\hbar q}J(p_z). \tag{4.16}$$

The additional factor $X(p_z)$ is calculated for linear polarization by the sum over the two polarization states of the scattered photons:

$$X(p_z) = \frac{R_1}{R_2} + \frac{R_2}{R_1} - 2\sin^2(\theta)\cos^2(\beta), \tag{4.17}$$

with β the angle between the scattering plane and the polarization vector of the incident photons and the factors R_1, R_2 given by

$$\begin{aligned} R_1 &= \hbar\omega_1(mc^2 - (\omega_1 - \omega_2\cos(\theta))\frac{p_z}{q}), \\ R_2 &= R_1 - \hbar^2\omega_1\omega_2(1-\cos(\theta)). \end{aligned} \tag{4.18}$$

For unpolarized photons, Eq. 4.17 simplifies to

$$X(p_z) = \frac{R_1}{R_2} + \frac{R_2}{R_1} - \sin^2(\theta). \tag{4.19}$$

Thus, by correcting experimental data for relativistic effects, the Compton profile can be extracted similar to the non-relativistic case.[24] In the framework of this work, the relativistic correction was performed by applying a generalization of Eq. 4.17 including summands proportional to $1/R_{1/2}^2$.[25]

Limitations of the impulse approximation: asymmetry

The Compton profile $J(p_z)$ is a symmetric function of p_z with a maximum for $p_z = 0$ a.u. in the framework of the impulse approximation. However, the measured Compton profiles show an intrinsic asymmetry that is due to the breakdown of the impulse approximation and is often separated in two parts, namely core and valence asymmetry. The core asymmetry can be estimated theoretically by performing first-order corrections to Eq. 4.9.[26] Another approach is to use the quasi-self-consistent field (QSCF) method that is based on the Born ap-

[23] Ribberfors, R. (1975*a*). *Phys. Rev. B* **12**, 2067; Ribberfors, R. (1975*b*). *Phys. Rev. B* **12**, 3136, and later confirmed by Holm, P. (1988). *Phys. Rev. A* **37**, 3706.

[24] For a more detailed overview for relativistic corrections see Cooper, M.J. et al. (2004). *X-Ray Compton Scattering*. Oxford University Press.

[25] For details see Holm, P. (1988). *Phys. Rev. A* **37**, 3706.

[26] Holm, P. and Ribberfors, R. (1989). *Phys. Rev. A* **40**, 6251.

proximation instead of the impulse approximation.[27] Experiments show that both approaches are suited to match the observed asymmetry, usually defined as[28]

$$\Delta J(p_z) = \frac{J(p_z) - J(-p_z)}{J(0)}. \tag{4.20}$$

With lower incident energies of about 10 keV and high momentum resolutions, also the Compton scattering from valence electrons shows asymmetry. The effect was studied in detail for Li and Be.[29] Such asymmetries are originated in interactions of the recoil electron with the many-particle system and particle-hole interactions. Both are thus the main contributions for element specific deviations from the impulse approximation for the valence electron system. Due to the significantly higher incident energy and lower momentum resolution used in this work, valence asymmetry is negligible.

Beside such intrinsic theoretical deviations from a symmetric profile, systematic experimental errors can yield asymmetric profiles, e.g. a change of the resolution function across the Compton profile.[30] Furthermore, multiple scattering may also give rise to an asymmetry. These contributions can be calculated numerically and the experimental data can be corrected accordingly.[31]

Extraction of thermodynamic properties

As the Compton profile of isotropic systems yields information on the radial electron momentum distribution, Epstein deduced the possibility to calculate expectation values of the momentum operator.[32] In particular, the expectation value of the electron kinetic energy $\langle T_e \rangle$ can be calculated to[33]

$$\langle T_e \rangle = \frac{3}{m_e} \int_0^\infty p^2 J(p) \mathrm{d}p. \tag{4.21}$$

The total energy of the system is given by the virial theorem for Coulomb interactions to

$$E = -\langle T \rangle, \tag{4.22}$$

[27] Issolah, A. et al. (1991). *Phys. Rev. B* **44**, 11029.
[28] Huotari, S. et al. (2001). *J. Phys. Chem. Solids* **62**, 2205.
[29] Sternemann, C. et al. (2000). *Phys. Rev. B* **62**, R7687; Huotari, S. et al. (2001). *J. Phys. Chem. Solids* **62**, 2205.
[30] For an overview see Huotari, S. et al. (2001). *J. Phys. Chem. Solids* **62**, 2205; Cooper, M.J. et al. (2004). *X-Ray Compton Scattering*. Oxford University Press; Huotari, S. et al. (2009). *J. Synch. Rad.* **16**, 672.
[31] Fajardo, P. et al. (1998). *Nucl. Instr. Meth. Phys. Res. B* **134**, 337; Kakutani, Y. and Sakai, N. (2004). *J. Phys. Chem. Solids* **65**, 2071.
[32] Epstein, I.R. (1973). *Phys. Rev. A* **8**, 160.
[33] Cooper, M.J. et al. (2004). *X-Ray Compton Scattering*. Oxford University Press.

with the expectation value of the total kinetic energy $\langle T \rangle = \langle T_e \rangle + \langle T_n \rangle$ and the kinetic energy term $\langle T_n \rangle$ including rotational, vibrational and translational motion of the nuclei. By neglecting the contribution of the nuclei and taking into account that Compton measurements are usually performed at isobaric conditions, the adequate measure of energy is the configurational enthalpy which can be estimated to[34]

$$H^{\text{config}} \approx -\langle T_e \rangle. \tag{4.23}$$

With this enthalpy, thermodynamic properties such as the configurational heat capacity c_p^{config} can be calculated to

$$c_p^{\text{config}} = \left. \frac{\mathrm{d}H^{\text{config}}}{\mathrm{d}T} \right|_p . \tag{4.24}$$

Thus, besides the information on local structure and geometry (see section 4.2.2), Compton scattering can be used to extract thermodynamic properties of the sample. This has been previously demonstrated for water and polycrystalline ices,[35] and in this thesis, it is used for clathrate hydrates where it is especially useful for identifying phase transitions.

4.1.3 Computational methods

There is no general connection between the features in experimental XRS or Compton scattering spectra and the structural properties of a sample material. The most comprehensive interpretation of the experimental spectra is usually obtained by comparisons to calculations that simulate the experimental result. To model the electronic excitations, the Schrödinger equation for a system consisting of N interacting electrons has to be solved, which means $3N$ spatial variables and a spin for each electron. As this is practically not possible for complex systems, approximations are needed, such as, e.g. Hartree-Fock (HF) theory or density functional theory (DFT). In the case of Compton scattering, HF calculations were used to estimate the core electron's contribution to the overall Compton spectrum[36] and were shown to be a good approximation as long as the impulse approximation is valid.[37] In this work DFT is used for calculations which is a good compromise between accuracy and computational cost compared to Hatree-Fock and other more sophisticated methods.

In the framework of DFT, all properties of a system are understood as functionals of the electron density. In the static case, i.e. if no time-dependent external fields are present, the

[34] Nygård, K. et al. (2007*a*). *Phys. Rev. Lett.* **99**, 197401.
[35] ibid.
[36] Biggs, F. et al. (1975). *Atom. Data Nucl. Data* **16**, 201.
[37] Cooper, M.J. et al. (2004). *X-Ray Compton Scattering*. Oxford University Press.

Hamiltonian of the system can be written as[38]

$$H = -\frac{\hbar^2}{2m_e}\sum_i \nabla_i^2 + \sum_i V_{\text{ext}}(\vec{r}_i) + \frac{1}{2}\sum_{i\neq j}\frac{e^2}{|\vec{r}_i - \vec{r}_j|}. \tag{4.25}$$

Here, the Coulomb repulsion is separated in the third term, while the external potential is given in the second term. DFT is formulated as an exact theory and it bases on two theorems published by Hohenberg and Kohn:[39]

- The external potential $V_{\text{ext}}(\vec{r})$ is determined, except for a constant, by the electron density $\rho_e(\vec{r})$. The total energy is then a functional of $\rho_e(\vec{r})$: $E_{\text{tot}} = E_{\text{tot}}[\rho_e(\vec{r})]$.
- The ground state energy E^0_{tot} is the global minimum of this functional and the density $\rho_e(\vec{r})$ that minimizes the functional is the exact ground state density $\rho_0(\vec{r})$: $E^0_{\text{tot}} = E[\rho_0(\vec{r})] \leq E[\rho_e(\vec{r})]$.

Hence, the ground state density $\rho_0(\vec{r})$ can be estimated by applying a variational principle to find the minimum energy via

$$E_{\text{tot}}[\rho_e(\vec{r})] = F[\rho_e(\vec{r})] + \int V_{\text{ext}}(\vec{r})\rho_e(\vec{r})\mathrm{d}\vec{r}. \tag{4.26}$$

The universal functional $F[\rho_e(\vec{r})]$ is the same for all systems and includes all internal energies of the interacting electron system and is thus independent from $V_{\text{ext}}(\vec{r})$. A solution of Eq. 4.26 for the ground state is given by the Kohn-Sham ansatz[40] by using an auxiliary system of independent, i.e. non-interacting particles $\phi_i(\vec{r})$ which has the same electron density as the system of interest and an effective local potential $V_{\text{eff}}(\vec{r})$. If this potential is fully known, the auxiliary system will yield the same density as an exact solution of the Schrödinger equation. Eq. 4.26 then becomes

$$E_{KS} = T_{KS}[\rho_e(\vec{r})] + \int V_{\text{eff}}(\vec{r})\rho_e(\vec{r})\mathrm{d}\vec{r}, \tag{4.27}$$

with the kinetic energy T_{KS} expressed by

$$T_{KS}[\rho_e(\vec{r})] = \sum_i^{N_0}\frac{\hbar^2}{2m_e}|\nabla\phi_i(\vec{r})|^2, \tag{4.28}$$

with the number of occupied states N_0 and ϕ_i the so-called Kohn-Sham orbitals. The density

[38] Martin, R.M. (2004). *Electronic Structure*. Cambridge University Press.
[39] Hohenberg, P. and Kohn, W. (1964). *Phys. Rev.* **136**, B864.
[40] Kohn, W. and Sham, L.J. (1965). *Phys. Rev.* **140**, A1133.

of the auxiliary system is given by[41]

$$\rho_e(\vec{r}) = \sum_i^{N_0} |\phi(\vec{r})|^2. \tag{4.29}$$

The so-called Kohn-Sham equations are obtained by performing the variational procedure to Eq. 4.27:

$$\left(-\frac{\hbar^2}{2m_e}\nabla^2 + V_{\text{eff}}(\vec{r}) \right) \phi_i(\vec{r}) = \epsilon_i \phi_i(\vec{r}), \tag{4.30}$$

with eigenvalues ϵ_i. The effective potential can be written as a sum of the external potential, a Hartree potential considering the Coulomb interaction, and an exchange-correlation part V_{xc} including all many-particle interactions:[42]

$$V_{\text{eff}}(\vec{r}) = V_{\text{ext}}(\vec{r}) + \int \frac{e^2 \rho_e(\vec{r}')}{|\vec{r} - \vec{r}'|} \mathrm{d}\vec{r}' + V_{\text{xc}}. \tag{4.31}$$

The exchange-correlation potential is calculated from the exchange-correlation energy functional E_{xc} by variation

$$V_{\text{xc}} = \frac{\delta E_{\text{xc}}[\rho_e(\vec{r})]}{\delta \rho_e(\vec{r})}. \tag{4.32}$$

Although the DFT is exact in principle, the exchange-correlation functional is for the majority of applications unknown and has to be approximated. As independent-particle terms are explicitly separated out, $E_{\text{xc}}[\rho_e(\vec{r})]$ can be approximated as a local functional of density. In the framework of this so-called *local density approximation* (LDA), the energy functional can be expressed in the form[43]

$$E_{\text{xc}}[\rho_e(\vec{r})] = \int \rho_e(\vec{r}) \epsilon_{\text{xc}}(\vec{r}) \mathrm{d}\vec{r}, \tag{4.33}$$

where $\epsilon_{\text{xc}}(\vec{r})$ is an energy per electron at a certain point $\vec{r}$ which depends only on the local density at this point. Typically, $\epsilon_{\text{xc}}(\vec{r})$ is approximated in such a way, that the Kohn-Sham equations provide the correct density for a homogeneous electron gas, i.e. the jellium model of interacting electrons with a uniformly distributed positive charge background. Then, the exchange-correlation potential can be approximated by computations, e.g. Monte Carlo methods. Nevertheless, although this approximation is quite simple, the LDA yields good results for numerous applications. Improvements of this methods are given by e.g. the *local spin density approximation* by considering the spin, the *generalized gradient approximation* (GGA),

[41] Jones, R. O. and Gunnarsson, O. (1989). *Rev. Mod. Phys.* **61**, 689.
[42] Martin, R.M. (2004). *Electronic Structure*. Cambridge University Press.
[43] Hohenberg, P. and Kohn, W. (1964). *Phys. Rev.* **136**, B864.

Meta-GGA, and hybrid functionals.[44] The GGA takes also the gradient of the density into account and it often yields improved results compared to the LDA.

Time-independent DFT is only justified for simulating the materials' ground state properties. Time-dependent DFT is the generalization of the theory to time-dependent processes, including electronic excitations.[45] It has important applications for simulating valence electron excitations where dynamic effects play an important role in the electron-hole interactions.[46] Nevertheless, also time-independent DFT can sometimes be used to obtain good results for electronic excitations. Indeed, in the framework of this work, it was used to simulate x-ray Raman scattering spectra.

Calculation of Compton profiles

The relation of the single electron momentum density and the experimental spectrum was shown at high q and E in Eq. 4.13. By applying the density matrix formulation, this can expanded to a many particle system.[47] In terms of the Kohn-Sham orbital, the density matrix is defined by

$$\rho_e(\vec{r},\vec{r}') = 2\sum_i \phi_i(\vec{r})\phi_i^*(\vec{r}'), \tag{4.34}$$

where the factor 2 considers the electron spin. Subsequently, as Compton scattering probes the ground state of the electron-momentum distribution $\rho(\vec{p})$, it can be calculated by a Fourier transformation of the density matrix of the Kohn-Sham states $\phi_i(\vec{r})$ via

$$\rho(\vec{p}) = \frac{1}{(2\pi)^3}\iint \rho_e(\vec{r},\vec{r}')e^{-i\vec{p}\cdot(\vec{r}-\vec{r}')}\mathrm{d}\vec{r}\mathrm{d}\vec{r}'. \tag{4.35}$$

Afterwards, the Compton profile can be calculated following its definition in Eq. 4.13. On this basis, calculations of Compton spectra of water and ice were successfully performed.[48] It is important to note, that mostly only Compton profile differences are of interest. In this way, systematical experimental errors are canceled out. Similarly, though the absolute Compton profiles calculated with DFT can be relatively inaccurate, the errors cancel in the difference profiles. Therefore, the difference profiles can be accurately calculated. The same argumentation holds also for the experimental data, where the systematic errors cancel out so that the difference profile can be measured more accurately than the absolute one.

[44] An overview on these methods and examples are presented in Jones, R. O. and Gunnarsson, O. (1989). *Rev. Mod. Phys.* **61**, 689.
[45] Runge, E. and Gross, E.K.U (1984). *Phys. Rev. Lett.* **52**, 997.
[46] Marques, M.A.L. et al., eds. (2006). *Time-Dependent Density Functional Theory*. Springer.
[47] Hakala, M. et al. (2004). *Phys. Rev. B* 70, 125413.
[48] See, e.g. Hakala, M. et al. (2004). *Phys. Rev. B* 70, 125413; Hakala, M. et al. (2006*a*). *Phys. Rev. B* **73**, 035432; Nygård, K. et al. (2006*a*). *Phys. Rev. E* **74**, 031503

Calculation of XRS spectra

In the XRS process an inner shell electron is excited to an unoccupied final state and hence excited state properties of the system are probed. Despite DFT is a static theory, it has been successfully applied also to core-level spectroscopy. However, electronic excitations in the XRS process induce changes in the electronic structure and numerous approaches have been developed to approximate these time-dependent effects.[49] The calculations shown in this work were done in the framework of the transition potential (TP) approximation.[50] Here, the occupancies of the initial and final one-electron states are set to 0.5. In this framework, the XRS contribution to the scattering cross section in Eq. 4.4 can be directly calculated using the computed Kohn-Sham states in an one-electron treatment as used in section 4.1.2.

4.2 Molecular local structure of liquids probed by NRIXS

In recent years, both XRS and Compton scattering has been used to investigate the local molecular structure of liquids. Here, in particular the hydrogen bond network of water and ice was studied extensively, either experimentally or theoretically. The findings from these studies are discussed in the following sections because they can support the interpretation of the measured XRS and Compton spectra of THF-water mixtures and THF hydrate.

4.2.1 Local structure of water and ice studied by x-ray Raman scattering

The XANES region of an XAS spectrum yields information on the sample's physical and chemical properties such as, e.g. coordination and oxidation state.[51] Hence, it is sensitive to the local structure of the sample and particularly useful for disordered systems where diffraction methods cannot yield a full understanding of the local structure. Especially the hypothetical formation of hydrate precursors in a supercooled water-THF mixture will be accessible by changes in the XANES.

A typical XRS spectrum of water and various ice phases is shown in Fig. 4.4. The spectra are subdivided in three region: a preedge feature at $E \approx 535$ eV energy loss (I), the main edge around $E \approx 537$ eV (II), and the post-edge region at $E \approx 541$ eV (III). The first XRS measurements of liquid water and ice were performed by Bowron et al.[52] They found the preedge feature in the oxygen K-edge spectrum of liquid water, while the ice spectrum shows a characteristic increase of the post-edge signal. However, due to the energy resolution of $\Delta E = 2$ eV, they were not able to discuss the fine-structure of the edges. Here, also an EXAFS analysis

[49] For an overview see Sakko, A. et al. (2007). *Phys. Rev .B* **76**, 205115 and references therein.
[50] Triguero, L. et al. (1998). *Phys. Rev. B* **58**, 8097.
[51] Als-Nielsen, J. and McMorrow, D. (2001). *Elements of Modern X-ray Physics*. John Wiley & Sons, Ltd.
[52] Bowron, D.T. et al. (2000). *Phys. Rev. B* **62**, R9223.

has been performed, yielding an oxygen-oxygen pair distribution function which is similar to neutron diffraction data. More recent EXAFS studies on water and ice demonstrated the applicability of XRS to these sample systems which offers the opportunity to use XRS as a complementary method to x-ray or neutron diffraction.[53] In XANES experiments with liquid water at energy resolutions of $\Delta E = 1$ eV or better, the oxygen K-edge has been shown to be sensitive to a distortion or breaking of hydrogen bonds.[54] Changes in preedge and postedge features of the oxygen K-edge indicate the existence of only two strong H-bonds. This interpretation supports a water model consisting of molecular chains instead of the conventional view of a tetrahedrally coordinated structure. In contrast, Smith et al.[55] concluded that these features originate only from small distortions and that the tetrahedral configurations is still preferred. A high pressure study of liquid water up to $p = 0.6$ GPa suggested that the preedge peak nearly disappears at $p \approx 0.3$ GPa, while it is again observable at higher pressures.[56] This behavior may be interpreted as changes in the average number of hydrogen bonds. In contrast to the conclusions concerning liquid water, an XRS study on supercritical water revealed that approximately 65 % of the water molecules exhibit a tetrahedral coordination.[57] However, the interpretation of the preedge feature in terms of the local structure of water remains under discussion.[58]

A study of the oxygen K-edge near edge structure of H_2O and D_2O at room temperature and 2°C with a very high statistical accuracy showed that deuteration yields similar effects on the structure of water at the molecular level as a lowered temperature.[59] Such an effect had already been suggested by diffraction measurements.[60] Furthermore, the small statistical errors of the experimental data allowed the investigation of a pure temperature effect, i.e. a weakening of the hydrogen bonds at higher temperatures through an elongation of the hydrogen bond length, on the XRS spectrum.

As already mentioned, the oxygen K-edges of water and ice differ in the preedge and main edge features. Moreover, the spectra obtained from various ice phases have different shapes. The first XRS study of different ice phases was performed by Cai and co-workers.[61] By studying liquid water, hexagonal ice Ih, and the ices II, III, IX with a high energy resolution of $\Delta E = 0.3$ eV or better, they found changes in the preedge and main edge region. A trend from liquid water over ice Ih, ice III and ice II to ice IX was observed where the preedge fea-

[53] Bergmann, U. et al. (2007*b*). *J. Chem. Phys.* **127**, 174504.
[54] Bergmann, U. et al. (2002). *Phys. Rev. E* **66**, 092107; Wernet, Ph. et al. (2004). *Science* **304**, 995.
[55] Smith, J.D. et al. (2004). *Science* **306**, 851.
[56] Fukui, H. et al. (2007). *J. Chem. Phys.* **127**, 134502.
[57] Wernet, Ph. et al. (2005). *J. Chem. Phys.* **123**, 154503.
[58] Nilsson, A. et al. (2005). *Science* **308**, 793a; Smith, J.D. et al. (2005). *Science* **308**, 793b; Head-Gordon, T. and Johnson, M.E. (2006). *PNAS* **103**, 7973; Prendergast, D. and Galli, G. (2006). *Phys. Rev. Lett.* **96**, 215502.
[59] Bergmann, U. et al. (2007*a*). *Phys. Rev. B* **76**, 024202.
[60] See e.g. Hart, R.T. et al. (2006). *J. Chem. Phys.* **124**, 134505 and references therein.
[61] Cai, Y.Q. et al. (2005). *Phys. Rev. Lett.* **94**, 025502.

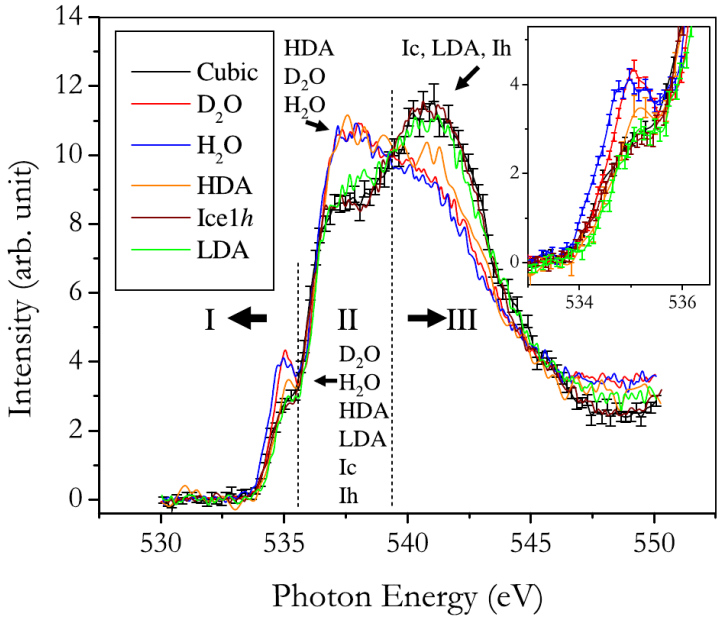

Figure 4.4: XRS spectra of the oxygen K-edge for several modifications of water. The higher ordered phases exhibit a maximum in the post-edge region (III) which is not observable in the disordered phases. Figure from Tse, J.S. et al. (2008). *Phys. Rev. Lett.* **100**, 095502.

ture decreases while the post-edge intensity at $E \approx 541$ eV increases. This was related to the increasing ordering of the protons and the oxygen network in the ice phases. Thus, an occurrence of a preedge feature can also be interpreted as proton disorder. A subsequent study of H_2O, D_2O, ice Ih and Ic, and the two amorphous ice modifications high-density amorphous ice (HDA) and low-density amorphous ice (LDA) revealed that the preedge feature can be found in all water phases. It is diminished in the ice phases compared to the liquid phases, but it is only slightly influenced by the local structure.[62] In contrast, spectral features in the main- and post-edge regions provide information on the degree of the order in the sample's local structure, see Fig. 4.4. In particular, the peak in the post-edge region at $E \approx 541$ eV which is observable in, e.g. ice Ih, is a characteristic of an ordered local environment.[63] This interpretation was recently extended by Pylkkänen et al.[64] In their study of ice Ih, VI, VII, and VIII they found that the preedge feature is observable even with fully coordinated molecules. Furthermore, the spectral changes in the main- and post-edge region can be directly linked to the density of the phases which is itself related to the distance of the second oxygen coordination shell. Here, a large distance as in hexagonal ice Ih means a higher intensity in the post-edge region, whereas a small distance as in ice VI and VII leads to a decreased intensity in the post-edge region together with an increase in the main edge region. Schematic drawings of

[62] Tse, J.S. et al. (2008). *Phys. Rev. Lett.* **100**, 095502.

[63] As LDA is similar to ice Ih and Ic in many properties, in particular the local structure, it shows a spectrum suggesting a higer order than HDA whose structure is heavily distorted and very similar to liquid water, see Tse, J.S. et al. (2008). *Phys. Rev. Lett.* **100**, 095502.

[64] Pylkkänen, T. et al. (2010). *J. Phys. Chem. B* **114**, 3804.

the structures of ice Ih, ice VI and THF hydrate are shown in Fig. 4.5.[65] This finding can also be transferred to the spectra of liquid water, where the distance of the second coordination shell is significant smaller as in ice Ih. A calculation of XRS spectra up to 50 eV behind the edge demonstrated recently the possibility to gain also information of the intermediate range order, i.e. past the first coordination shells, in water systems.[66] This energy interval has been ignored so far in XRS studies and may give fingerprints of the molecular order, e.g. for future studies of high-pressure phases of ice. In conclusion, the sensitivity of the preedge feature to the local structure remains unclear while a shift of spectral weight from the main edge to the post-edge can be linked to a higher order of the oxygen atom. Hence, this thesis focuses mainly on the interpretation of the main and post-edge regions.

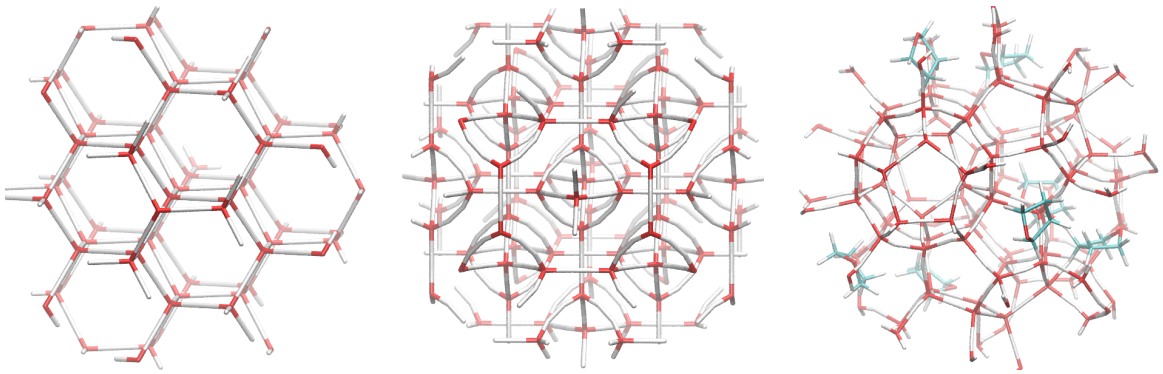

(a) Hexagonal ice Ih. **(b)** Ice VI. **(c)** THF hydrate.

Figure 4.5: Schematic structures of ice Ih, ice VI and THF hydrate. The sites of the oxygen atoms are marked red, bonds are visualized as connections between the atom sites. The different coordination is clearly visible.

Based on these studies on water and ice, measurements of the oxygen K-edge of a liquid mixture of water and THF can be analyzed with respect to the hypothetical formation of hydrate precursors. Such precursor structures would change the local structure of the water molecules significantly so that the shape of the near-edge structure will change from a shape similar to disordered water to a shape which represents a more ordered structure such as, e.g. ice Ih. The spectrum of the fully formed THF hydrate will represent a complete ordered structure. In the framework of the interpretation of Pylkkänen et al., the shape of the oxygen K-edge of THF hydrate should agree in principle with ice Ih because both have similar first coordination shell and second-shell distances of 4.51 Å for ice Ih and 4.33 Å for the hydrate whereas the liquid mixture without precursors should have the same distance as found in water of approximately 3.7 Å.[67] The formation of precursors would result in higher ordered

[65] The structural data for ice VI was taken from Kuhs, W.F. et al. (1984). *J. Chem. Phys.* **81**, 3612.
[66] Fister, T.T. et al. (2009). *Phys. Rev. B* **79**, 174117.
[67] Sloan, E.D. and Koh, C.A. (2008). *Clathrate Hydrates of Natural Gases*. 3rd ed. CRC Press Inc.; Pylkkänen, T. et al. (2010). *J. Phys. Chem. B* **114**, 3804.

structure with a larger second shell distance. Deviations of the spectra can then be related to the existence of the THF molecules.

4.2.2 Intra- and intermolecular structure probed by Compton scattering

Like x-ray Raman scattering, Compton scattering is an indirect probe of the structural properties of the sample material. Therefore, Compton spectra are typically analyzed using comparisons with computational spectra. However, the first Compton scattering studies on water and aqueous solutions were performed in the 1970s[68] although here detailed structural information could not be extracted because of experimental and computational limitations.

The first experiments on ice Ih using a high resolution spectrometer were performed by Isaacs et al,[69] where intensity variations in the directional Compton profile differences were found. This result was interpreted as an evidence for a covalent nature of the hydrogen bond. In the following, theoretical studies argued that these oscillations in the difference profile do not support the purposed covalency.[70] The observed oscillations are originated in the antisymmetrized product of the isolated water monomer and thus are an effect of the transition from monomer to a full crystal. Even the replacement of the oxygen atoms with neon showed the same features in the difference profiles although in this case no hydrogen bonds are present.[71] However, subsequent studies demonstrated the feasibility of Compton scattering to study properties of hydrogen bonds, e.g. in urea.[72] This was later confirmed by Barbiellini at al. who studied theoretically the charage transfer in ice, water monomer and dimer.[73]

A detailed theoretical study by Hakala et al.[74] demonstrated the influences of changes in the local structure of water to the shape of the Compton profile differences. By replacing water with neon they concluded that typical oscillations in the Compton differences profiles are a fingerprint of the hydrogen bond. Furthermore, they analyzed the effect of the bond length and bond angles. Therefore, this work was followed by several studies of water and ice. In a subsequent study, changes originated from intra- and intermolecular effects, e.g. bond angles, bond lengths and O-O distances on the Compton profile of water were analyzed systematically.[75] This was later compared with experiments of liquid water at different temperatures

[68] Whangbo, M.H. et al. (1974). *J. Phys. B: Atom. Molec. Phys.* **7**, L427; Williams, B.G. et al. (1976). *Acta. Cryst.* **A32**, 513; Manninen, S. et al. (1977). *Chem. Phys. Lett.* **46**, 62; Seth, A. and Baerends, E.J. (1977). *Chem. Phys. Lett.* **52**, 248; Paakkari, T. (1978). *Chem. Phys. Lett.* **55**, 160; Seth, A. and Baerends, E. J. (1979). *Chem. Phys. Lett.* **64**, 165.

[69] Isaacs, E.D. et al. (1999). *Phys. Rev. Lett.* **82**, 600; Isaacs, E.D. et al. (2000). *J. Phys. Chem. Solid* **61**, 403.

[70] Ghanty, T.K. et al. (2000). *J. Am. Chem. Soc.* **122**, 1210.

[71] Ragot, S. et al. (2002). *Phys. Rev. B* **65**, 235115.

[72] Shukla, A. et al. (2001). *Phys. Rev. B* **64**, 052101.

[73] Barbiellini, B. and Shukla, A. (2002). *Phys. Rev. B* **66**, 235101.

[74] Hakala, M. et al. (2004). *Phys. Rev. B* **70**, 125413.

[75] Hakala, M. et al. (2006*a*). *Phys. Rev. B* **73**, 035432.

and water and ice Ih.[76] In these works the structural changes (bond lengths and angles) were optimized for the best agreement with the experimental data. Thus, a systematic weakening of the hydrogen bond with increasing temperature and smaller hydrogen bond angles at short bond distances were found for liquid water. The comparison of water and ice yielded in principle similar results. In addition, the number of intact hydrogen bonds per molecule was found to be larger than reported in the XRS study of Wernet et al.[77] Depending on the water model, the mean number of hydrogen bonds per molecule decreases in the temperature region between 298 K and 363 K from 3.9 to 3.1, or from 3.3 to 2.5, respectively. A comparison of the experimental Compton profile difference of water and ice together with calculations basing on different structural models is shown in Fig. 4.6.[78] Here, the *rigid uncorrelated* model represents a liquid water model with rigid intramolecular geometry, while in the *semirigid uncorrelated* model the intramolecular OH bond lengths are correlated with the hydrogen bond length and angles. The *semirigid correlated* model, which provides the best fit to the data, expands the correlation and takes also the correlation between the hydrogen bonds into account. In Compton scattering experiments of water, up to the supercritical phase at $T = 430°\mathrm{C}$ the weakening trend and the decrease of the total number of hydrogen bonds per molecule was confirmed.[79] Moreover, the transition to the supercritical phase was found to be characterized by a sharp increase in the number of water monomers. By studying temperature-induced changes in the Compton profile of hexagonal ice at temperatures between 50 K and 250 K, Nygård et al. extracted the configurational enthalpy and heat capacity for ice.[80] It was demonstrated that Compton scattering has a unique feasibility to access information on structural changes together with thermodynamic properties which offers direct comparisons with MD simulations.

Beside the studies of pure water and ice, the effect of deuteration of water, ion hydration, and hydrogen bonds in non-water systems such as NH_4F and alcohols have also been analyzed recently by Compton scattering.[81] In particular, the study of ion hydration in water showed the sensitivity of Compton scattering on hydration shells which may be similar to the proposed hydrate precursor. Moreover, by comparing Compton spectra of methane hydrate with spectra of ice and methane the effect of the guest-host interaction in hydrates was demonstrated.[82] In summary, based upon the results of Compton scattering experiments on

[76] Hakala, M. et al. (2006*b*). *J. Chem. Phys.* **125**, 084504; Nygård, K. et al. (2006*a*). *Phys. Rev. E* **74**, 031503.
[77] Wernet, Ph. et al. (2004). *Science* **304**, 995.
[78] As usual in Compton scattering experiments, atomic units ($e = \hbar = m_e = 1$) are used for the momentum p_z: 1 a.u.$=\frac{\hbar}{a_\mathrm{B}} \approx 1.99 \cdot 10^{-24} \frac{\mathrm{kg\ m}}{\mathrm{s}}$.
[79] Sit, P.H.-L. et al. (2007). *Phys. Rev. B* **76**, 245413.
[80] Nygård, K. et al. (2007*a*). *Phys. Rev. Lett.* **99**, 197401.
[81] Nygård, K. et al. (2007*b*). *J. Chem. Phys.* **126**, 154508; Nygård, K. et al. (2006*b*). *Phys. Rev. B* **73**, 024208; Barbiellini, B. et al. (2009). *Phys. Rev. B* **79**, 155115; Hakala, M. et al. (2009). *J. Chem. Phys.* **130**, 034506.
[82] Sternemann, C. et al. (2006). *Phys. Rev. B* **73**, 195104. However, the statistical accuracy in this experiment was not sufficient to gain a detailed explanation of the spectra's fine structure. This can be achieved by using

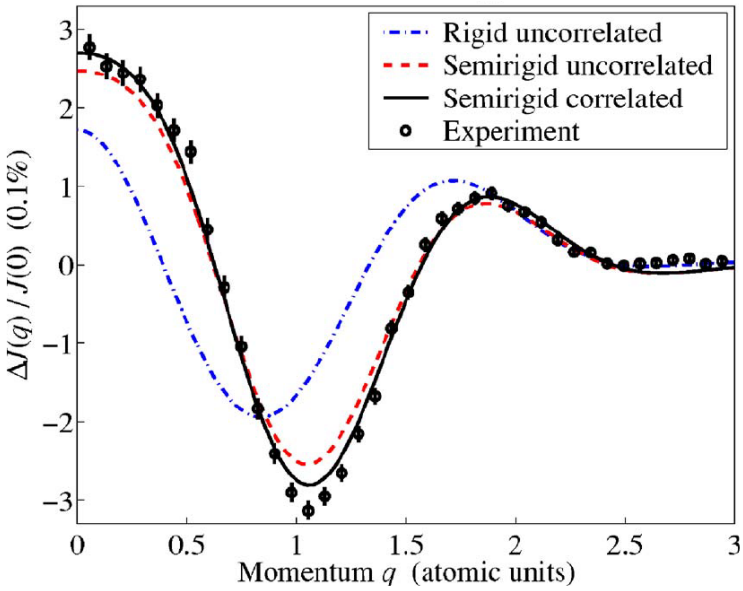

Figure 4.6: Compton profile difference of water ($T = 298$ K) and ice ($T = 223$ K) compared with different theoretical models. Figure from Nygård, K. et al. (2006*a*). *Phys. Rev. E* **74**, 031503.

water and ice and its potential to investigate hydrogen bonds, this method is well capable to study changes in the local environment of a water-THF mixture, e.g. the formation of hydrate precursors, and changes in the formed THF hydrate.

4.3 Sample environments

In order to form THF hydrate in situ during the experiment, special sample environments had to be built which also satisfy the demands of a high temperature stability and have to resist THF as solvent. Therefore, two sample cells were designed, a sample used in the XRS and Compton scattering experiments investigating the hydrate formation process, and a cryostat sample cell to measure Compton profiles of THF hydrate at lower temperatures.

Hydrate formation sample cell

To study the formation of THF hydrate in a mixture of water and THF, a special sample cell had to be built satisfying certain requirements.[83] The cell should allow a large interval of possible scattering angles. Furthermore, the transmission of x-rays with energies of $E \approx 10$ keV should be possible to control the hydrate growth by x-ray diffraction and allow XRS in

solid-state detectors instead of a crystal spectrometer as done in this thesis. Owing to the broad and weak features in the Compton differences of water systems, a high resolution of typically better than $\Delta p_z = 0.2$ a.u. by utilizing a crystal spectrometer is not necessary.

[83] Here only a short overview of the sample cell is presented. More details can be found in Conrad, H. et al. (2009*a*). *Rev. Sci. Instrum.* **80**, 026103 and Conrad, H. (2007). "Tetrahydrofuran clathrate hydrate formation studied by X-ray Raman scattering." Diploma thesis. Technische Universität Dortmund.

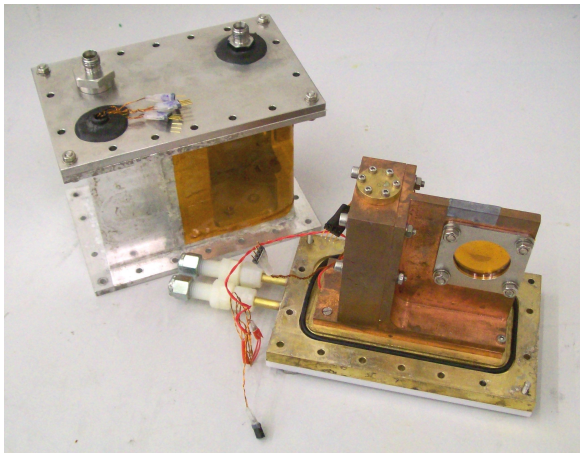

(a) Photograph of the sample cell (right) and the outer chamber (left).

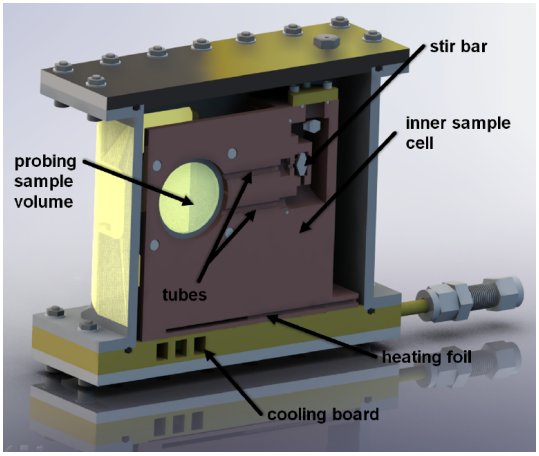

(b) Sectional drawing of the sample cell. Important parts are labeled.

Figure 4.7: Sample cell for THF hydrate formation.

transmission geometry. Therefore, the sample thickness should not exceed a few millimeters. To achieve a high temperature stability in the region of $T = 250$ K - 280 K and to reduce air scattering, the cell environment should be flushable with helium or allow evacuation. Most importantly, due to the very good solvent character of THF for rubber and glues the contact to conventional Viton O-rings or glued surfaces, e.g. for Kapton-foil windows, has to be avoided. Finally, THF hydrate formation has to be initiated by stirring the supercooled water/THF mixture which has to be included in the cell.

To satisfy the requirements, the cell consists of two parts: a large reservoir including the stirring mechanism and a smaller, circular sample volume for x-ray exposure, both made of copper, see Fig. 4.7a. As the liquid is filled in the reservoir and has to flow into the probing volume via tubes of 3 mm diameter, the latter has a thickness of approximately 6 mm with a diameter of 20 mm. A magnetic stir bar is placed into the large reservoir which can be rotated by placing a magnetic stirrer on top of the cell. Kapton and perfluoroethylene propylene (FEP) resist the contact to THF, thus only FEP-coated O rings were used for sealing. The Kapton windows were clamped between the sample volume and an aluminum frame using such O rings. The Kapton windows are 25 µm thick, so that scattering originating from the windows can be neglected.[84] The large diameter of the windows allows changing of the x-ray exposed area during the experiment to avoid radiation damage. The temperature is monitored by two Pt100 elements and controlled using a heating foil and a cooling board made of brass which is flushed by a liquid, e.g., ethanol. Onto the cooling board an outer cell is fixed which can be evacuated or flushed by helium. This procedure provides a high temperature stability of better than 0.01 K and inhibits formation of ice outside the sample cell. With this cell and an adequate chiller set-up, a minimum temperature of approximately 250 K can be achieved.

[84] Bergmann, U. et al. (2007*a*). *Phys. Rev. B* **76**, 024202.

Figure 4.8: Sample cell for cryostat set-up, side view (left) and top view of the opened cell (right). The magnetic stir bar is placed in the chamber above the 6 mm thick measurement section, as seen in the top view.

This is mainly limited by the cooling power of the used chiller. The window design allows measurements in both transmission and backscattering geometry at scattering angles of 0° - 75° and 105° - 180°, respectively. A sectional drawing of the sample cell is shown in Fig. 4.7b.[85]

Cryostat sample cell

To allow measurements of THF hydrate at lower temperatures, a cryostat set-up was utilized in a second experiment. Therefore, a special sample cell which fits to the cryostat cooling head available at beamline ID15B was designed with similar requirements. This is in particular a potential use of FEP-coated O-rings and a magnetic stir bar placed inside the cell. Similar to the other cell, the sample thickness is 6 mm. A photograph of the cell is given in Fig. 4.8. A high temperature stability together with the inhibition of ice formation on the cell is guaranteed by a vacuum chamber around the cryostat cooling head and the sample cell.

4.4 X-ray Raman scattering study on THF hydrate formation

As discussed in section 4.2, the shape of the oxygen K-edge probed by XRS allows to study the local structure and coordination of a sample. In particular, the formation of hydrate precursors will lead to modifications of the oxygen K-edge. Therefore, XRS spectra of the

[85] Picture taken from Conrad, H. (2007). "Tetrahydrofuran clathrate hydrate formation studied by X-ray Raman scattering." Diploma thesis. Technische Universität Dortmund.

liquid water-THF mixture and the hydrate at different temperatures were performed to study the formation of hydrate precursors. The experimental details and the results are discussed in this section.

4.4.1 Experimental set-up at beamline ID16

The XRS measurements were carried out at beamline ID16 at ESRF. A schematic overview of the beamline is given in Fig. 4.9. The x-ray source is an alignment of three U35 undulators. The beam is monochromatized by a pair of Si(660) crystals and a Si(440) channel-cut crystal in order to achieve a high photon flux of $I \approx 3.5 \cdot 10^{13}$ photons per second at an energy resolution of $\Delta E < 0.2$ eV of the incident beam. The spot size of the incident beam was 50×100 µm. The spectrometer is based on the Rowland circle design.[86] Here, the sample, the analyzer, and the detector are aligned on a circle with a diameter of 1 m. A schematic drawing of the spectrometer at ID16 is shown in Fig. 4.10. To access various scattering angles in one experiment, an array of nine Si(660) analyzer crystals at an analyzer energy of 9.69 keV is used at ID16. Hence, a total energy resolution of $\Delta E = 0.55$ eV was achieved. These analyzer crystals cover five scattering angles of distance $\Delta\theta = 6.5°$ each, where four of them were measured by two analyzers. In this thesis, a backscattering geometry with scattering angles between $\theta_{\text{low}} = 127°$ and $\theta_{\text{high}} = 153°$ was chosen, resulting in wave vector transfers of $q = 9.01 - 9.83$ Å^{-1}. The analyzer crystals reflect the scattered beam to a Maxipix 2D detector consisting of 256×256 pixels. This position sensitivity allows studies of inhomogeneous samples or the discrimination of the signals from the sample and the environments such as complex sample cells. Thus, only the contribution of the scattering volume can be filtered by software masking the region of interest.[87] In order to validate the formation of THF hydrate, a MARCCD133 detector was placed behind the sample cell at a distance of 87 mm allowing x-ray diffraction measurements.

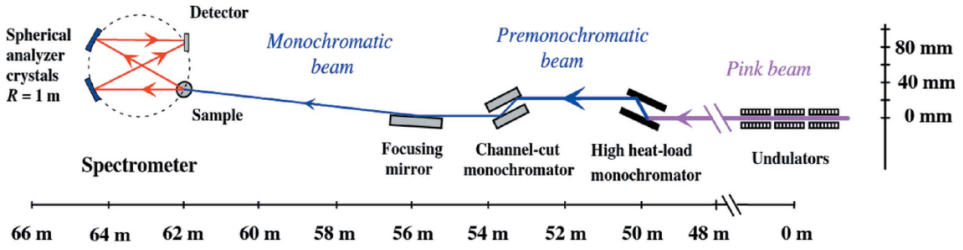

Figure 4.9: Schematic drawing of the set-up at beamline ID16. Figure taken from Verbeni, R. et al. (2009). *J. Synch. Rad.* **16**, 469.

[86] For an overview see e.g. Sternemann, H. (2008). "A non-resonant inelastic x-ray scattering study on silicon oxides and clathrates." Dissertation. Technische Universität Dortmund.
[87] Verbeni, R. et al. (2009). *J. Synch. Rad.* **16**, 469.

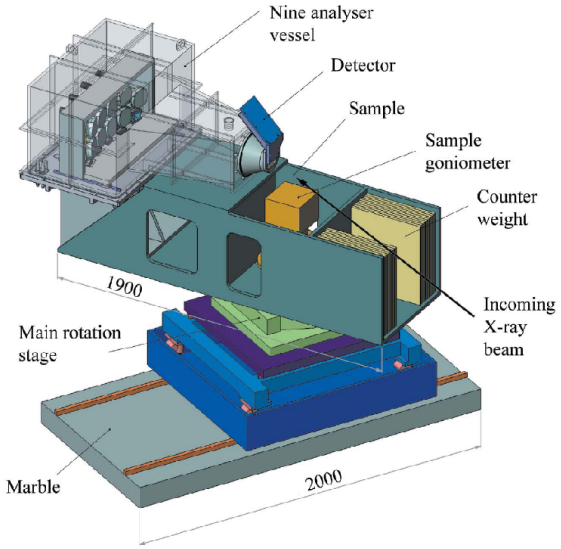

Figure 4.10: Rowland spectrometer at ID16. Figure taken from Verbeni, R. et al. (2009). *J. Synch. Rad.* **16**, 469.

4.4.2 Experimental procedure and raw data analysis

After the sample cell had been filled with a stoichiometric 17:1 mixture of water and THF, it was placed at the sample position as shown in Fig. 4.10. X-ray Raman spectra of the oxygen K-edge were measured for the liquid water-THF mixture at temperatures of $T = 293$ K and $T = 283$ K, and at the supercooled liquid mixture at $T = 275$ K. Subsequently, hydrate formation was initiated by the stirring mechanism. After one to two hours, the hydrate was fully formed and proven by x-ray diffraction. The hydrate was measured at $T = 274$ K and $T = 254$ K. The raw spectra were analyzed as described by Sternemann et al.[88] Since only negligible changes in the spectra for the different momentum transfers were observed, the spectra were averaged over all momentum transfers to obtain a higher statistical accuracy. Finally, all spectra were normalized to the integral from 532 eV to 550 eV.

4.4.3 Results and discussion

The XRS spectra of all measured phases are shown in Fig. 4.11. Following the suggestion by Tse et al.[89], the spectra are subdivided in three regions as indicated in Fig. 4.11: a preedge region (I) dominated by a maximum at an energy loss of about 535 eV, a main edge region (II), and a post-edge region (III) above 539.5 eV energy loss. As demonstrated in section 4.2, the in-

[88] See Sternemann, H. et al. (2008*b*). *J. Synch. Rad.* **15**, 162. A detailed description of the data analysis of the measured spectra is given in Conrad, H. (2007). "Tetrahydrofuran clathrate hydrate formation studied by X-ray Raman scattering." Diploma thesis. Technische Universität Dortmund; Conrad, H. et al. (2009*b*). *Phys. Rev. Lett.* **103**, 218301.

[89] See Fig. 4.4 and Tse, J.S. et al. (2008). *Phys. Rev. Lett.* **100**, 095502.

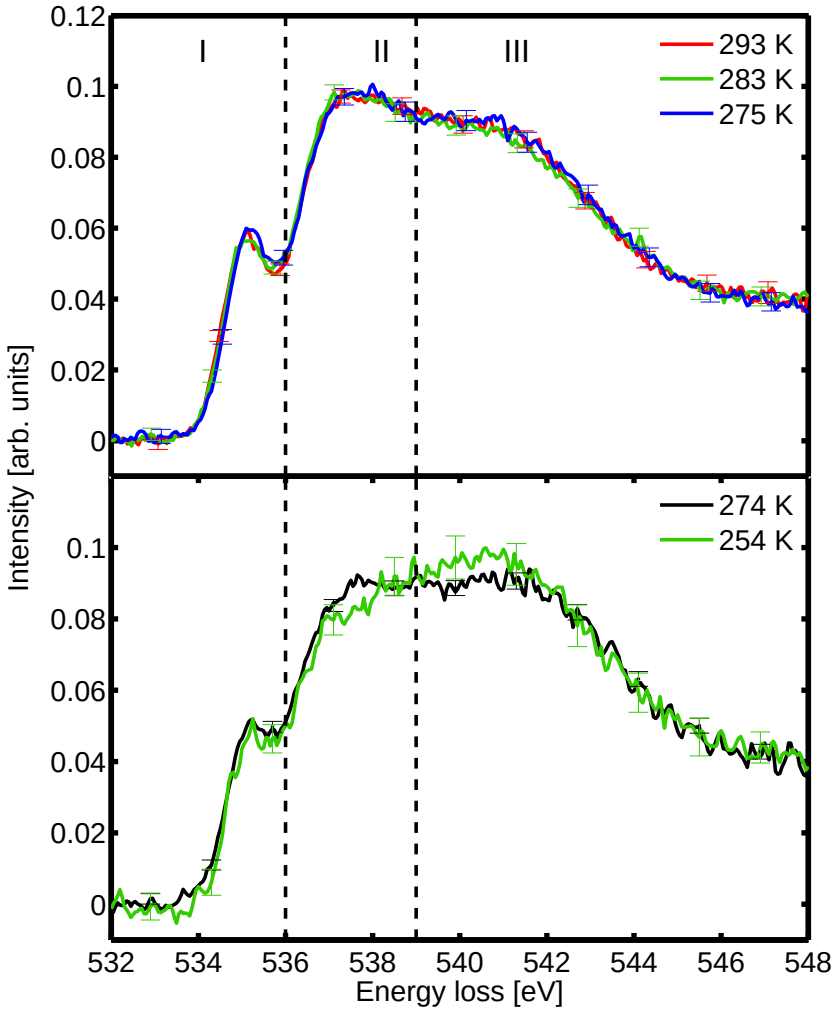

Figure 4.11: All measured XRS spectra of the oxygen K-edge for the liquid mixture (top) and the hydrate (bottom) at different temperature.

fluence of the sample's local structure to the shape of the preedge is debated controversially.[90] In contrast to absorption spectroscopy, not only dipole transitions, but also nondipole transitions contribute to the spectrum at high momentum transfers as used in the present experiment. In water systems, for instance, s-s transitions contribute significantly to the XRS spectrum in the vicinity of the preedge, whereas s-p transitions dominate in the main and postedge regions.[91] Therefore, the discussion regarding the hydrate formation process is focused on regions II and III of the spectrum. Following the interpretations presented in section 4.2, a precursor formation would manifest in a change of local order and coordination and thus in a shift of spectral weight in the XRS spectra at the supercooled temperature of $T = 275$ K. However, all spectra of the liquid mixture do not show any significant difference in contrast

[90] Wernet, Ph. et al. (2004). *Science* **304**, 995; Tse, J.S. et al. (2008). *Phys. Rev. Lett.* **100**, 095502; Cai, Y.Q. et al. (2005). *Phys. Rev. Lett.* **94**, 025502.
[91] See e.g. Pylkkänen, T. et al. (2010). *J. Phys. Chem. B* **114**, 3804.

to the spectra of the solid hydrate, see Fig. 4.11 (top). A comparison with water and ice XRS spectra yields similarities for the liquid water-THF mixture and water, and for hexagonal ice and hydrate at $T = 254$ K, respectively.[92] This can be explained by a similar coordination and local structure for the corresponding phases. An increase of spectral weight in region III was observed for the solid hydrate with decreasing temperature (Fig. 4.11 (bottom)) which may be attributed to a change in the hydrate structure, possibly a rise of structural ordering at lower temperatures.

In order to emphasize the differences in the XRS spectra, the spectra are shown together in Fig. 4.12 (top). The disappearance of the maximum in region II of the hydrate phase and the arising maximum in region III with decreasing temperature support the discussed changes in the local structure. These changes are highlighted by differences of the XRS spectra, see Fig. 4.12 (bottom). First, the discussion is focused on the liquid phase to investigate the formation of hydrate precursors. In general, the difference of the liquid phase at 293 K and 275 K is very weak, in particular in regions II and III no significant difference is observable. For comparison, the averaged difference of water XRS spectra measured at $T = 295$ K and $T = 275$ K is also shown to describe the bare temperature effect on bonding in non-supercooled water.[93] By comparing with non-supercooled water, a potential formation of the highly debated clathrate-like structures in water at supercooled temperatures[94] is suppressed and can be discarded within the experimental resolution. The deviation in the preedge region (I) between water and the measured water-THF mixture can be related to the fact that the water measurements were carried out at a significantly smaller momentum transfer compared to this work. At high momentum transfers, also the s-type local density of empty states (sDOS) contributes significantly to the XRS spectrum in region I.[95] This leads in general to an emphasized preedge feature and thus to more pronounced differences in contrast to measurements at low momentum transfers which probe only the pDOS. Most importantly, in regions II and III the difference between the mixture at room temperature and in the supercooled state is in accordance with the temperature effect of water within the errorbars. Thus, it can be concluded that no signatures of hydrate precursors could be found in the supercooled state in the limits of the experiments and that a hydrate formation model such as the local structuring hypothesis is favored by these measurements.

The comparison of the liquid mixture and the hydrate shows a similar general shape as the spectra of water and hexagonal ice, as mentioned above. Moreover, the hydrate spectra show a significant difference with temperature that may also be attributed to an increase of structural order of the hydrate at $T = 254$ K compared to $T = 274$ K. This finding can be linked to the

[92] Bergmann, U. et al. (2007*a*). *Phys. Rev. B* **76**, 024202; Tse, J.S. et al. (2008). *Phys. Rev. Lett.* **100**, 095502.
[93] Data from Bergmann, U. et al. (2007*a*). *Phys. Rev. B* **76**, 024202.
[94] Yokohama, H. et al. (2008). *Chem. Phys. Lett.* **463**, 99.
[95] Pylkkänen, T. et al. (2010). *J. Phys. Chem. B* **114**, 3804.

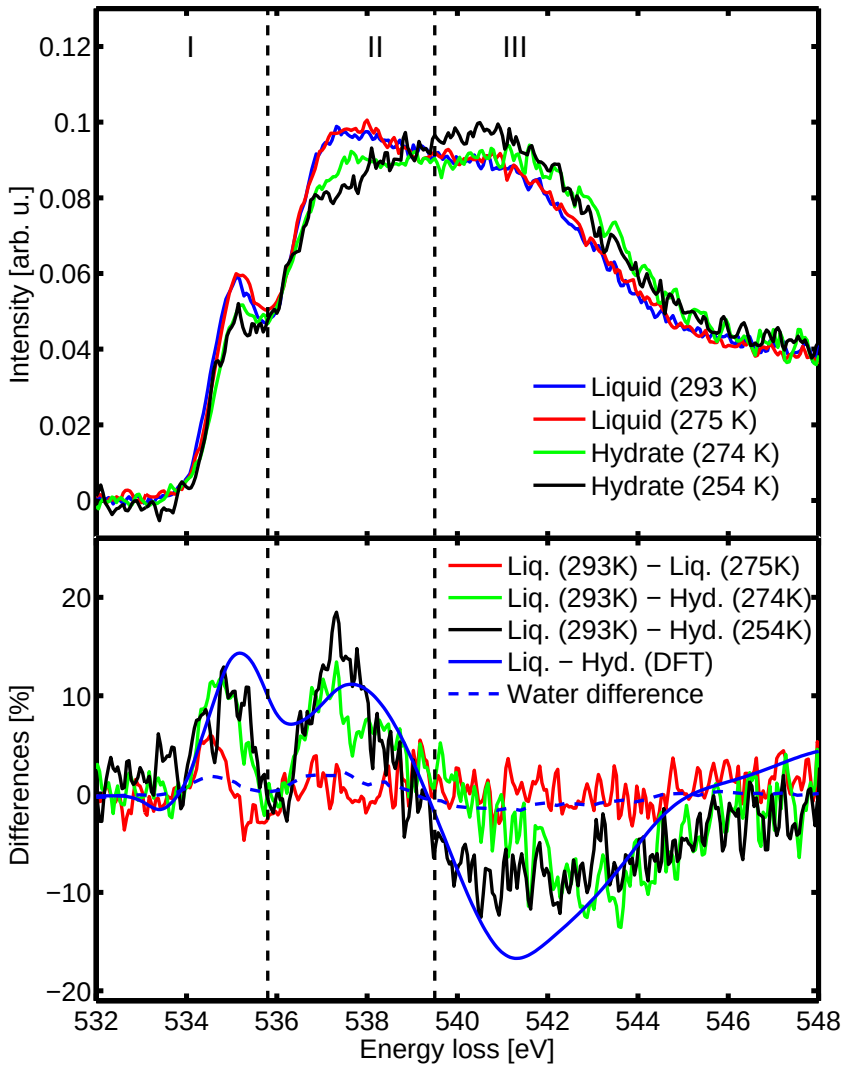

Figure 4.12: XRS spectra (top) and spectra differences (bottom) of the liquid mixture and the hydrate.

abnormal behavior of thermodynamic properties of THF hydrate.[96] The nonlinear behavior of thermodynamic properties from THF hydrate above $T \approx 265$ K may be connected to a change of hydrate structure, evidenced by the XRS spectra. Here, a possible reason for such a structural change above $T \approx 265$ K may be the formation of hydrogen bonds between enclosed THF molecules and water molecules from the cage which leads to distorted cages or even defects in the hydrate lattice as shown in section 2.1.3.

In order to compare the experimentally obtained XRS spectra with structure models, DFT calculations have been performed of a liquid mixture and THF hydrate, see Fig. 4.12 (bottom). Details of the calculations are given in the appendix E. For the liquid phase, snapshots

[96] See section 2.1.4 and Leaist, D.G. et al. (1982). *J. Phys. Chem.* **86**, 4175; Waite, W.F. et al. (2005). *Proceedings of the Fifth International Conference on Gas Hydrates*, 1725.

from MD simulations were used as input for the structure,[97] while for the hydrate phase the structural model was obtained from neutron diffraction measurements.[98] It has to be emphasized that the MD simulations do not show any kind of hydrate precursors in the supercooled phase. In general, a good overall agreement of experiment and theory is achieved, in particular, for the hydrate at $T = 254$ K compared to the difference of liquid and hydrate at $T = 274$ K near the dissociation temperature. This leads to the conclusion that the hydrate at $T = 254$ K is fully formed, whereas at $T = 274$ K the structure is somehow disturbed, probably due to the supposed formation of hydrogen bonds discussed above. Such a change in the hydrogen bond network can be studied in more detail by x-ray Compton scattering, as presented in the next section.

4.5 Compton scattering on THF hydrate

Compton scattering was shown to be very sensitive to changes in a hydrogen bond network, see section 4.2.2. Therefore, Compton scattering experiments of the liquid mixture and the hydrate at different temperatures may extend the findings of the XRS experiment significantly. In particular, changes in the short range order such as intramolecular distances can be investigated in detail by Compton scattering. Moreover, the extraction of configurational energies from the Compton profiles enables a direct relation of structural rearrangements and thermodynamic properties of THF hydrate which may shed light on the thermodynamic anomalies of THF hydrate. Therefore, two Compton scattering experiments were performed in the framework of this thesis. The first is dedicated to study the hydrate formation process by measuring Compton profiles of the liquid water-THF mixture and THF hydrate at temperatures between 253 K and 299 K. In the second experiment Compton profiles of THF hydrate were measured for temperatures between 93 K and 253 K to study structural rearrangements of the hydrate and to extract thermodynamic properties. Both experiments are discussed in this section.

4.5.1 Experimental set-up at beamline ID15B

The Compton scattering experiments were performed at beamline ID15B at ESRF.[99] A photograph and schematic overview of the set-up is given in Fig. 4.13a. Here, a cylindrically bent Si(511) Laue crystal is used as monochromator yielding an incident energy of $E = 86.95$ keV. The monochromator is placed approximately 16 m in front of the monochromator of

[97] Paschek, D. (2008). *private communication*. For details see appendix D.
[98] Jones, C.Y. et al. (2003). *J. Phys. Chem. B* **107**, 6026.
[99] Details of this beamline can be found in Suortti, P. et al. (1999). *J. Synch. Rad.* **6**, 69; Hiraoka, N. et al. (2005). *J. Synch. Rad.* **12**, 670.

ID15A and deflects the beam to the experimental hutch ID15B. Before the beam hits the sample it passes monitoring detectors (ionization chamber A and Si PIN diode D) and a triangular wedge B. This wedge is moved in the beam to absorb a certain amount of intensity in order to gain a constant beam flux on the sample. In prior experiments the decreasing beam intensity due to the decrease of electrons in the storage ring was problematic as the detector only works sufficiently with constant count rates. In particular, for weak effects on the order of 0.1% of the maximum of the Compton profile as observed in water systems, a constant count rate is necessary to neglect systematic errors due to shifting count rates in the detectors. The position of the wedge is controlled every second via the count rate of the monitoring diode D behind the wedge. In this way the beam intensity on the sample deviates only approximately 0.1 % during a scan of several hours allowing highly accurate measurements of Compton profiles. The slit system C defines the beam size to 0.1×0.3 mm^2(v × h). The scattered intensity is measured using a 13-element Ge solid state detector in backscattering geometry at a scattering angle of $\theta = 160°$. Here 13 detectors are arranged in three vertical rows on an area of 58×30 (v×h) mm^2. The scattering events are distributed by the energy of the scattered photons by multi channel analyzers (MCA) into 4096 channels. The energy calibration of these channels is done by measuring the fluorescence of certain substances, in this case tungsten was used since the energy of its Kα and Kβ emissions is near the Compton peak. Thus, the energy difference between two MCA channels was approximately 25 eV. A statistical accuracy of 0.03% or better can be achieved by summing up the signals of all detectors. With the 13-element detector an energy resolution of $\Delta E \gtrsim 400$ eV, which corresponds to a momentum space resolution of $\Delta p_z \simeq 0.6$ a.u. at the Compton peak, is achieved. This is still fully sufficient for the analyzed sample systems, because the Compton profile differences exhibit only broad features, see section 4.2.2. In front of the 13-element detector a slit system is installed to avoid the detection of radiation which was not scattered by the sample. A MAR345 image plate behind the sample was used to prove the formation of THF hydrate by x-ray diffraction.

The Compton profiles of THF hydrate at temperatures below 253 K were measured with a slightly modified set-up in a second experimental run at ID15B. The small sample cell adapted for the cryostat available at beamline ID15B was used. The cell was placed in a vacuum chamber. As only Compton profiles of the solid hydrate were measured in this experiment, conventional O-rings were used for sealing, in order to achieve a better vacuum stability. Previous stability tests demonstrated that after hydrate was formed the O-rings were not affected by THF. In this experiment, a larger beam size of 0.35×0.25 mm^2(v × h) was utilized at an energy of $E = 86.89$ keV with the same momentum space resolution of $\Delta p_z \simeq 0.6$ a.u. at the Compton peak.

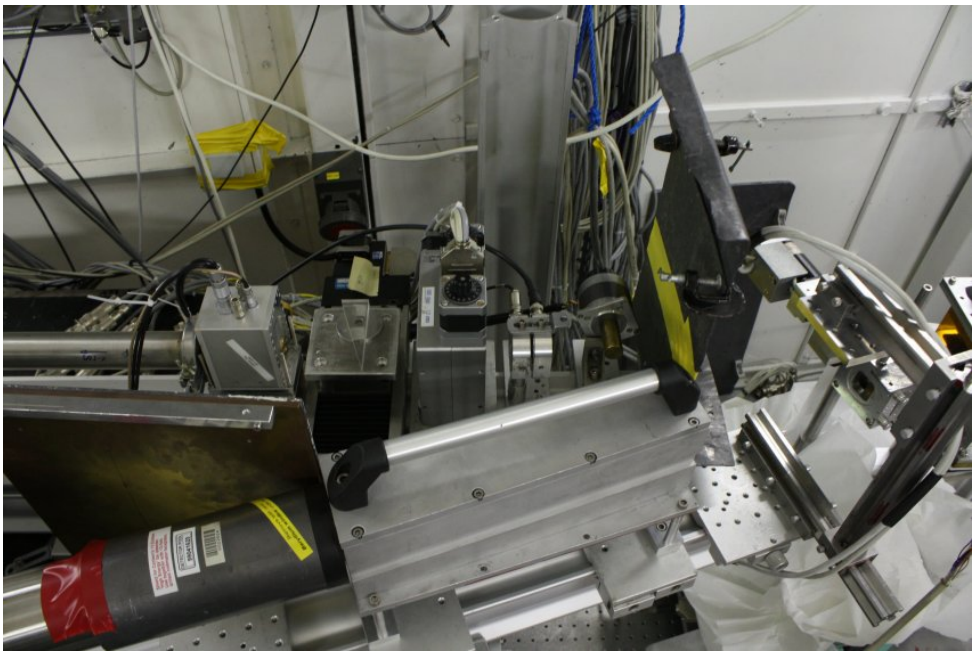

(a) Photograph of the setup for Compton scattering experiments at ID15B.

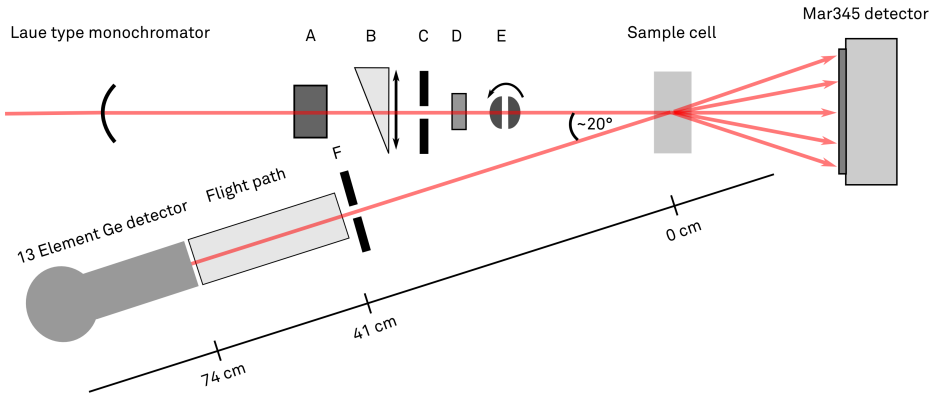

(b) Schematic drawing showing the components of the Compton scattering setup (top view). The distance between the photon source and the monochromator is approximately 42 m, between monochromator and sample cell 9 m, and between sample cell and MAR345 detector 0.7 m. Some components are indicated with letters: ionization chamber A, plexiglas wedge B, slits C and F, monitoring detector D, and shutter E.

Figure 4.13: Experimental setup for Compton scattering experiments at beamline ID15B.

4.5.2 Experimental procedure

For the first experiment, a stoichiometric 17:1 mixture of water and THF was filled into the cell. The sample temperature was set to $T = 299$ K. The chosen beam size guaranteed a count rate per detector of approximately 10000 counts per second. In order to prove the consistency of the data, spectra were saved every 10 minutes. Altogether, spectra were taken for at least seven hours per temperature, yielding a overall count rate of $3.5 \cdot 10^6$ at the maximum of Compton peak at $p_z = 0$ a.u. within a 0.03 a.u. momentum bin per detector. Summing over all detectors, a statistical accuracy of better than 0.03% at $p_z = 0$ a.u. was obtained. After the measurements at 299 K had been finished, measurements at $T = 287$ K and the supercooled temperature of $T = 275$ K were performed for the liquid mixture. Then the liquid was disturbed by a magnetic stirrer which initiated the formation of THF hydrate. This was proven by x-ray diffraction using the MAR image plate detector, see appendix C. Spectra of the hydrate were measured at $T = 275$ K, $T = 265$ K and at the lowest achievable temperature of $T = 253$ K with the chiller set-up using ethanol as coolant.

In order to enable a qualitative analysis of possible hydrate precursor formation, also measurements of a diluted 200:1 mixture of water and THF were performed. For such a low THF concentration, a hydrate crystal cannot form.[100] Thus, these sample can be used as a reference, which is similar to water and ice. However, precursor-like structures may be observable below the hydrate formation temperature of 277.4 K, but less than in the stoichiometric 17:1 mixture. Here, measurements of a liquid mixture were performed at $T = 299$ K and $T = 275$ K, while spectra of the frozen sample were measured at $T = 271$ K and $T = 254$ K.

In the second experiment, the formation of THF hydrate was initiated immediately after the sample cell was filled with the stoichiometric 17:1 mixture. The formation was again validated by x-ray diffraction. Owing to an upgrade of the 13-element detector, each detector was now able to work with a count rate of 60000 counts per second. At these count rates the detector is used in a non-linear region which is possible as long as the count rates do not change during the experiment. Thus, a larger beam size could be used in comparison to the first experiment. Again, spectra were saved every ten minutes. However, a significant lower measurement time of less than five hours was sufficient to achieve an adequate statistical accuracy. A summed count rate of $8.5 \cdot 10^6$ at $p_z = 0$ a.u. within a 0.03 a.u. momentum bin was achieved per detector, yielding a total statistical accuracy of 0.01% at $p_z = 0$ a.u. The hydrate was measured at six temperatures between 253 K and 93 K. Lower temperatures could not be reached during the experiment.

[100] Ganji, H. et al. (2006). *J. Chem. Eng. Jpn.* **39**, 401.

4.5.3 Data analysis

In order to obtain the Compton profile in a Compton scattering experiment, the measured intensity has to be corrected for several contributions. However, as the sample was not changed during the whole experiment, contributions due to a change in, e.g. the sample thickness, can be neglected. Moreover, since only Compton profile differences are analyzed, contributions from background scattering are averaged out.

In a first step, the single spectra were checked for systematic errors. This is done by calculating differences of two single spectra. By assuming the symmetry of the Compton profile, one of the two spectra is shifted until a symmetric difference is obtained. Such a shift did not exceed 15 eV which is well below the experimental resolution of 400 eV. Besides, changes of the width of the Compton profile also occurred. However, this was limited to single detectors and can thus be connected to malfunctions of the detector. These detectors were not used in the following data analysis. The single spectra were summed up for each detector after shifting. Single spectra which exhibit a large deviation from the summed signal were not added to the total spectrum. This was in particular the case during and after injections of electrons into the storage ring.

The measured Compton spectra have to be corrected for various contributions to access the experimental Compton profile J. In general, the measured intensity I can be written as

$$I = B + C \cdot (J + M), \tag{4.36}$$

with the contributions of background scattering B, e.g. scattering from sample cell windows, and multiple scattering M. The energy dependent correction factor C includes corrections for absorption and the relativistic cross section. Furthermore, in particular at high count rates, the so called dead time correction of the detectors has to be taken into account.

Dead time correction

The dead time τ is the time that a detector is unable to process a second event after the first. Therefore, the experimental count rate is lower than the real count rate because several photons were not detected during the expiration of the dead time. The real count rate I can be calculated from the experimental count rate I' via[101]

$$I = \frac{I'}{1 - \tau I'}, \tag{4.37}$$

with all count rates measured in counts per second. The dead time τ can be estimated by comparing the count rate of the detectors with the incident intensity measured by a monitor

[101] Huotari, S. et al. (2001). *J. Phys. Chem. Solids* **62**, 2205.

detector.[102] To achieve different incident intensities, various beam sizes were used. In the first Compton scattering experiment on THF hydrate formation this correction could be neglected, since lower count rates were achieved compared to the second experiment.

Air absorption

Due to a constant incident energy E_1, only the air absorption of the scattered x-rays with energy E has to be taken into account, yielding the correction factor

$$C_{\text{air}} = e^{-d_{\text{air}} \cdot \mu_{\text{air}}(E)}. \tag{4.38}$$

Here, $d_{\text{air}} = 74$ cm is the distance between sample and detector and $\mu_{\text{air}}(E)$ denotes the absorption coefficient for air at standard conditions of $T = 293$ K and $p = 1$ bar.[103]

Sample absorption

Both the incident and scattered beam have to be taken into account in the case of absorption by the sample. Thus, for calculation of the sample's absorption coefficient, the sum for both energies is used by $\mu_{\text{sam}} = \mu(E_1) + \mu(E)$. The sample was aligned so that its surface normal halves the scattering angle θ. One yields the correction factor

$$C_{\text{sam}} = \frac{1 - e^{-d_{\text{sam}} \mu_{\text{sam}} / \cos(180 - \beta)}}{\mu_{\text{sam}} / \cos(180 - \beta)}, \tag{4.39}$$

with $\beta = \frac{180 - \theta}{2}$ and the sample thickness d_{sam}.

Relativistic cross section

As discussed in section 4.1.2, the experimental spectra have to be corrected for relativistic effects, especially at the high incident energy used in this work. Thus, a expansion of the correction factor $C_{\text{rel}} = 1/X(p_z)$ presented in Eq. 4.19 is utilized.[104]

An overview on all energy dependent corrections is given in Fig. 4.14. The final correction factor is given by the product $C_{\text{all}} = C_{\text{air}} \cdot C_{\text{sam}} \cdot C_{\text{rel}}$ of all single correction factors. Besides these corrections, also the asymmetry of the profiles was analyzed.

[102] Monitor detector D in Fig. 4.13.

[103] Absorption coefficients were calculated using *NIST XCOM*. URL: `http://physics.nist.gov/PhysRefData/Xcom/html/xcom1.html`.

[104] Holm, P. (1988). *Phys. Rev. A* **37**, 3706.

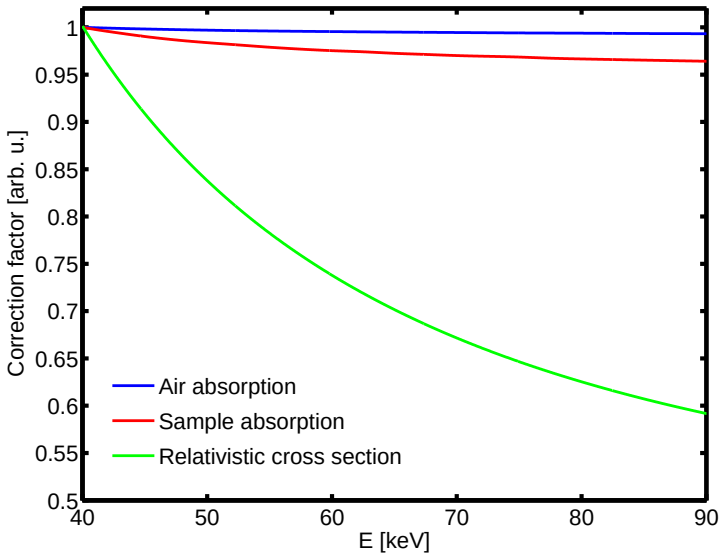

Figure 4.14: Energy dependent correction factors for THF hydrate. The maximum of the Compton peak at $p_z = 0$ a.u. is located at $E \approx 65.2$ keV at the experimental incident energy of $E_1 = 86.95$ keV. The first value of each correction is normalized to one to enable a comparison of the contributions.

Asymmetry

As already discussed in section 4.1.2, several scattering contributions and shortcomings of the impulse approximation result in an asymmetric Compton profile. Usually, these are corrected by a calculation of the amount of multiple scattered photons followed by an asymmetry correction by fitting the data Eq. 4.20 and subsequent subtraction.[105] However, as the liquid's and hydrate's density do not differ at the same THF content,[106] in both cases exactly the same multiple scattering contribution will be estimated. In this thesis only Compton profile differences are analyzed. Following Eq. 4.36, the correction for multiple scattering is averaged out for the Compton differences in this case and can thus be discarded. Furthermore, this is also valid for the contribution of background scattered x-rays.

The asymmetry of the experimental Compton profiles of the first Compton experiment are shown exemplary for three detectors in Figs. 4.15a-c. As usual for Compton scattering experiments, the data is shown as function of p_z, see Eq. 4.14. It can be clearly seen that both the shape and the amplitude of the experimental asymmetry depends on the detector.[107] Furthermore, some of the detectors exhibit a different asymmetry for various samples (Fig.

[105] For an overview see Sternemann, C. (2000). "Final state interaction and temperature effects in Compton scattering from lithium." PhD thesis. Universität Dortmund; Volmer, M. (2006). "Compton Scattering on Complex Materials - an investigation on the electronic structure of alkali-metak doped S-clathrates." PhD thesis. Universität Dortmund.

[106] See Nayak, J.N. et al. (2004). *J. Chem. Eng. Data* **49**, 468 for the density of the liquid. The hydrate's density has exactly the same value, but it was shown that the density in one hydrate crystal may differ up to approximately 4% owing to different cage occupations, see Takeya, S. et al. (2007). *Appl. Phys. Lett.* **90**, 081920.

[107] Honkimäki, V. and Suortti, P. (2007). *J. Synch. Rad.* **14**, 331.

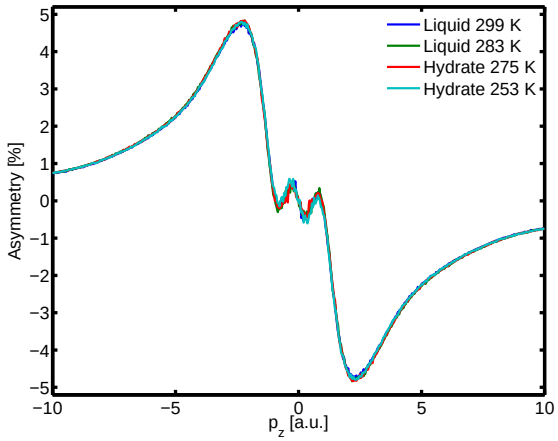

(a) Asymmetry of the Compton profile for detector 5.

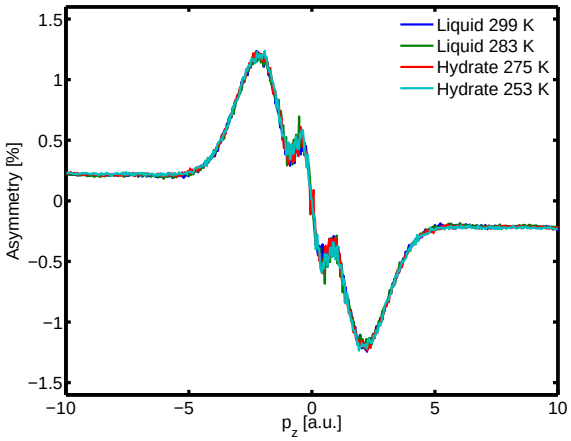

(b) Asymmetry of the Compton profile for detector 9.

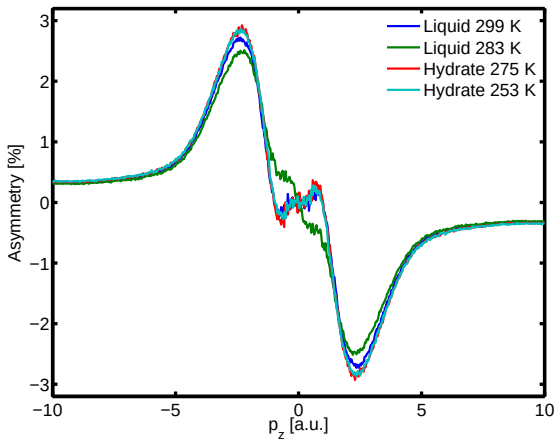

(c) Asymmetry of the Compton profile for detector 4.

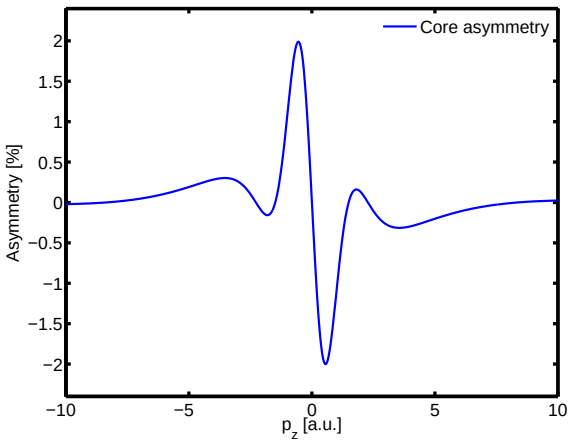

(d) Calculated theoretical core asymmetry for THF hydrate.

Figure 4.15: Experimental and theoretical Compton profile asymmetry for different detectors and sample phases.

4.15c), while other are constant during the experiment (Figs. 4.15a and 4.15b). Therefore, only the latter were used in the data analysis. For comparison, the calculated core asymmetry following the calculation of Holm and Ribberfors[108] based on the theoretical core profiles by Biggs et al.[109] is shown in Fig. 4.15d. It is obvious, that this core asymmetry cannot be used to correct the data although it is at least in the same order of magnitude. However, for the further data analysis the Compton profiles were not corrected for asymmetry because only the profile differences were analyzed. Thus, the differences are not affected by these asymmetries because these systematic errors of the detectors cancel out. In the second Compton experiments on THF hydrate, the asymmetry of the detectors did not change during the experiment. Hence, more detectors could be used compared to the first experiment resulting in significant smaller errorbars.

After taking all corrections into account, the Compton profile differences were calculated for each detector separately and normalized to the number electrons of one THF and 17 water molecules following Eq. 4.15. Finally, the total difference was calculated by averaging over the differences of all detectors.

4.5.4 Formation of THF hydrate

For the Compton profile differences from the first Compton scattering experiment on THF hydrate formation, the measurement of the liquid mixture at $T = 299$ K was chosen as reference. The experimental Compton profile differences are shown in Fig. 4.16. Here, both parts of the difference spectra (positive and negative p_z) were averaged since they only vary slightly inside the errorbars. All differences are shown as percentage value of $J(p_z = 0 \text{ a.u.})$ of the respective reference.

The differences between the liquid mixtures at 299 K and 287 K and 275 K have a maximum at $p_z = 0$ a.u. and a broader minimum at $p_z \approx 1.1$ a.u. By increasing the temperature difference, the amplitudes of the maximum and the minimum are increased, but the shape is not affected. Thus, a similar trend as in the measurements of the temperature effect on water are achieved within the errorbars.[110] As discussed in section 4.2.2, the shape of the Compton profile differences of water was modeled by assuming a weakening of the hydrogen bonds at rising temperatures. The similarity to water is underlined by a direct comparison with the Compton profile difference of the diluted water-THF mixture and water, see Fig. 4.17a.[111] In particular, the measurements of water and the diluted mixture do not show any deviation. The differences between the mixture with the hydrate-stoichiometry (17:1) and water

[108] Holm, P. and Ribberfors, R. (1989). *Phys. Rev. A* **40**, 6251.
[109] Biggs, F. et al. (1975). *Atom. Data Nucl. Data* **16**, 201.
[110] Hakala, M. et al. (2006*b*). *J. Chem. Phys.* **125**, 084504; Nygård, K. et al. (2007*b*). *J. Chem. Phys.* **126**, 154508.
[111] The data for water is taken from Nygård, K. et al. (2007*b*). *J. Chem. Phys.* **126**, 154508. The Compton profiles of the diluted mixtures were normalized to the number electrons assuming a THF amount of 2 %.

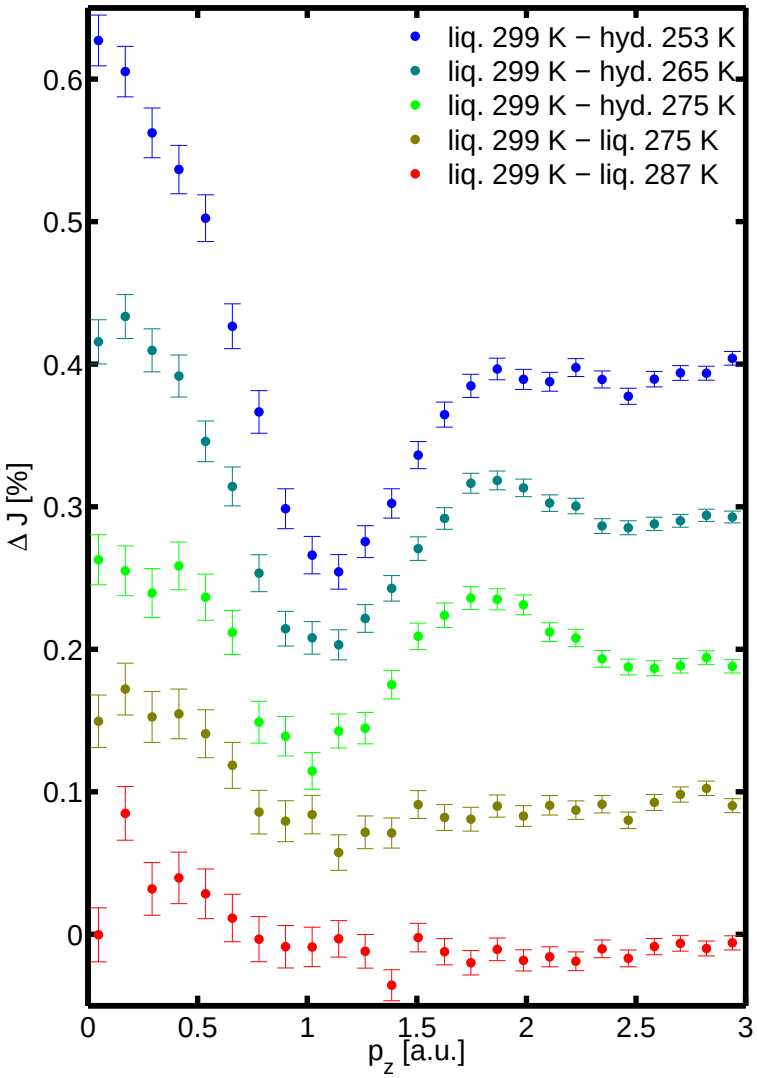

Figure 4.16: Experimental Compton profile differences for the liquid mixture and THF hydrate as function of temperature. Spectra are shifted for clarity, the measurement of the liquid mixture at $T = 299$ K is used as reference.

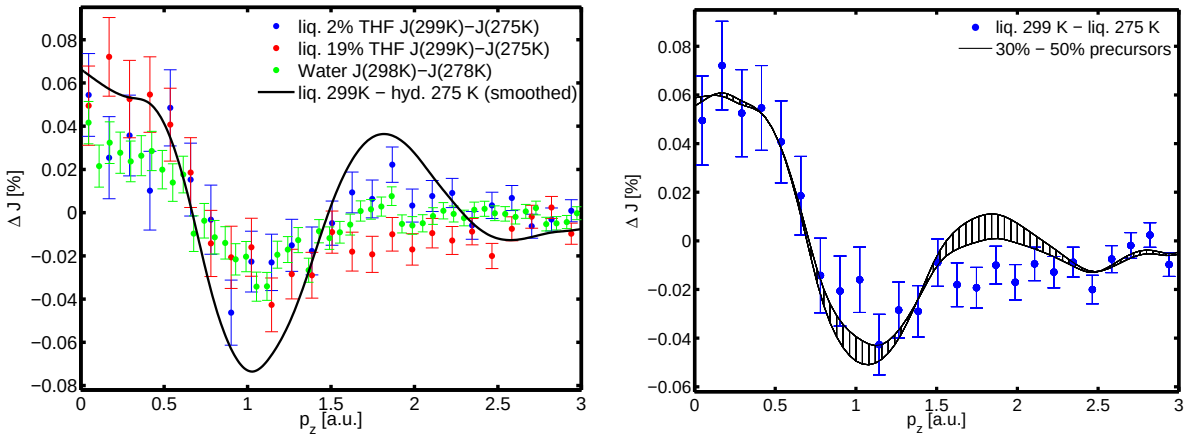

(a) Compton profile differences of the liquid 17:1 mixture (19% THF), the diluted 200:1 mixture (2% THF) and water at different temperatures. The percentage value refers to the mass ration of THF in the liquid mixture. For comparison, also a smoothed liquid-hydrate difference is shown as black line.

(b) Sensitivity to hydrate precursor formation. The black curves are a linear combination of the liquid-liquid and liquid-hydrate differences at 299 K and 275 K with ratios of the liquid-hydrate difference of 30% and 50%, respectively.

Figure 4.17: Compton profile differences of the liquid phases and sensitivity to hydrate precursors.

for $p_z = 0$ - 0.5 a.u. and $p_z = 1.5$ - 2.5 a.u. can be related to the influence of the higher amount of THF molecules compared to the diluted mixture. However, this deviation is too weak to be interpreted as a hint for a structural change, such as the formation of hydrate precursors at the supercooled temperature of $T = 275$ K. Furthermore, because the difference between $T = 299$ K and $T = 275$ follows the same trend as the difference between $T = 299$ K and $T = 287$ K shown in Fig. 4.16, the formation of hydrate precursors can be denied within the limits of the experiments. Moreover, the formation of precursors is suggested to result in Compton profile differences whose shape becomes similar to a liquid-hydrate differences. This is not the case for the difference between $T = 299$ K and $T = 275$, in particular for $p_z = 1.5$ - 2.5 a.u., where both shapes vary strongly. The comparison between liquid-liquid and liquid-hydrate differences is also shown in Fig. 4.17a by the smoothed difference between the liquid mixture at $T = 299$ K and the hydrate at $T = 275$ K.

Besides the similar shape of the liquid-liquid differences, the lack of hydrate precursors can also be demonstrated by an estimation of the sensitivity of Compton scattering to hydrate precursors. By suggesting no precursors in the liquid mixture at $T = 275$ K justified by the similar shape of the difference spectra, the occurrence of hydrate precursors is modeled by a linear combination of the liquid-liquid and liquid-hydrate difference, both for $T = 299$ K and $T = 275$ K, respectively. Since Compton scattering is in particular sensitive to the short range order which should be similar for the hydrate and for the precursors, the liquid-hydrate difference can be assumed to represent a precursor ratio of 100%. In Fig. 4.17b the liquid-liquid difference between 299 K and 275 K is shown together with an estimated precursor

ratio between 30% and 50% (hatched area). Especially for $p_z \approx 1.5$ - 2.5 a.u. the experimental liquid-liquid difference does not fit in the hatched area. The upper limit of the amount of molecules forming hydrate precursors is estimated to 15%. However, as it is proposed that precursors should form with every dissolved THF molecule, it can be assumed that at least 50% of the molecules should form these precursors suggesting a potential break-up of some precursor structures[112] so that their formation can be denied. It has to be noted, that the liquid-hydrate differences at lower temperatures would yield significantly lower values for the precursor ratio, but due to the same temperature interval, the measurement at 275 K has to be favored as reference.

In contrast to the liquid differences, the hydrate differences exhibit a strong dependence to temperature which was not observed for ice in this small temperature interval,[113] but is in line with the XRS experiment. In general, the differences between the hydrate and the liquid mixture resemble the water-ice difference shown in Fig. 4.6. They show the same oscillatory features which are typical for changes in the water hydrogen bond system, i.e. a maximum at $p_z = 0$ a.u., a minimum at $p_z \approx 1$ a.u. and a second maximum at $p_z \approx 1.8$ a.u. However, differing from ice, the amplitude of the minimum is only approximately half of the value found in water-ice. Moreover, the amplitude of the second maximum is generally smaller and decreases with decreasing temperature. These findings can be understood as special features of the hydrate structure and the influences of the guest molecule. To demonstrate the unusual behavior of THF hydrate, a Compton profile difference of the hydrate at $T = 275$ K and $T = 254$ K ($\Delta T = 19$K) is directly compared to the difference of the frozen diluted mixture and ice measured at a larger temperature difference of $\Delta T = 50$ K at temperatures of $T = 100$ K and $T = 150$ K in Fig. 4.18.[114] The difference of the frozen diluted mixture shows only small deviations from 0, however, the oscillatory feature typical for ice is visible. Owing to the larger temperature difference, this feature is more pronounced for ice. On the other hand, the Compton profile difference for THF hydrate exhibits a completely different shape showing a maximum at $p_z = 0$ a.u. and a broad minimum at $p_z \approx 1.4$ a.u. A similar shape was observed for ice in theoretical work by tuning the OH bond length of the water molecule.[115] Thus, the experimental Compton differences of the hydrate measured close to the hydrate's dissociation temperature suggest a contraction of the OH bond length with decreasing temperature.

This was further analyzed by comparing the experimental spectra with DFT calculations on the basis of the same structural models used for the calculations of XRS spectra. Since

[112] Sloan, E.D. and Koh, C.A. (2008). *Clathrate Hydrates of Natural Gases*. 3rd ed. CRC Press Inc.
[113] Hakala, M. et al. (2006*b*). *J. Chem. Phys.* **125**, 084504.
[114] Data for ice taken from Nygård, K. et al. (2007*a*). *Phys. Rev. Lett.* **99**, 197401. Here it was demonstrated that the Compton differences for ice change linearly at least above $T = 100$ K, so only ΔT is important to show the differences in the ice Compton profiles, the difference for, e.g. $T = 250$ K and $T = 200$ K has a similar shape.
[115] Hakala, M. et al. (2006*a*). *Phys. Rev. B* **73**, 035432.

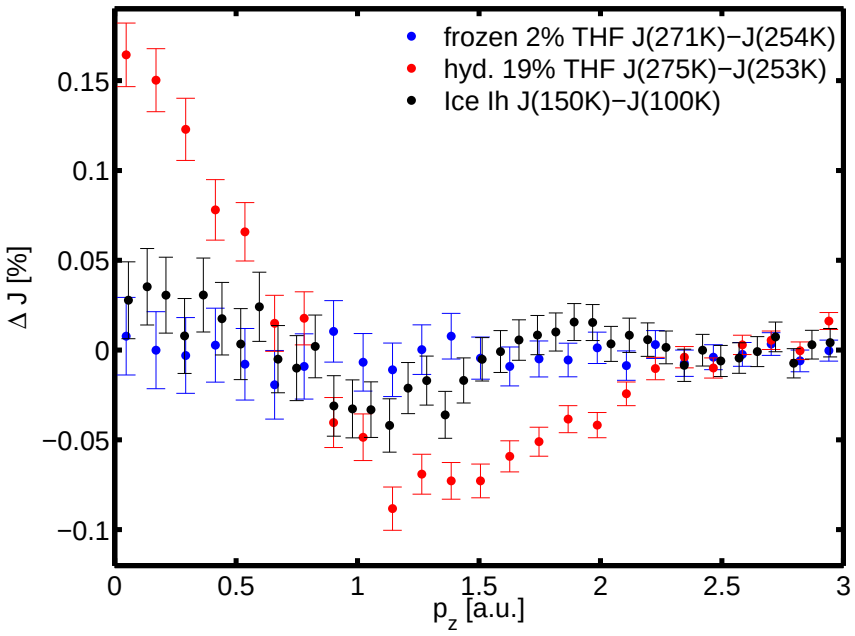

Figure 4.18: Compton profile differences of the hydrate and the frozen diluted mixture compared to differences of ice at different temperatures.

the structural data for the liquid phase do not show significant differences for the simulated temperatures, the amplitudes in the calculated difference profiles for the liquid mixtures were at least one order of magnitude too weak and are hence not discussed in the following. It can be concluded, that the MD simulations fail to describe how the temperature change affects the structure of the liquid, in particular the intra- and intermolecular bond lengths. Computed Compton profile differences of the liquid mixture and the hydrate are shown in Fig. 4.19. The profiles were normalized just like the experimental profiles to the number of electrons of one THF and 17 water molecules. Using the hydrate structure as it was obtained from neutron diffraction, the amplitude of the difference is larger by a factor of four than the experimental difference between the liquid mixture at $T = 299$ K and the hydrate at $T = 253$ K. However, the general shape is well reflected. This means in particular the ratio of the maximum at $p_z = 0$ a.u. and the minimum at $p_z \approx 1$ a.u. and the shape for $p_z > 1.5$ a.u. The water molecules in the original hydrate structure exhibit OH bond lengths between 0.92 and 1.02 Å, yielding a mean value of approximately 0.97 Å. In contrast, the OH bond length of the simulated water-THF mixture was found to be 1.00 Å. These different bond lengths influence the Compton scattering calculations significantly.[116] Nevertheless, the effect is very systematical and therefore the calculations were performed with stretched OH bond lengths in the hydrate structure which are also shown in Fig. 4.19. A stretching of 4.7 % yields a similar amplitude at $p_z = 0$ a.u. as the experimental difference between the liquid at $T = 299$ K and the hydrate at $T = 253$ K, but the maximum-minimum ratio does not fit to

[116] See Hakala, M. et al. (2004). *Phys. Rev. B* **70**, 125413; Hakala, M. et al. (2006*a*). *Phys. Rev. B* **73**, 035432.

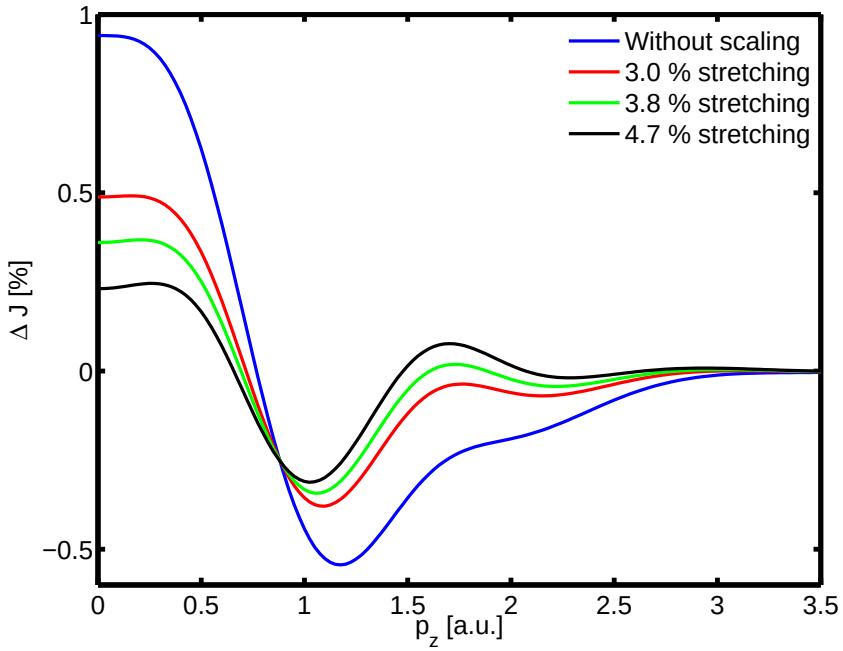

Figure 4.19: Calculated Compton profile differences of a liquid water-THF mixture and THF hydrate for various OH bond lengths in the hydrate structure.

the experiment. More detailed calculations will be needed to fully understand the result.

Nevertheless, the comparison of liquid mixture and hydrate at different temperatures supports the assumption of a change in the OH bond length in THF hydrate with temperature. This is emphasized by comparing directly the hydrate phase profiles, see Fig. 4.20. The difference between $T = 265$ K and $T = 253$ K has the same shape and amplitude as the difference between $T = 275$ K and $T = 265$ K which suggests a similar structural change in both temperature regions. Here, a calculated difference assuming a contraction of the OH bond length of 0.5 % by cooling yields a good agreement to the experimental data. In this calculation the reference structure ($T = 253$ K) was constructed using diffraction based data but where the mean OH bond length was scaled by +3 % in order to obtain 1 Å, similar to the bond length in the liquid structures. Such an effect has not been observed by diffraction experiments so far,[117] but up to now diffraction studies on THF hydrate mainly focused on a temperature range well below the temperatures studied in this thesis.

Since a similar change of the OH bond length has not been observed in water molecules for such small temperature differences without a phase change, it is assumed that processes related to structural changes in the hydrate lead to a change of the mean OH bond length. In particular, a strong guest-host interaction as proposed by the recent MD simulations[118] may lead to both disturbed cages with changed bond lengths and a release of single water molecules

[117] Jones, C.Y. et al. (2003). *J. Phys. Chem. B* **107**, 6026.

[118] See section 2.1.3 and Susilo, R. et al. (2009). *Chem. Phys. Chem.* **10**, 824; Alavi, S. et al. (2009). *J. Chem. Phys.* **130**, 174501.

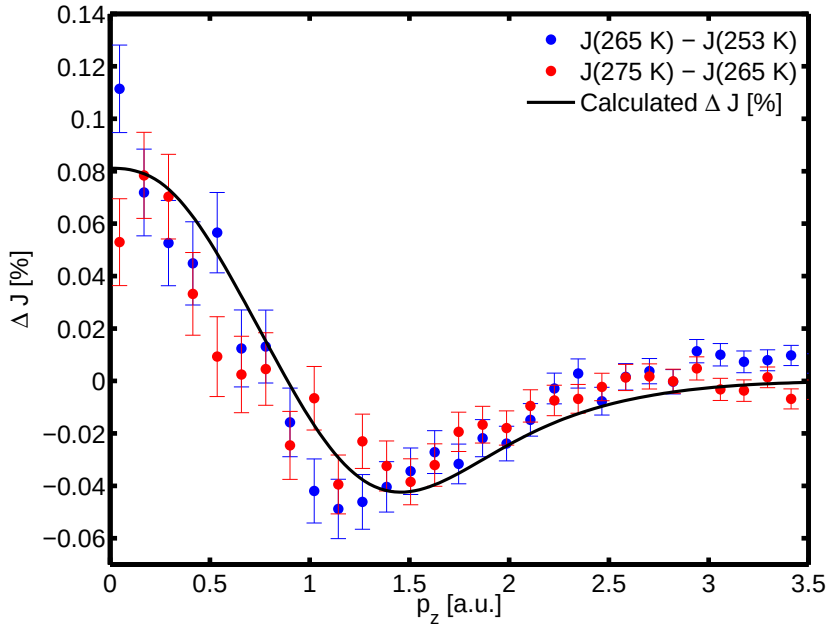

Figure 4.20: Compton profile differences of THF hydrate at different temperatures together with calculated difference ΔJ, assuming contracted OH bond length by 0.5 % at the lower temperature.

from the cage. These molecules may behave similar to liquid water with a different OH bond length compared to the bound molecules in the cage network. Furthermore, the assumption of disturbed or partially broken cages fits very well to the findings of the XRS experiment discussed in section 4.4.3. However, it should be noted, that the observed change of the effective OH bond length of 0.5% per approximately 10 K is huge compared to changes usually observed in a larger temperature region. Here a more detailed XRS experiment probing similar temperature intervals as done in the Compton experiment may provide additional information on the hydrogen bond lengths and the medium-range local order of the sample[119] which can be expected by disturbances of the cage network. Finally, as the observed differences in the hydrate phase may be connected to the anomalies of thermodynamic properties,[120] special attention to these is given in the subsequent section.

4.5.5 Effect of temperature on THF hydrate Compton spectra

Experimental Compton profile differences of THF hydrate at various temperatures measured in the second Compton scattering experiment are shown in Fig. 4.21. The measurement at $T = 253$ K was chosen as reference. For the measurement at $T = 240$ K only four detectors could be used because the Compton profiles measured by the other detectors exhibited an in-

[119] Pylkkänen, T. et al. (2010). *J. Phys. Chem. B* **114**, 3804.
[120] Leaist, D.G. et al. (1982). *J. Phys. Chem.* **86**, 4175; Waite, W.F. et al. (2005). *Proceedings of the Fifth International Conference on Gas Hydrates*, 1725.

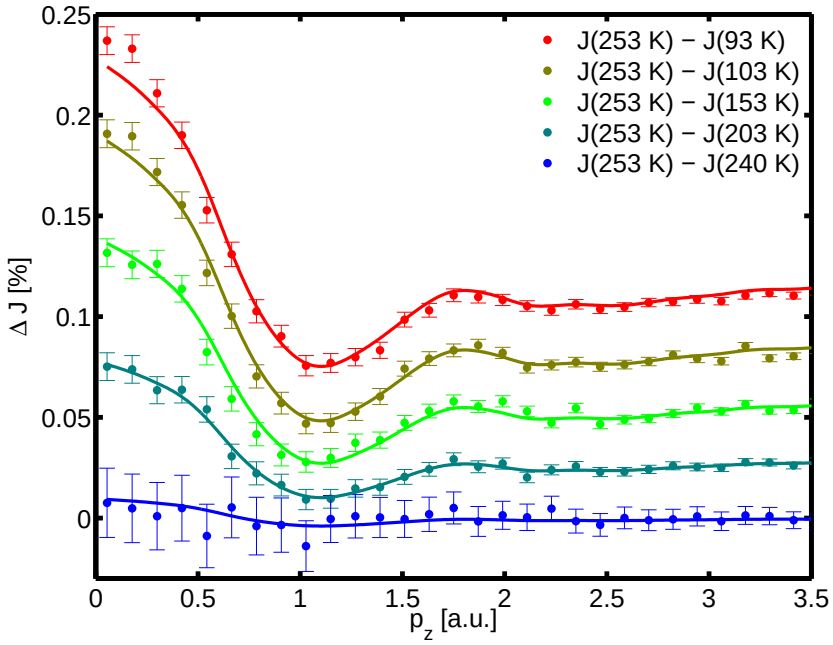

Figure 4.21: Compton profile differences of THF hydrate as function of temperature. Curves are shifted vertically for clarity by 0.03% each. The solid line represents the scaled and smoothed difference of $T = 253$ K and $T = 203$ K.

creased broadness during the measurements. Therefore, the statistics are worse compared to the other temperatures. However, the differences between the measurement at $T = 253$ K and $T = 240$ K deviates only slightly from 0. Hence, it can assumed, that the structural rearrangements observed in the first Compton experiment do not occur below approximately $T = 253$ K. At lower temperatures the difference spectra exhibit a similar shape as for hexagonal ice,[121] but again the minimum at $p_z \approx 1$ a.u. and the maximum at $p_z \approx 1.8$ a.u. are less pronounced. This second maximum grows with decreasing temperatures together with an arising broad and weak minimum at $p_z \approx 2.4$ a.u. The latter was not observed for ice. The solid lines in Fig. 4.21 represent smoothed differences of the measurements at $T = 253$ K and $T = 203$ K which are scaled to fit the other differences. Owing to the good agreement to the data, it can be deduced that the difference spectra change almost linear with temperature. Most importantly, the shape of the differences does not change. A variation of the amplitudes of the first maximum and minimum in the Compton profile differences was shown to be connected to different hydrogen bond lengths,[122] e.g., due to a decreased lattice parameter. Thus, because the amplitudes of the differences for the hydrate are comparable to the amplitudes observed in ice, both samples seem to behave similar in the studied temperature region. In particular, the shape varies from the measurements at temperatures next to the dissociation temperature which can be connected to different structural rearrangements in both temperature regions.

[121] Nygård, K. et al. (2007*a*). *Phys. Rev. Lett.* **99**, 197401.
[122] Hakala, M. et al. (2006*b*). *J. Chem. Phys.* **125**, 084504.

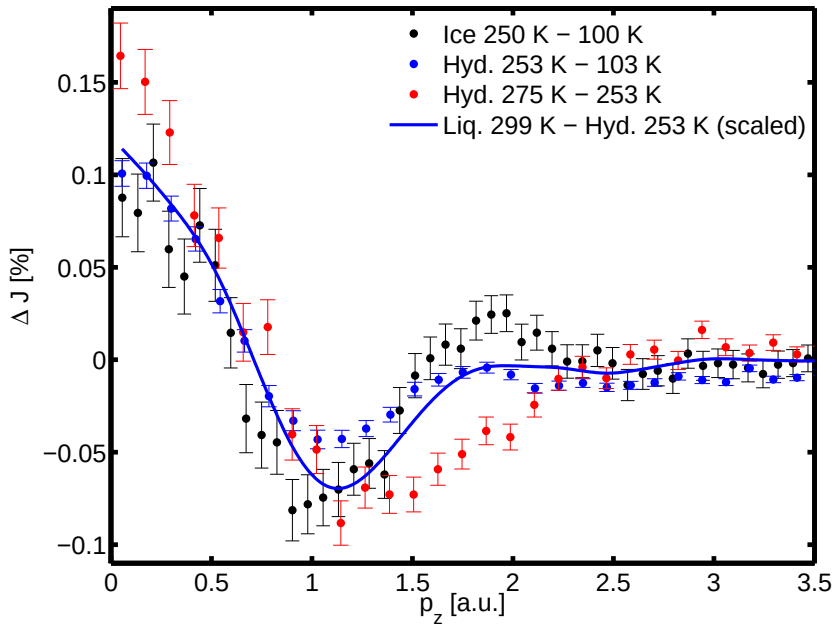

Figure 4.22: Comparison of Compton spectra of THF hydrate at different temperature regions and ice.

The difference between the spectra of the hydrate above and below $T = 253$ K is emphasized by the comparison shown in Fig. 4.22. Especially the shape of the spectra for $p_z \approx 1.5$ - 2.0 a.u. demonstrates the different behavior of the sample in the corresponding temperature regions. The direct comparison to the difference for ice[123] supports similar processes for hydrate and ice by cooling due to a similar shape of the differences. On the other hand the weaker amplitudes give rise to a slightly different behavior of the hydrate which are originated, e.g. by the influence of the THF molecule on the structure. The solid line in Fig. 4.22 represents a scaled difference between the liquid at $T = 299$ K and the hydrate at $T = 253$ K in order to match the amplitude of the hydrate difference. Such a procedure yielded a very good agreement in the case of water and ice suggesting similar changes in the bond geometry of ice upon heating and melting to liquid water.[124] The deviation for THF hydrate indicates that this is not fully valid for THF hydrate. Although the shape of the liquid-hydrate difference is similar to the hydrate-hydrate difference, the minimum at $p_z \approx 1.0$ a.u. does not agree accurately. This is in line with the observations concerning the comparison of THF hydrate and ice.

A comparison of experiment and DFT calculation for THF hydrate is demonstrated exemplary for the difference between $T = 253$ K and $T = 103$ K in Fig. 4.23. To model the thermal expansion of the hydrate in the DFT calculations, the oxygen-oxygen distance of the water network is changed according to the measured thermal expansion of THF hydrate in

[123] The difference data for ice is taken from Nygård, K. et al. (2007*a*). *Phys. Rev. Lett.* **99**, 197401.
[124] Nygård, K. et al. (2007*a*). *Phys. Rev. Lett.* **99**, 197401.

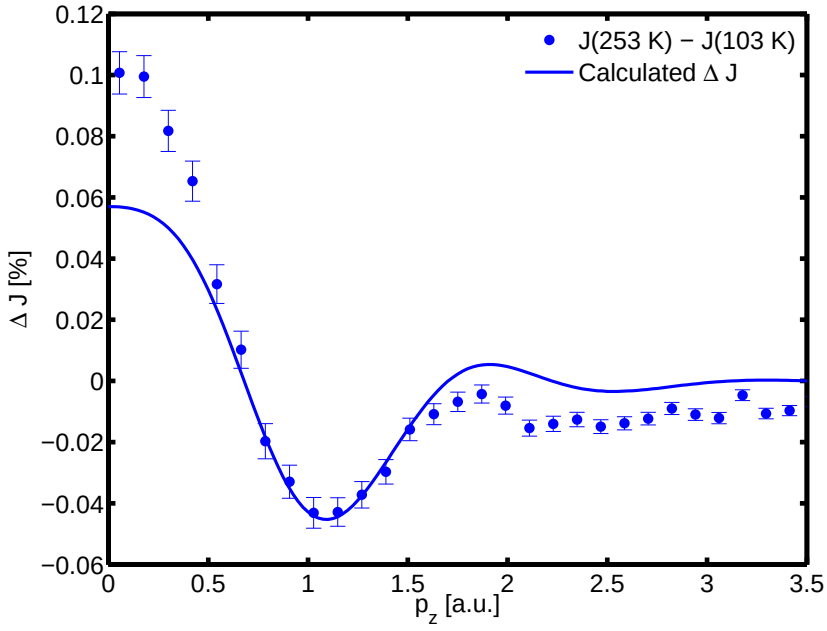

Figure 4.23: Experimental and calculated Compton profile differences of THF hydrate between 253 K and 103 K.

this temperature interval.[125] Although the shape of the profile differences is fairly reproduced by the calculations, the amplitudes cannot be modeled accurately,[126] in particular for $p_z \leq 0.5$ a.u. and $p_z \geq 1.6$ a.u. which can not be explained by an additional change of the OH bond length. Hence, other contributions have to be taken into account, e.g. changes in the shape or different orientations of the THF molecules.[127] However, the linearity of the changes with temperature allows to study thermodynamic properties of the sample, as shown in the following section.

Calculation of thermodynamic properties

As demonstrated in section 4.1.2, it is possible to extract thermodynamic properties from Compton scattering experiments, in particular the configurational enthalpy H^{config} as demonstrated in Eqs. 4.21 and 4.23. However, because it is difficult to account for all systematic experimental errors in Compton scattering experiments, only differences ΔH^{config} are studied in the following. Assuming a constant background for all temperatures, systematic errors can be neglected. The extracted values for ΔH^{config} per molecule are shown in Fig. 4.24 for both experiments. As for $p_z > 4$ a.u. no deviation from 0 occurs in the Compton profile

[125] Jones, C.Y. et al. (2003). *J. Phys. Chem. B* **107**, 6026; Sloan, E.D. and Koh, C.A. (2008). *Clathrate Hydrates of Natural Gases*. 3rd ed. CRC Press Inc.

[126] Similar results were observed in Compton profile calculations of ice, Sakko, A. and Hakala, M. (2009–2010). *private communication*.

[127] Owing to a slight change of the hydrate's density, a correction for multiple scattering may also result in a better agreement of experiment and calculation which has to be modeled accurately.

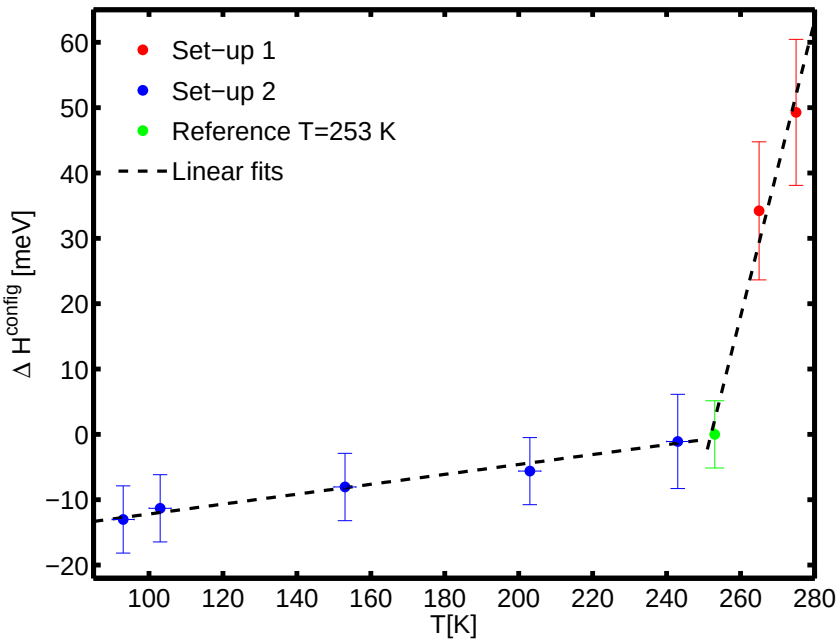

Figure 4.24: Configurational enthalpy as function of temperature. Data obtained from both Compton scattering experiments are presented. Therefore, the measurements at $T = 253$ K were used as reference. The fits provide the value of the configurational heat capacity c_p^{config}.

differences, the integration range was limited to 0 a.u. $\leq p_z \leq 4$ a.u.

Similar to a previous experiment on ice,[128] the linear changes of the Compton profile below $T = 253$ K imply a constant heat capacity $c_p^{\text{config}} = (\mathrm{d}H^{\text{config}}/\mathrm{d}T)_p$ in this temperature region. A linear fit to the data yields a value of $c_p^{\text{config}} = (0.37 \pm 0.11)\ \mathrm{Jg^{-1}K^{-1}}$. This value is slightly smaller than the value for ice of $c_p^{\text{config,ice}} = (0.44 \pm 0.11)\ \mathrm{Jg^{-1}K^{-1}}$,[129] which can be related to the enclosed THF molecules leading to a larger effective weight per molecule and thus to smaller values of c_p. By normalizing the heat capacity to the number of molecules, one yields nearly the same values of $c_p^{\text{config,hyd.}} = (7.8 \pm 2.3)\ \mathrm{J\,mol^{-1}K^{-1}}$ for THF hydrate and $c_p^{\text{config,ice}} = (8.0 \pm 2.0)\ \mathrm{J\,mol^{-1}K^{-1}}$ for hexagonal ice. Similar results were found in calorimetric measurements of both samples for the total experimental heat capacity[130]

$$c_p = c_p^{\text{config}} + c_p^{\text{vib}}. \tag{4.40}$$

The term c_p^{vib} accounts for vibrational, rotational and translational motion of the nuclei. Furthermore, with Eq. 4.40 the contribution of the nuclei c_p^{vib} can be estimated by using calorimetric data published before.[131] The results are presented in Tab. 4.1. Again, the data is

[128] Nygård, K. et al. (2007*a*). *Phys. Rev. Lett.* **99**, 197401.
[129] ibid.
[130] Tombari, E. et al. (2006). *J. Chem. Phys.* **124**, 154507.
[131] The data obtained by Leaist et al. were used, see Leaist, D.G. et al. (1982). *J. Phys. Chem.* **86**, 4175. They

Temperature [K]	c_p [$Jg^{-1}K^{-1}$]	c_p^{vib} [$Jg^{-1}K^{-1}$]
93	0.94	0.57 ± 0.12
103	0.98	0.61 ± 0.12
153	1.21	0.84 ± 0.12
203	1.44	1.07 ± 0.12
240	1.63	1.26 ± 0.13
253	1.67	1.30 ± 0.13

Table 4.1: Heat capacities of THF hydrate at various temperatures. The total heat capacities c_p are extra- and interpolated from Leaist, D.G. et al. (1982). *J. Phys. Chem.* **86**, 4175.

comparable to the results for ice, although it was assumed to be slightly larger than ice.[132] Unfortunately, due to the experimental problems discussed in section 4.5.1, Compton profiles and heat capacities for $T < 90$ K could not be measured. In this temperature region frozen guest dynamics and a nearly constant lattice parameter were observed which may both influence thermodynamic properties.

The comparison of the data for $T \leq 253$ K with the hydrate spectra measured in the first experiments at temperatures above $T = 253$ K underlines the abnormal behavior of the hydrate in this region. Although a linear relation of ΔH^{config} and temperature cannot be postulated because only three temperatures were measured and larger errorbars were obtained due to lower count rates, a linear refinement to the data yielded a large heat capacity of $c_p^{config} = (4 \pm 2)$ $Jg^{-1}K^{-1}$. However, as shown by Waite et al.,[133] who measured a similar anomaly in this temperature region, the total heat capacity is not constant for the studied temperatures. Furthermore, they found a maximum at $T = 276.1$ K of $c_p(276.1\ K) \approx 6.2\ Jg^{-1}K^{-1}$, which leads to a value of $c_p^{vib} = 2.2 \pm 2\ Jg^{-1}K^{-1}$ for the contributions of the nuclei. Since this value is in line with the extracted values for $T \leq 240$ K, a change of the configurational enthalpy dominates at the higher temperatures. Nevertheless, the results obtained in this experiment may only be understood to demonstrate the structural rearrangements of THF hydrate at temperatures close to the dissociation temperature. More measurements at various temperatures and with higher statistical accuracy would yield a more comprehensive picture of the structural changes underlying the observations.

The measurements of the configurational enthalpy allow the comparison of the experi-

measured the heat capacity at temperatures between $T = 120$ K and $T = 260$ K. More recent publications by Waite et al. (Waite, W.F. et al. (2005). *Proceedings of the Fifth International Conference on Gas Hydrates*, 1725) and Tombari et al. (Tombari, E. et al. (2006). *J. Chem. Phys.* **124**, 154507) analyzed only temperatures above $T \approx 245$ K, but yielded in principle similar results as Leaist et al. in this temperature region.

[132] Tombari, E. et al. (2006). *J. Chem. Phys.* **124**, 154507.

[133] Waite, W.F. et al. (2005). *Proceedings of the Fifth International Conference on Gas Hydrates*, 1725.

mental data with MD simulations. For THF hydrate, simulations have been performed for temperatures between 100 K and 273 K where configurational energies were extracted.[134] The energy increases linear with temperature similar to the result of the experiment. Here, a value of $c_p^{\text{config}} = 1.56\ \text{Jg}^{-1}\text{K}^{-1}$ is obtained from the slope of the fitted lines[135] which is even larger than the total heat capacity. However, since data from other simulations are missing, a conclusion of the quality of these MD simulations cannot be given. Furthermore, the anomaly of THF hydrate above $T \approx 253$ K was not observed in this MD simulation study. In contrast, new simulations of a large hydrate cluster including certain distortions such as the hydrogen bond formation between guest and water molecules[136] and at longer state-of-the-art simulation times may give rise to more accurate heat capacities and the anomaly at high temperatures.

4.6 Conclusions

The study of liquid water-THF measurements at supercooled and non-supercooled conditions by both XRS and Compton scattering revealed no significant differences in the experimental spectra. In previous experiments, the feasibility of the used techniques to study the sample's local structure was demonstrated for water and ice and the interpretation of spectral characteristics was shown. Both techniques provide complementary information of the sample. The shape of the oxygen K-edge probed by XRS on the one hand allows to study the local structure and coordination, on the other hand Compton scattering yields detailed information about short range structure of the sample, e.g. intramolecular order or the hydrogen bond network, and thermodynamic properties. In particular, the formation of hydrate precursors would lead to more ordered structure and thus would manifest in changes of the oxygen K-edge and the Compton spectra. However, the measurements of the stoichiometric liquid mixture of water and THF showed no indication for hydrate precursors in the supercooled state. Comparisons to water measurements exhibited that only the bare temperature effect on, e.g. the hydrogen bonds can be found in the liquid water-THF mixture. Moreover, the lack of hydrate precursors in the MD simulations of water-THF mixtures and the good agreement of experiment and DFT calculations strongly supports the absence of hydrate precursors in a supercooled mixture. Thus, the formation of hydrate precursors can be denied. Consequently, these findings on THF hydrate formation are in agreement with the study of CO_2 in chapter 3 and support stochastic hydrate formation models such as the local structuring hypothesis.

Among the findings to the hydrate formation process of THF hydrate, large differences in the XRS and Compton spectra of THF hydrate were observed for temperatures $T > 250$ K.

[134] Alavi, S. et al. (2006). *J. Chem. Phys.* **124**, 014704.
[135] Alavi, S. (2009–2010). *private communication*.
[136] Alavi, S. et al. (2009). *J. Chem. Phys.* **130**, 174501.

Here, the differences of the XRS spectra suggest a higher local order at lower temperatures, whereas the Compton differences indicate a decrease of the water OH bond lengths at lower temperatures. Both processes can be explained by a structural distortion of the water cage network and a release of single water molecules which act similar to the liquid phase. To draw a final conclusion on this issue, more calculations are needed to try various structural arrangements which can then be compared to the experimental data. Nevertheless, the calculation of configurational enthalpies from Compton profiles yielded similar results as calorimetric studies, where a discontinuous rise of thermodynamic properties has been observed for temperatures of at least 10 K below the dissociation temperature of THF hydrate. This again supports the assumption of a structural change such as cage distortions in this temperature region. The obtained heat capacity for temperatures between 93 K and 253 K is comparable to calorimetric studies. The small difference to the heat capacity of hexagonal ice is in agreement with the larger thermal expansivity of the hydrate compared to ice.

5 Summary and outlook

Summary

In this thesis the formation of clathrate hydrates was studied by means of various x-ray scattering techniques. The hydrate formation at water-gas interfaces was studied for CO_2 by x-ray reflectivity and time-resolved x-ray diffraction measurements. To expand the investigation to bulk mixtures of water and hydrate formers, the formation of THF hydrate was probed by x-ray Raman and Compton scattering. Furthermore, for this sample Compton profiles were measured for temperatures down to $T = 93$ K which made the calculation of thermodynamic properties like the configurational heat capacity possible.

X-ray reflectivity measurements of the liquid-gas water-CO_2 interface exhibit the formation of an adsorbed liquid CO_2 layer onto the water surface. Its layer thickness increases with CO_2 gas pressure, and an adsorption isotherm was refined to the data. Moreover, the evolution of the layer roughness as function of its thickness and a constant water roughness for all gas pressures suggest the pure adsorption of CO_2 molecules without the formation of hydrate or hydrate precursors. In contrast to the liquid-gas interface, x-ray diffraction measurements from the liquid-liquid water-CO_2 interface revealed an instantaneous formation of very mobile, small hydrate crystallites. Altogether, the absence of any hydrate precursors at the liquid-gas interface and the stochastically distributed formation of hydrate crystallites at the liquid-liquid interface suggest a stochastic formation model instead of cluster models predicting hydrate precursor structures.

The formation of THF hydrate was studied by x-ray Raman scattering of the oxygen K-edge for a liquid THF-water mixture at supercooled and non-supercooled conditions. The difference of these spectra can be explained by a bare temperature effect on the bond geometry, a formation of hydrate precursors at supercooled temperatures cannot be observed. These findings are confirmed by Compton scattering experiments of the liquid mixture where also no hydrate precursors could be detected. Furthermore, XRS and Compton spectra of THF hydrate change significantly for $T \geq 253$ K. The shift of spectral weight in the XRS spectra towards higher energy suggests a higher order of the hydrate at lower temperatures, while the Compton differences exhibit a shortening of the effective OH bond length of the water molecules. Altogether, this might be interpreted as distortions of the water cages at higher temperatures which may lead to a less ordered structure and changed bond lengths. DFT

calculations based on MD simulation snapshots and hydrate structures obtained from diffraction experiments of both XRS and Compton spectra support the experimental observations of absent precursors and structural changes in the hydrate. Thus, similar to the measurements of CO_2 hydrate, a formation model without hydrate precursors such as the local structuring hypothesis is supported.

In contrast to the differences of XRS and Compton spectra of THF hydrate for $T \geq 254$ K, Compton spectra measured at temperatures between 93 K and 253 K exhibit only small changes. This agrees with similar measurements on hexagonal ice. The extracted configurational heat capacity is constant for $T \leq 254$ K, while it increases strongly at higher temperatures. These findings agree with calorimetric measurements of THF hydrate and may hence be originated in the suggested distortion of the water cages. However, more DFT calculations are necessary to find a final conclusion.

The thesis contributes to the understanding of the structure and physics of clathrate hydrates. In particular, it advances the knowledge of the hydrate formation process at liquid-gas interfaces and mixtures of water and hydrate forming molecules and provides an unprecedented insight into the local structure of hydrates.

Outlook

In the framework of this thesis, CO_2 and THF hydrate were chosen as examples to study the hydrate formation process by x-ray scattering methods. Since the chosen methods are sensitive to the sample's structure on molecular length scales, they are uniquely suited to study the hydrate formation process for various sample systems. Beside CO_2, in particular the study of hydrate formation at interfaces can be expanded to a large number of hydrate forming substances. First measurements of water-xenon interfaces showed a macroscopic hydrate formation and growth already at liquid-gas interfaces. The use of high energy x-ray reflectivity will also allow the study of liquid-liquid interfaces with respect to the formation of gas hydrates. In particular, liquid-liquid interfaces of water and hydrocarbons such as propane or isobutane are well suited for such experiments, because the dissolubility of these substances in water is significantly lower than CO_2 or xenon. Moreover, measurements of liquid-liquid-gas interfaces, e.g. water-cyclohexane-xenon, may reveal the formation of more complex double hydrates. Such systems are presently under investigation in subsequent work.

More detailed x-ray diffraction studies with higher time resolutions can also demonstrate the formation of a more amorphous pre-hydrate phase as suggested in previous experiments. Furthermore, high-resolution diffraction measurements of the liquid structure factor may give rise to a change in local structure during the hydrate formation process.

In order to find accurate structure models of THF hydrate at high temperatures, more DFT calculations have to be performed. Here, several modifications can be tested, such as

different bond lengths, distorted cages and off-center positions or various orientations of the THF molecules inside the cages. To study the freezing of the guest dynamics at lower temperatures, Compton scattering experiments for $T \leq 93$ K have to be performed in subsequent experiments.

Preliminary results of recent XRS experiments of THF hydrate for temperatures between $T = 20$ K and $T = 275$ K agree with the findings of the Compton scattering experiments, in particular the spectral changes at high temperatures. Here the data analysis has to be completed and the experimental spectra have to be compared with DFT calculations which can thus be performed synchronously for Compton and XRS spectra to find structural models for the hydrate.

A Numerical methods for reflectivity data analysis

The analysis of x-ray reflectivity experiments is usually done by numerical methods such as the Parratt algorithm.[1] Starting with the Fresnel formula in Eq. 3.6 the reflectivity of a sample system consisting of N layers is calculated recursively. For the reflected intensity R_{j+1} and the transmitted intensity T_{j+1} at interface $j+1$, the equations

$$\begin{aligned} R_{j+1} &= \frac{1}{t_{j+1,j}}(T_j r_{j+1,j} e^{-i(k_{z,j+1}+k_{z,j})z_j} + R_j e^{-i(k_{z,j+1}+k_{z,j})z_j}), \\ T_{j+1} &= \frac{1}{t_{j+1,j}}(T_j e^{-i(k_{z,j+1}+k_{z,j})z_j} + R_j r_{j+1,j} e^{-i(k_{z,j+1}+k_{z,j})z_j}) \end{aligned} \tag{A.1}$$

are obtained,[2] where $r_{j+1,j}$ is the reflectivity coefficient of interface j and $t_{j+1,j} = 1 + r_{j+1,j}$ is the transmission coefficient, respectively. The starting conditions are $T_1 = 1$ for the top of the layer system (incident beam) and $R_{N+1} = 0$ for the substrate. Thus, the reflectivity can be calculated starting from the substrate's surface. In order to model the roughness of the layers, the transition between two layer is modeled by, e.g., an error function or a hyperbolic shape. The latter is in general used for liquid-gas interfaces resulting in[3]

$$n_j(z) = \frac{n_j + n_{j+1}}{2} - \frac{n_j - n_{j+1}}{2} \tanh\left(\frac{\pi}{2\sqrt{3}} \frac{z - z_j}{\sigma_j}\right) \tag{A.2}$$

for the index of refraction n_j of layer j, with z_j the position of the interface between layers j and $j+1$ and the corresponding roughness σ_j. Rough surfaces can be replaced by an ensemble of smooth surfaces with constant electron densities. These surfaces are weighted with a probability density P_j, yielding the roughness

$$\sigma_j^2 = \int (z - \mu_j)^2 P_j \mathrm{d}z, \tag{A.3}$$

[1] Parratt, L.G. (1954). *Phys. Rev.* **95**, 359.

[2] Als-Nielsen, J. and McMorrow, D. (2001). *Elements of Modern X-ray Physics*. John Wiley & Sons, Ltd; Tolan, M. (1999). *X-ray Scattering from Soft Matter Thin Films*. Springer.

[3] Tolan, M. (1999). *X-ray Scattering from Soft Matter Thin Films*. Springer.

with the mean value

$$\mu_j = \int z P_j(z) \mathrm{d}z. \tag{A.4}$$

For the hyperbolic-shaped profile, one finds

$$P_j(z) = \frac{\pi}{4\sqrt{3}\sigma_j} \cosh^{-2}\left(\frac{\pi}{2\sqrt{3}}\frac{z}{\sigma_j}\right). \tag{A.5}$$

Then, the coefficients in Eq. A.1 are replaced by modified coefficients $\tilde{r}_{j+1,j}, \tilde{t}_{j+1,j}$:

$$\begin{aligned} \tilde{r}_{j+1,j} &= r_{j,j+1}\frac{\sinh(\sqrt{3}\sigma_j(k_{z,j} - k_{z,j+1}))}{\sinh(\sqrt{3}\sigma_j(k_{z,j} + k_{z,j+1}))}, \\ \tilde{t}_{j+1,j} &= t_{j,j+1}\frac{\sinh(\sqrt{3}\sigma_j(k_{z,j} - k_{z,j+1}))}{\sqrt{3}\sigma_j(k_{z,j} - k_{z,j+1})}. \end{aligned} \tag{A.6}$$

However, the iteration in Eq. A.1 together with the modified coefficients can be performed if the layer thickness is larger than its roughness. If this is not the case, the domain for Eq. A.2 is to small so that a constant value for the electron density cannot be achieved. Thus, discontinuities may occur in the density profile. Here, the *effective density model*[4] connects the region of different densities continuously. Within this model, at first a continuous electron density profile is modeled by connecting hyperbolic or error functions $Y_j(z)$. Then, probability functions $W_j(z)$ are defined in order to achieve continuous transitions, via

$$W_j(z) = \begin{cases} (1 + Y_j(z - z_j))/2, & \forall z \leq \chi_j \\ (1 + Y_j(z - z_{j-1}))/2, & \forall z > \chi_j \end{cases}. \tag{A.7}$$

These functions give the probability to find a fraction of layer j at position z. χ_j denotes the vertical position in the sample where the transition from layer $j-1$ to layer j can be found:

$$\chi_j = \frac{\sigma_j z_{j-1} + \sigma_{j-1} z_j}{\sigma_{j-1} + \sigma_j}. \tag{A.8}$$

[4] Tolan, M. (1999). *X-ray Scattering from Soft Matter Thin Films*. Springer.

The dispersion profile $\delta(z)$ of the sample is subsequently calculated to

$$\delta(z) = \frac{\sum_{j=1}^{N+1} \delta_j W_j(z)}{\sum_{j=1}^{N+1} W_j(z)}, \tag{A.9}$$

where δ_j is the dispersion of layer j. Thus, the continuous dispersion profile can cut in several small layers. The electron density profile $\rho(z)$ can be obtained by multiplying $\delta(z)$ with $\frac{2\pi}{\lambda^2 r_e}$ according to the definition of δ in section 3.1.2. Finally, the reflectivity of such a sample system is calculated with the Parratt algorithm.

B Impulse approximation

As a supplement to section 4.1.2, a more sophisticated derivation of Eq. 4.11 is given in this section. For high energy and impulse transfers, i.e. the regime of Compton scattering, Eq. 4.2 can be simplified in the framework of the *impulse approximation*.[1] By using the Fourier representation of the δ-function

$$\delta(E_\mathrm{f} - E_\mathrm{i} - \hbar\omega) = \frac{1}{2\pi\hbar}\int e^{i(\omega+(E_\mathrm{i}-E_\mathrm{f})/\hbar)t}\,\mathrm{d}t \tag{B.1}$$

Eq. 4.4 becomes

$$S(\vec{q},\omega) = \frac{1}{2\pi\hbar}\int e^{-i\omega t}\sum_{\mathrm{i,f}}\langle \mathrm{i}|\sum_j e^{-i\vec{q}\cdot\vec{r}_j}|\mathrm{f}\rangle \times \langle \mathrm{f}|e^{iE_\mathrm{f}t/\hbar}\sum_j{}' e^{i\vec{q}\cdot\vec{r}'_j}e^{-iE_\mathrm{i}t/\hbar}|\mathrm{i}\rangle\,\mathrm{d}t. \tag{B.2}$$

The replacing of the eigenvalues E_i and E_f by the Hamiltonian H of the system, and using the completeness relation for the final states, Eq. B.2 can be rewritten as[2]

$$S(\vec{q},\omega) = \frac{1}{2\pi\hbar}\int e^{-i\omega t}\langle \mathrm{i}|\sum_j e^{-i\vec{q}\cdot\vec{r}_j}e^{iHt/\hbar}\sum_{j'} e^{i\vec{q}\cdot\vec{r}'_j}e^{-iHt/\hbar}|\mathrm{i}\rangle\,\mathrm{d}t. \tag{B.3}$$

The Hamiltonian $H = H_0 + V$ can be separated into a kinematic term H_0 of a free electron and a constant potential V which enables the expansion of the exponential $e^{iHt/\hbar}$:

$$e^{iHt} \approx e^{iH_0t/\hbar}e^{iVt/\hbar}e^{-[H_0,V]t^2/(2\hbar^2)}. \tag{B.4}$$

Here, significant contributions occur only for $t \leq 1/\omega$ which allows the approximation

$$e^{[H_0,V]t^2/(2\hbar^2)} \simeq 1, \tag{B.5}$$

when $\frac{1}{2}\langle[H_0,V]\rangle \approx E_B^2 \ll (\hbar\omega)^2$. This is the main assumption of the impulse approximation which is valid, when the scattering process is fast compared to relaxations of the system.

[1] Eisenberger, P. and Platzman, P.M. (1970). *Phys. Rev. A* **2**, 415; Cooper, M.J. et al. (2004). *X-Ray Compton Scattering*. Oxford University Press; Schülke, W. (2007). *Electron Dynamics by Inelastic X-ray Scattering*. Oxford University Press.

[2] Schülke, W. (2007). *Electron Dynamics by Inelastic X-ray Scattering*. Oxford University Press.

Since V commutates with $\vec{r}$ and by reducing the discussion to a one electron atom,[3] Eq. B.3 simplifies to

$$S(\vec{q},\omega) = \frac{1}{2\pi\hbar}\int e^{-i\omega t}\langle \mathrm{i}|e^{-i\vec{q}\cdot\vec{r}}e^{iH_0 t/\hbar}e^{i\vec{q}\cdot\vec{r}}e^{-iH_0 t/\hbar}|\mathrm{i}\rangle \mathrm{d}t. \tag{B.6}$$

Followed by the insertion of a complete set of eigenfunctions $|\vec{p}_f\rangle = \frac{1}{\sqrt{V_c}}e^{i\vec{p}_f\cdot\vec{r}}$ of H_0 with

$$e^{iH_0 t/\hbar}|\vec{p}_f\rangle = e^{i\varepsilon(\vec{p}_f)t}|\vec{p}_f\rangle \tag{B.7}$$

and

$$\varepsilon(\vec{p}_f) = \frac{\vec{p}_f^{\,2}}{2m_e}, \tag{B.8}$$

Eq. B.6 transforms into

$$S(\vec{q},\omega) = \sum_{\vec{p}_f}|\langle \mathrm{i}|e^{i\vec{q}\cdot\vec{r}}|\vec{p}_f\rangle|^2\delta(\varepsilon(\vec{p}_f)-\varepsilon(\vec{p}_f-\hbar\vec{q})-\hbar\omega) \tag{B.9}$$

after the time integration has been performed. By redefining the momenta $\vec{p} = \vec{p}_f - \hbar\vec{q}$ and changing from a discrete to a continuous system, Eq. B.9 finally yields

$$S(\vec{q},\omega) = \left(\frac{1}{2\pi\hbar}\right)^3\int|\langle \mathrm{i}|\vec{p}\rangle|^2\delta\left(\frac{\hbar^2q^2}{2m_e}+\hbar\vec{p}\cdot\vec{q}/m_e-\hbar\omega\right)\mathrm{d}\vec{q}, \tag{B.10}$$

with $\varepsilon(\vec{p}_f)-\varepsilon(\vec{p}_f-\hbar\vec{q}) = \varepsilon(\vec{p}+\hbar\vec{q})-\varepsilon(\vec{p}) = \hbar^2q^2/(2m_e)+\hbar\vec{p}\cdot\vec{q}/m_e$ according to Eq. B.8 and the definition of $\vec{p}$. The term $\hbar^2q^2/(2m_e)$ is the non-relativistic Compton shift for an electron at rest and $\hbar\vec{p}\cdot\vec{q}/m_e$ is the Doppler shift of an electron with momentum $\vec{p}$ in its initial state.[4]

Altogether, in the framework of the impulse approximation the scattering process is assumed to happen so fast that the excited electron can be considered as a nearly free electron no relaxation processes occur.[5]

[3] In this case the summations over j and j' can be left out, for a detailed analysis see Löwdin, P.-O. (1955). *Phys. Rev.* **97**, 1474.
[4] Schülke, W. (2007). *Electron Dynamics by Inelastic X-ray Scattering*. Oxford University Press.
[5] ibid.

C Diffraction patterns

In this chapter theoretical x-ray diffraction (XRD) patterns for CO_2 and THF hydrate are presented. With these data it was possible to index the Bragg reflections in the diffraction patterns of CO_2 hydrate presented in section 3.4.2. Furthermore, the formation of THF hydrate without occurrence of hexagonal ice was proven by x-ray diffraction. These diffraction patterns are also presented in this section.

In order to compare the experimentally obtained diffraction patterns, theoretical patterns were calculated using the programme POUDRIX.[1] Here, structural data obtained, e.g. from x-ray or neutron scattering, are used to calculate an x-ray powder diffraction pattern for the given structure.

CO_2 hydrate

For CO_2 hydrate, structural data from Klapproth[2] was used to calculate a corresponding XRD pattern. These data were taken at $T = 273$ K and $p = 30$ bar. The resulting pattern is presented in Fig. C.1.

THF hydrate

The calculated XRD pattern of THF hydrate is shown in Fig. C.2. The input data was taken from Jones et al.[3] and were measured at $T = 265$ K.

Experimental XRD patterns have been measured during all experiments in order to verify the formation of pure THF hydrate. In Fig. C.3 XRD patterns measured during the first Compton beamtime are shown. Here, the transition from the liquid mixture to the hydrate is clearly visible in the change from the liquid structure factor for the mixture to the pattern dominated by Bragg reflections. Compared to the calculated pattern in Fig. C.2, the pattern shows less Bragg reflections and different intensities. This is originated in the growth of hydrate crystallites. These do not resemble a powder which is assumed for the calculated pattern. In general, no liquid structure factor is visible in the diffraction pattern of the hydrate at

[1] *Poudrix Powder X-ray and Neutron Pattern Calculation Software*. URL: `http://www.ccp14.ac.uk/ccp/web-mirrors/lmgp-laugier-bochu/`.

[2] Klapproth, A. (2002). "Strukturuntersuchungen an Methan- und Kohlenstoffdioxid-Clathrat-Hydraten." Dissertation. Georg-August-Universität zu Göttingen.

[3] Jones, C.Y. et al. (2003). *J. Phys. Chem. B* **107**, 6026.

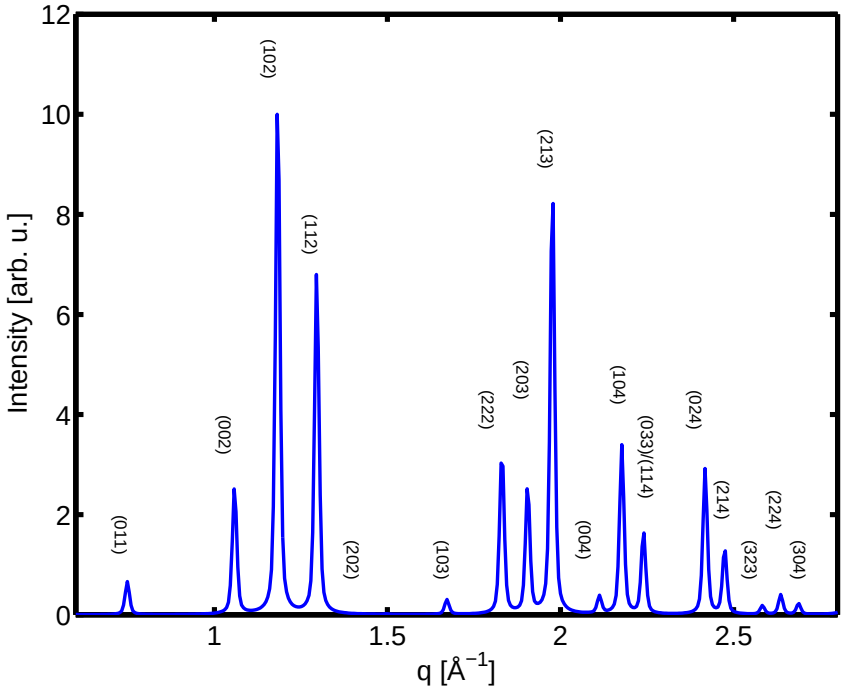

Figure C.1: Calculated diffraction pattern of CO_2 hydrate. The Bragg reflections are indicated.

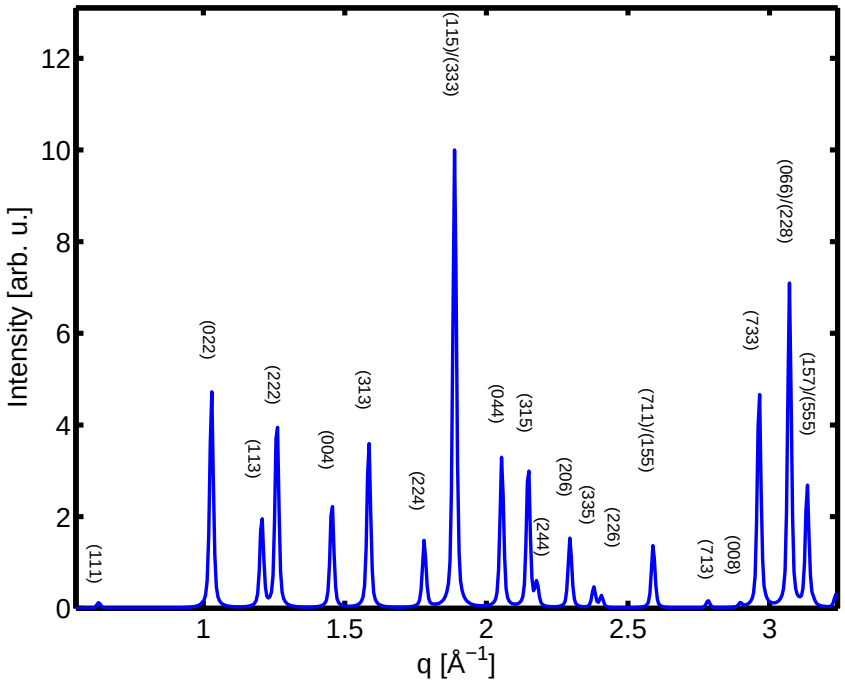

Figure C.2: Calculated diffraction pattern of THF hydrate. The Bragg reflections are indicated.

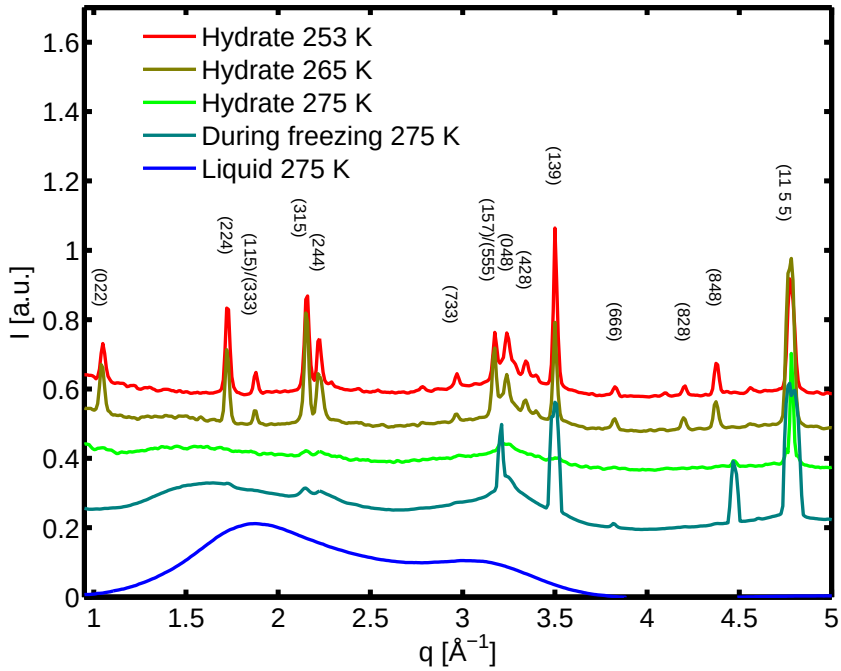

Figure C.3: Experimental diffraction patterns of the liquid mixture and THF hydrate at different temperatures. The patterns were measured during the first Compton experiment, Bragg reflections are indicated.

$T = 275$ K so that formation of ice can be neglected at lower temperatures. The occurrence of more Bragg reflections at lower temperatures suggests a transition from a single crystal structure to a polycrystalline structure which does not change by cooling to $T = 253$ K. However, this does not affect the Compton profiles, because the difference between 275 K and 265 K are similar as the difference between 265 K and 253 K and cannot be explained by an increase of polycrystallinity. Thus, the sample can be assumed to be stable during the experiment.

The XRD patterns measured in the second Compton experiment show only two strong Bragg reflections, see Fig. C.4. Moreover, the increase of the lattice constant at lower temperatures is clearly visible by a shift of the Bragg reflections towards higher q with decreasing temperature.

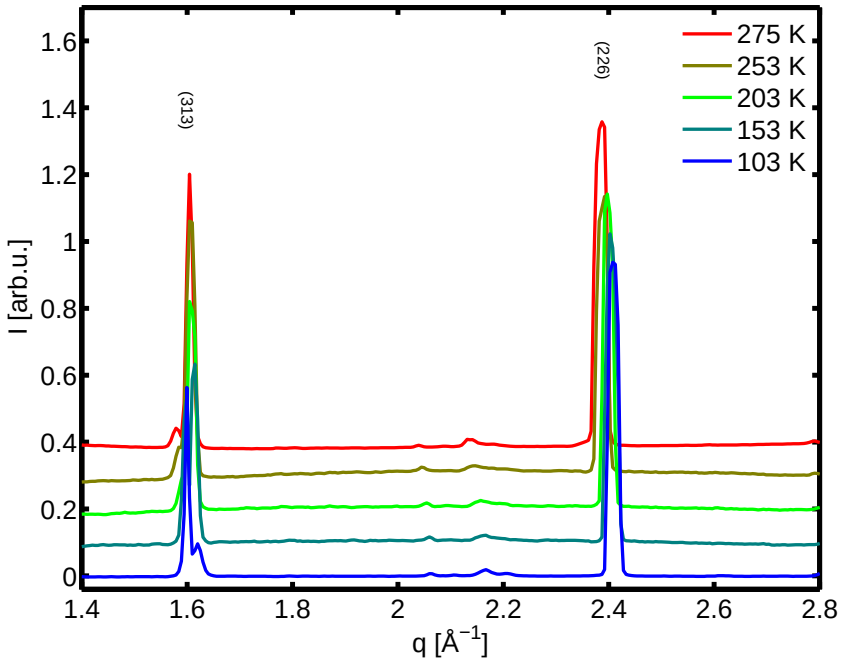

Figure C.4: Experimental diffraction patterns of THF hydrate at different temperatures. The patterns were measured during the second Compton experiment, Bragg reflections are indicated.

D Molecular dynamics simulations

In order to compare the experimental XRS and Compton spectra with calculated spectra, molecular dynamics simulations of the liquid mixture were performed.[1] Here, some details of these simulations are summarized.

The MD simulations were carried out using the GROMACS 3.2 program.[2] The MOSCITO suite of programs[3] was employed to generate start configurations and topology files. For all reported systems, initial equilibration runs of 1 ns length were performed. The simulations were performed of aqueous THF solutions which were composed of 64 THF molecules based on the OPLS-AA forcefield[4] and 1088 SPC/E water molecules.[5] The simulations were carried out at a pressure of $p = 1$ bar at the following five temperatures: 250 K, 260 K, 280 K, 300 K, and 320 K. However, preliminary simulations indicated a strong tendency of the THF molecules to aggregate, and eventually phase separate. This apparently contradicts experimental observations, as the lower critical solution temperature for the THF-water miscibility gap is located at $T = 344$ K,[6] well above the temperatures used in this study. Therefore, the intermolecular nonbonded parameters for the THF-THF and THF-water interactions were modified.[7] These simulations exhibited a significantly reduced aggregation tendency of the THF molecules and showed no formation of large THF-clusters. Instead, the calculated THF-THF pair correlation functions show similar features as the distribution functions reported from neutron scattering experiments.[8] It should be noted that these simulations do not show evidence for the formation of cluster structures which may act as hydrate precursors. These clusters should form instantly in the supercooled mixture[9] and have lifetimes on the order of the simulated time in the MD simulations of $t = 20$ ns.[10]

---

[1] The MD simulations were performed by D. Paschek: Paschek, D. (2008). *private communication*

[2] Lindahl, E. et al. (2001). *J. Mol. Model.* **7**, 306.

[3] Paschek, D. (2005). *MOSCITO4 molecular dynamics simulation package*. http://ganter.chemie.uni-dortmund.de/MOSCITO.

[4] Jorgensen, W.L. et al. (1996). *J. Am. Chem. Soc.* **118**, 11225.

[5] Berendsen, H.J.C. et al. (1987). *J. Phys. Chem.* **91**, 6269.

[6] Oleinikova, A. and Weingärtner, H. (2000). *Chem. Phys. Lett.* **319**, 119.

[7] For details see Stubbs, J.M. et al. (2004). *J. Phys. Chem. B* **108**, 17596; Fischer, J. et al. (2008). *J. Phys. Chem. B* **112**, 2388.

[8] Bowron, D.T. et al. (2006). *J. Phys. Chem. B* **110**, 20235.

[9] Sloan, E.D. (2003). *Nature* **426**, 353.

[10] Guo, G.-J. et al. (2004). *J. Chem. Phys.* **124**, 1542.

E Density functional theory calculations

As XRS and Compton spectra cannot usually be interpreted straightforward, the experimental data has to be compared to calculated spectra in order to yield an accurate interpretation. Therefore, density functional theory (DFT) calculations were performed in order to calculate both XRS and Compton spectra for the THF-water system which will be shortly summarized in this chapter.[1]

The computational XRS spectra and Compton profiles were calculated in the framework of DFT utilizing the STOBE-DEMON code that employs localized Gaussian basis functions.[2] Triple zeta plus valence polarization basis sets were used, except for the excited oxygen site for which iii-iglo and a set of diffuse basis functions were utilized. A gradient corrected exchange correlation functional was used in the calculations.

X-ray Raman scattering

For XRS, the method for performing q-dependent XRS spectrum calculations[3] within this framework was recently presented.[4] The relaxation effects due to the creation of the core hole was modeled by the transition potential (TP) approximation.[5] Furthermore, gradient-corrected exchange-correlation functionals were employed.[6] The calculated liquid phase spectrum is an average over 135 clusters that were extracted from the MD simulations at $T = 260$ K. The differences of the MD simulations at the other temperatures were very weak, so that similar XRS spectra are yielded using a different temperature. Each of these clusters was created by randomly selecting an oxygen atom and then including all THF and water molecules that have at least one atom within a diameter of $d = 5.5$ Å from the central oxygen atom. For the hydrate phase calculation, a model cluster consisting of several small and large cages was created using neutron diffraction data at $T = 265$ K.[7] The THF molecules were fixed into the

[1] All calculation were performed by A. Sakko and M. Hakala: Sakko, A. and Hakala, M. (2009–2010). *private communication*.

[2] Hermann, K. and et al. STOBE-DEMON *version 3.0*. URL: `http://w3.rz-berlin.mpg.de/~hermann/StoBe/index.html`.

[3] Soininen, J.A. et al. (2005). *Phys. Rev. B* **72**, 045136.

[4] Sakko, A. et al. (2007). *Phys. Rev .B* **76**, 205115.

[5] Triguero, L. et al. (1998). *Phys. Rev. B* **58**, 8097; Sakko, A. et al. (2007). *Phys. Rev .B* **76**, 205115.

[6] Perdew, J.P. et al. (1996). *Phys. Rev. Lett.* **77**, 3865; Hammer, B. et al. (1999). *Phys. Rev. B* **59**, 7413.

[7] Jones, C.Y. et al. (2003). *J. Phys. Chem. B* **107**, 6026.

center of the cages so that their thermal motion was neglected. 18 oxygen-centered clusters with the same radii as for the liquid phase were extracted from this structure and their spectra were averaged to obtain the hydrate phase spectrum. Core hole localization was ensured using model core potentials for all nonexcited oxygen sites. To model the lifetime broadening and continuum part of the spectrum, a Lorentzian convolution was used with an energy-transfer dependent half-width of 0.1 eV below 536 eV energy loss and 2.0 eV above 541 eV energy loss. Between 536 and 541 eV energy loss, the half-width increases linearly. Furthermore, a Gaussian convolution with a half-width of the experimental resolution of 0.55 eV was also applied. In order to match the experimental data, the spectra were shifted by 1.2 eV towards lower energies.

Compton scattering

The same structural models obtained from MD simulations and diffraction were used for the Compton scattering calculations as for the XRS. Also the principle is similar, i.e. small model clusters were extracted from the large structures. A set of Compton profiles were calculated for these clusters using DFT with the same exchange correlation correlation functional and similar basis sets.[8] Finally, their average yields the total Compton profile.

Compared to the calculation of XRS spectra, the small model clusters have to be created in a different way for the Compton profile calculations. For the liquid phase, 100 small clusters were centered to randomly chosen points. All the THF and water molecules with at least one atom within the radius of 5 Å from the central point were included in the small clusters. The average Compton profile had to calculated carefully because the number of THF and water molecules in the small cluster only approximately obeys the hydrate stoichiometry condition of 17:1. The final Compton profile is calculated via

$$J(p) = \sum_{i=1}^{N_{\text{tot}}} w_i \cdot J_i(p) \tag{E.1}$$

from the Compton profiles $J_i(p)$ of the clusters. Here, N_{tot} denotes the total number of clusters. The weights w_i are determined from the condition

$$\begin{aligned} \sum_{i=1}^{N_{\text{tot}}} w_i N_i^{\text{THF}} &= 1, \\ \sum_{i=1}^{N_{\text{tot}}} w_i N_i^{\text{H}_2\text{O}} &= 17, \end{aligned} \tag{E.2}$$

[8] Hakala, M. et al. (2004). *Phys. Rev. B* 70, 125413. Since the Compton profile is calculated from the ground state electronic structure, no iglo nor diffuse basis functions are needed.

where N_i^{THF} and $N_i^{\mathrm{H_2O}}$ are the numbers in the ith cluster of THF and water molecules, respectively. This ensures that the correct stoichiometry is obtained in the calculation. For the calculation of the hydrate phase, four different cluster were created: a large cage, a small cage, THF molecule in the cage, and two neighboring cages with five common atoms. Similar to the calculation for the liquid phase, the final Compton profile is a linear combination of these four types with weights chosen in such a way that the hydrate stoichiometry is obeyed.

Bibliography

Alavi, S. (2009–2010). *private communication*.

Alavi, S.; Ripmeester, J.A., and Klug, D.D. (2006). *J. Chem. Phys.* **124**, 014704.

Alavi, S.; Susilo, R., and Ripmeester, J.A. (2009). *J. Chem. Phys.* **130**, 174501.

Als-Nielsen, J. and McMorrow, D. (2001). *Elements of Modern X-ray Physics*. John Wiley & Sons, Ltd.

Aya, I.; Yamane, K., and Nariai, H. (1997). *Energy* **22**, 263.

Barbiellini, B. and Shukla, A. (2002). *Phys. Rev. B* **66**, 235101.

Barbiellini, B.; Bellin, Ch.; Loupias, G.; Buslaps, T., and Shukla, A. (2009). *Phys. Rev. B* **79**, 155115.

Beamline ID15. URL: `http://www.esrf.eu/UsersAndScience/Experiments/StructMaterials/ID15`.

Berendsen, H.J.C.; Grigera, J.R., and Straatsma, T.P. (1987). *J. Phys. Chem.* **91**, 6269.

Bergmann, U.; Wernet, Ph.; Glatzel, P.; Cavalleri, M.; Pettersson, L.G.M.; Nilsson, A., and Cramer, S.P. (2002). *Phys. Rev. E* **66**, 092107.

Bergmann, U.; Nordlund, D.; Wernet, Ph.; Odelius, M.; Pettersson, L.G.M., and Nilsson, A. (2007*a*). *Phys. Rev. B* **76**, 024202.

Bergmann, U.; Di Cicco, A.; Wernet, Ph.; Principi, E.; Glatzel, P., and Nilsson, A. (2007*b*). *J. Chem. Phys.* **127**, 174504.

Bernal, J.D. and Fowler, R.H. (1933). *J. Chem. Phys.* **1**, 515.

Bertie, J.A. and Jacobs, S.M. (1978). *J. Chem. Phys.* **69**, 4105.

Bertrand, E.; Dobbs, H.; Broseta, D.; Indekeu, J.; Bonn, D., and Meunier, J. (2000). *Phys. Rev. Lett.* **85**, 1282.

Biggs, F.; Mendelsohn, L.B., and Mann, J.B. (1975). *Atom. Data Nucl. Data* **16**, 201.

Bonn, D. and Ross, D. (2001). *Rep. Prog. Phys.* **64**, 1085.

Boswell, R. (2009). *Science* **325**, 957.

Bowron, D.T.; Filipponi, A.; Roberts, M.A., and Finney, J.L. (1998). *Phys. Rev. Lett.* **81**, 4164.

Bowron, D.T.; Krisch, M.H.; Barnes, A.C.; Finney, J.L.; Kaprolat, A., and Lorenzen, M. (2000). *Phys. Rev. B* **62**, R9223.

Bowron, D.T.; Finney, J.L., and Soper, A.K. (2006). *J. Phys. Chem. B* **110**, 20235.

Braslau, A.; Deutsch, M.; Pershan, P.S.; Weiss, A.H.; Als-Nielsen, J., and Bohr, J. (1985). *Phys. Rev. Lett.* **54**, 114.

Braslau, A.; Pershan, P.S.; Swislow, G.; Ocko, B.M., and Als-Nielsen, J. (1988). *Phys. Rev. A* **38**, 2457.

Brewer, P.G.; Friederich, G.; Peltzer, E.T., and Orr jr., F. M. (1999). *Science* **284**, 943.

Buff, F.P.; Lovett, R.A., and jr., F.H. Stillinger (1965). *Phys. Rev. Lett.* **15**, 621.

Cai, Y.Q.; Mao, H.K.; Chow, P.C.; Tse, J.S.; Ma, Y.; Patchkovskii, S.; Shu, J.F.; Struzhkin, V.; Hemley, R.J.; Ishii, H.; Chen, C.C.; Jarrige, I.; Chen, C.T.; Shieh, S.R.; Huang, E.P., and Kao, C.C. (2005). *Phys. Rev. Lett.* **94**, 025502.

Conrad, H. (2007). "Tetrahydrofuran clathrate hydrate formation studied by X-ray Raman scattering." Diploma thesis. Technische Universität Dortmund.

Conrad, H.; Lehmkühler, F.; Sternemann, C.; Feroughi, O.; Simonelli, L.; Huotari, S., and Tolan, M. (2009*a*). *Rev. Sci. Instrum.* **80**, 026103.

Conrad, H.; Lehmkühler, F.; Sternemann, C.; Sakko, A.; Paschek, D.; Simonelli, L.; Huotari, S.; Feroughi, O.; Tolan, M., and Hämäläinen, K. (2009*b*). *Phys. Rev. Lett.* **103**, 218301.

Cooper, M.J.; Mijnarends, P.E.; Shiotani, N.; Sakai, N., and Bansil, A. (2004). *X-Ray Compton Scattering*. Oxford University Press.

Daniels, J.E. and M.Drakopoulos (2009). *J. Synch. Rad.* **16**, 463.

Davy, H. (1811). *Philos. Trans. R. Soc. London* **101**, 1.

Doerr, A.K.; Tolan, M.; Prange, W.; Schlomka, J.-P.; Seydel, T.; Press, W.; Smilgies, D., and Struth, B. (1999). *Phys. Rev. Lett.* **83**, 3470.

Dornan, P.; Alavi, S., and Woo, T.K. (2007). *J. Chem. Phys.* **127**, 124510.

Duarte, A.R.C.; Shariati, A., and Peters, C.J. (2009). *J. Chem. Eng. Data* **54**, 1628.

Durham, W.B.; Stern, L.A., and Kirby, S.H. (2003). *Can. J. Phys.* **81**, 373.

Dyadin, Y. A.; Larionov, E. G.; Manakov, A. Y.; Zhurko, F. V.; Aladko, E. Y.; Mikina, T. V., and Komarov, V. Y. (1999). *Mendeleev Commun.* **5**, 209.

Eisenberger, P. and Platzman, P.M. (1970). *Phys. Rev. A* **2**, 415.

English, N.J. and Tse, J.S. (2009). *Phys. Rev. Lett.* **103**, 015901.

Epstein, I.R. (1973). *Phys. Rev. A* **8**, 160.

Fajardo, P.; Honkimäki, V.; Buslaps, T., and Suortti, P. (1998). *Nucl. Instr. Meth. Phys. Res. B* **134**, 337.

Fan, S.; Li, S.; Wang, J.; Lang, X., and Wang, Y. (2009). *Energy Fuels* **23**, 4202.

Faraday, M. (1823). *Philos. Trans. R. Soc. London* **113**, 160.

Fischer, J.; Paschek, D.; Geiger, A., and Sadowski, G. (2008). *J. Phys. Chem. B* **112**, 2388.

Fister, T.T.; Nagle, K.P.; Vila, F.D.; Seidler, G.T.; Hamner, C.; Cross, J.O., and Rehr, J.J. (2009). *Phys. Rev. B* **79**, 174117.

Florusse, L.J.; Peters, C.J.; Schoonman, J.; Hester, K.C.; Koh, C.A.; Dec, S.F.; Marsh, K.N., and Sloan, E.D. (2004). *Science* **306**, 469.

Frenkel, J. (1946). *Kinetic Theory of Liquids*. Oxford University Press.

Fukui, H.; Huotari, S.; Andrault, D., and Kawamoto, T. (2007). *J. Chem. Phys.* **127**, 134502.

Ganji, H.; Manteghian, M., and Zadeh, K.S. (2006). *J. Chem. Eng. Jpn.* **39**, 401.

Gao, S.; Chapman, W.C., and House, W. (2005). *Ind. Eng. Chem. Res.* **44**, 7373.

Garg, S.K.; Davidson, D.W., and Ripmeester, J.A. (1974). *J. Magn. Reson.* **15**, 295.

– (1978). *J. Magn. Reson.* **31**, 399.

Ghaderi, T. (2006). "X-ray Intensity Correlation Spectroscopy from Fluid Surfaces." PhD thesis. Universität Dortmund.

Ghanty, T.K.; Staroverov, V.N.; Koren, P.R., and Davidson, E.R. (2000). *J. Am. Chem. Soc.* **122**, 1210.

Gordon, R.A.; Seidler, G.T.; Fister, T.T.; Haverkort, M.W.; Sawatzky, G.A.; Tanaka, A., and Sham, T.K. (2008). *Europhys. Lett.* **81**, 26004.

Guo, G.-J.; Zhang, Y.-G.; Zhao, Y.-J.; Refson, K., and Shan, G.H. (2004). *J. Chem. Phys.* **124**, 1542.

Guo, G.-J.; Zhang, Y.-G., and Liu, H. (2007). *J. Phys. Chem. C* **111**, 2595.

Guo, G.-J.; Zhang, Y.-G.; Li, M., and Wu, C.-H. (2008). *J. Chem. Phys.* **128**, 194504.

Guo, G.-J.; Li, M.; Zhang, Y.-G., and Wu, C.-H. (2009). *Phys. Chem. Chem. Phys.* **11**, 10427.

Gutt, C. (2001). "Methan- und Xenonhydrat. Struktur und Dynamik." Dissertation. Christian-Albrechts-Universität zu Kiel.

Gutt, C.; Asmussen, B.; Press, W.; Johnson, M. R.; Handa, Y. P., and Tse, J. S. (2000). *J. Chem. Phys.* **113**, 4713.

Gutt, C.; Baumert, J.; Press, W.; Tse, J.S., and Janssen, S. (2002). *J. Chem. Phys.* **116**, 3795.

Hakala, M.; Huotari, S.; Hämäläinen, K.; Manninen, S.; Wernet, Ph.; Nilsson, A., and Pettersson, L.G.M. (2004). *Phys. Rev. B* **70**, 125413.

Hakala, M.; Nygård, K.; Manninen, S.; Pettersson, L.G.M., and Hämäläinen, K. (2006*a*). *Phys. Rev. B* **73**, 035432.

Hakala, M.; Nygård, K.; Manninen, S.; Huotari, S.; Buslaps, T.; Nilsson, A.; Pettersson, L.G.M., and Hämäläinen, K. (2006*b*). *J. Chem. Phys.* **125**, 084504.

Hakala, M.; Nygård, K.; Vaara, J.; Itou, M.; Sakurai, Y., and Hämäläinen, K. (2009). *J. Chem. Phys.* **130**, 034506.

Halsey, G.D. (1948). *J. Chem. Phys.* **16**, 931.

Hämäläinen, K. and Manninen, S. (2001). *J. Phys.: Condens. Matter* **13**, 7539.

Hammer, B.; Hansen, L.B., and Nøorskov, J.K. (1999). *Phys. Rev. B* **59**, 7413.

Hammerschmidt, E.G. (1934). *Industrial and Engeneering Chemistry* **26**, 851.

Hart, R.T.; Mei, Q.; Benmore, C.J.; Neuefeind, J.C.; Turner, J.C.F.; Dolgos, M.; Tomberli, B., and Egelstaff, P.A. (2006). *J. Chem. Phys.* **124**, 134505.

Hawtin, R.W.; Quigley, D., and Rodger, P.M. (2008). *Phys. Chem. Chem. Phys.* **10**, 4853.

Head-Gordon, T. and Johnson, M.E. (2006). *PNAS* **103**, 7973.

Heilmann, R.K.; Fukuto, M., and Pershan, P.S. (2001). *Phys. Rev. E* **63**, 205405.

Hermann, K. and et al. STOBE-DEMON *version 3.0*. URL: `http://w3.rz-berlin.mpg.de/~hermann/StoBe/index.html`.

Hester, K.C.; Strobel, T.A.; Sloan, E.D.; Koh, C.A.; Huq, A., and Schultz, A.J. (2006). *J. Phys. Chem.* **110**, 14024.

Hester, K.C.; Huo, Z.; Ballard, A.L.; Koh, C.A.; Miller, K.T., and Sloan, E.D. (2007). *J. Phys. Chem. B* **111**, 8830.

Hill, T.L. (1949). *J. Chem. Phys.* **17**, 590.

Hirai, S.; Okazaki, K.; Tabe, Y., and Kawamura, K. (1997). *Energy Convers. Manage.* **38**, S301.

Hiraoka, N.; Buslaps, T.; Honkimäki, V., and Suortti, P. (2005). *J. Synch. Rad.* **12**, 670.

Hohenberg, P. and Kohn, W. (1964). *Phys. Rev.* **136**, B864.

Holm, P. (1988). *Phys. Rev. A* **37**, 3706.

Holm, P. and Ribberfors, R. (1989). *Phys. Rev. A* **40**, 6251.

Honkimäki, V. and Suortti, P. (2007). *J. Synch. Rad.* **14**, 331.

Honkimäki, V.; Reichert, H.; Okasinski, J. S., and Dosch, H. (2006). *J. Synch. Rad.* **13**, 426.

House, K.Z.; Schrag, D.P.; Harvey, C.F., and Lackner, K.S. (2006). *PNAS* **103**, 12291.

Huotari, S.; Hämäläinen, K.; Manninen, S.; Issolah, A., and Marangolo, M. (2001). *J. Phys. Chem. Solids* **62**, 2205.

Huotari, S.; Boldrini, B.; Honkimäki, V.; Suortti, P., and Weyrich, W. (2009). *J. Synch. Rad.* **16**, 672.

Ibach, H. and Lüth, H. (2002). *Festkörperphysik*. Springer.

Isaacs, E.D.; Shukla, A.; Platzman, P.M.; Hamann, D.R.; Barbiellini, B., and Tulk, C.A. (1999). *Phys. Rev. Lett.* **82**, 600.

– (2000). *J. Phys. Chem. Solid* **61**, 403.

Israelachvili, J. (2000). *Intermolecular & Surface Forces*. Academic Press Inc.

Issolah, A.; Garreau, Y.; Lévy, B., and Loupias, G. (1991). *Phys. Rev. B* **44**, 11029.

Jacobs, D.M.; Zeidler, M.D., and Kanert, O. (1997). *J. Phys. Chem. A* **101**, 5241.

Jacobson, L. C.; Hujo, W., and Molinero, V. (2009). *J. Phys. Chem B* **113**, 10298.

Jeffrey, G. A. (1984). *J. Inclusion Phenom.* **1**, 211.

Jones, C.Y.; Marshall, S.L.; Chakoumakos, B.C.; Rawn, C.J., and Ishii, Y. (2003). *J. Phys. Chem. B* **107**, 6026.

Jones, R. O. and Gunnarsson, O. (1989). *Rev. Mod. Phys.* **61**, 689.

Jorgensen, W.L.; Maxwell, D.S., and Tirado-Rives, J. (1996). *J. Am. Chem. Soc.* **118**, 11225.

Kakutani, Y. and Sakai, N. (2004). *J. Phys. Chem. Solids* **65**, 2071.

Kang, S. P. and Lee, H. (2000). *Environ. Sci. Technol.* **34**, 4397.

Kiessig, H. (1931). *Ann. Phys.* **402**, 769.

Klapproth, A. (2002). "Strukturuntersuchungen an Methan- und Kohlenstoffdioxid-Clathrat-Hydraten." Dissertation. Georg-August-Universität zu Göttingen.

Klauda, J.B. and Sandler, S.I. (2005). *Energy Fuels* **19**, 459.

Koh, C. A. (2002). *Chem. Soc. Rev.* **31**, 157.

Koh, C.A.; Savidge, J.L., and Tang, C.C. (1996). *J. Phys. Chem.* **100**, 6412.

Koh, C.A.; Wisbey, R.P.; Wu, X.; Westacott, R.E., and Soper, A.K (2000). *J. Chem. Phys.* **113**, 6390.

Kohn, W. and Sham, L.J. (1965). *Phys. Rev.* **140**, A1133.

Koza, M.M.; Geil, B.; Winkel, K.; Kohler, C.; Czeschka, F.; Scheuermann, M.; Schober, H., and Hansen, T. (2005). *Phys. Rev. Lett.* **94**, 125506.

Krisch, M.H.; Sette, F.; Masciovecchio, C., and Verbeni, R. (1997). *Phys. Rev. Lett.* **78**, 2843.

Krywka, C.; Sternemann, C.; Paulus, M.; Javid, N.; Winter, R.; Al-Sawalmih, A.; Yi, S.; Raabe, D., and Tolan, M. (2007). *J. Synch. Rad.* **14**, 244.

Kuhs, W.F.; Finney, J.L.; Vettier, C., and Bliss, D.V. (1984). *J. Chem. Phys.* **81**, 3612.

Kvamme, B. (2000). *Annals of the New York Academy of Science* **912**, 496.

Larson, M.A. and Garside, J. (1986). *Chem. Eng. Sci.* **41**, 1285.

Leaist, D.G.; Murray, J.J.; Post, M.L, and Davidson, D.W. (1982). *J. Phys. Chem.* **86**, 4175.

Lee, H.; Seo, Y.; Seo, Y.-T.; Moudrakovski, I.L., and Ripmeester, J.A. (2003). *Angew. Chem. Int. Ed.* **42**, 5048.

Lee, H.; Lee, J.; Kim, D.Y.; Park, J.; Seo, Y.; Zeng, H.; Moudrakovski, I.L.; Ratcliffe, C.I., and Ripmeester, J.A. (2005). *Nature* **434**, 743.

Li, M. and Schlossman, M.L. (2002). *Phys. Rev. E* **65**, 061608.

Li, M.; Tikhonov, A.M.; Chaiko, D.J., and Schlossman, M.L. (2001). *Phys. Rev. Lett.* **86**, 5934.

Lide, D.R., ed. (2003–2004). *Handbook of Chemistry and Physics*. 84th ed. Taylor & Francis.

Lietz, D. (2007). "Hochenergiereflektometrie an Festkörper-Gas und Festkörper-Flüssigkeits-Grenzflächen." Diploma thesis. Universität Dortmund.

Lindahl, E.; Hess, B., and van der Spoel, D. (2001). *J. Mol. Model.* **7**, 306.

Loerting, T.; Salzmann, C.; Kohl, I.; Mayer, E., and Hallbrucker, A. (2001). *Phys. Chem. Chem. Phys.* **3**, 5355.

Loerting, T.; Schustereder, W.; Winkel, K.; Salzmann, C.G.; Kohl, I., and Mayer, E. (2006). *Phys. Rev. Lett.* **96**, 025702.

Löwdin, P.-O. (1955). *Phys. Rev.* **97**, 1474.

Makino, T.; Sugahara, T., and Ohgaki, K. (2005). *J. Chem. Eng. Data* **50**, 2058.

Makogon, Y.F. (1965). *Gazov. Promst.* **5**, 14.

Manninen, S.; Paakkari, T., and Halonen, V. (1977). *Chem. Phys. Lett.* **46**, 62.

Mao, W. L.; Mao, H.; Goncharov, A. F.; Struzhkin, V. V.; Guo, Q.; Hu, J.; Shu, J.; Hemley, R. J.; Somayazulu, M., and Zhao, Y. (2002). *Science* **297**, 2247.

Marques, M.A.L.; Ullrich, C.A.; Nogueira, F.; Rubio, A.; Burke, K., and Gross, E.K.U., eds. (2006). *Time-Dependent Density Functional Theory*. Springer.

Martin, R.M. (2004). *Electronic Structure*. Cambridge University Press.

Mattila, A.; Soininen, J.A.; Galambosi, S.; Huotari, S.; Vankó, G.; Zhigadlo, N.D.; Karpinski, J., and Hämäläinen, K. (2005). *Phys. Rev. Lett.* **94**, 247003.

Max, M. D., ed. (2000). *Natural Gas Hydrates in Oceanic and Permafrost Environments*. Kluwer Academic Publishers.

May, E.F.; Moldover, M.R., and Schmidt, J.W. (2005). *Int. J. Thermophys.* **26**, 563.

Mizuno, Y. and Ohmura, Y. (1967). *J. Phys. Soc. Jpn.* **22**, 445.

Moon, C.; Taylor, P.C., and Rodger, P.M. (2003). *J. Am. Chem. Soc.* **125**, 4706.

Morgan, J.J.; Blackwell, V.R.; Johnson, D.E., and North, D.F. Spencer W.J. (1999). *Environ. Sci. Technol.* **33**, 1448.

Mulder, F.M.; Wagemaker, M.; Eijck, L. van, and Kearley, G.J. (2008). *Chem. Phys. Chem.* **9**, 1331.

Nagasawa, H.; Mourikis, S., and Schulke, W. (1997). *J. Phys. Soc. Jpn.* **66**, 3139.

Nayak, J.N.; Aralaguppi, M.I.; Kumar Naidu, B.V., and Aminabhavi, T.M. (2004). *J. Chem. Eng. Data* **49**, 468.

Nilsson, A.; Wernet, Ph.; Nordlund, D.; Bergmann, U.; Cavalleri, M; Odelius, M.; Ogasawara, H.; Näslund, L. Å.; Hirsch, T.; Ojamäe, L., and Nilsson, A. (2005). *Science* **308**, 793a.

NIST Chemistry WebBook. URL: `http://webbook.nist.gov/chemistry/`.

NIST XCOM. URL: `http://physics.nist.gov/PhysRefData/Xcom/html/xcom1.html`.

Nolas, G.S.; Cohn, J.L.; Slack, G.A., and Schujman, S.B. (1998). *Appl. Phys. Lett.* **73**, 178.

Nowaczyk, A.; Geil, B.; Schildmann, S., and Böhmer, R. (2009). *Phys. Rev. B* **80**, 144303.

Nygård, K.; Hakala, M.; Manninen, S.; Hämäläinen, K.; Itou, M.; Andrejczuk, A., and Sakurai, Y. (2006*b*). *Phys. Rev. B* **73**, 024208.

Nygård, K.; Hakala, M.; Manninen, S.; Andrejczuk, A.; Itou, M.; Sakurai, Y.; Pettersson, L.G.M., and Hämäläinen, K. (2006*a*). *Phys. Rev. E* **74**, 031503.

Nygård, K.; Hakala, M.; Manninen, S.; Itou, M.; Sakurai, Y., and Hämäläinen, K. (2007*a*). *Phys. Rev. Lett.* **99**, 197401.

Nygård, K.; Hakala, M.; Pylkkänen, T.; Manninen, S.; Buslaps, T.; Itou, M.; Andrejczuk, A.; Sakurai, Y.; Odelius, M., and Hämäläinen, K. (2007*b*). *J. Chem. Phys.* **126**, 154508.

Ogata, K.; Hashimoto, S.; Sugahara, T.; Moritoki, M.; Sato, H., and Ohgaki, K. (2008). *Chem. Eng. Sci.* **63**, 5714.

Ohmura, R.; Kashiwazaki, S.; Shiota, S.; Tsuji, H., and Mori, Y.H. (2002). *Energy Fuels* **16**, 1141.

Oleinikova, A. and Weingärtner, H. (2000). *Chem. Phys. Lett.* **319**, 119.

Paakkari, T. (1978). *Chem. Phys. Lett.* **55**, 160.

Papadimitriou, N. I.; Tsimpanogiannis, I. N.; Peters, C. J.; Papaioannou, A. Th., and Stubos, A. K. (2008). *Mendeleev Commun.* **112**, 14206.

Park, Y.; Kim, D.-Y.; Lee, J.-W.; Huh, D.-G.; Park, K.-P.; Lee, J., and Lee, H. (2006). *PNAS* **103**, 12690.

Parratt, L.G. (1954). *Phys. Rev.* **95**, 359.

Paschek, D. (2005). *MOSCITO4 molecular dynamics simulation package*. http://ganter.chemie.uni-dortmund.de/MOSCITO.

– (2008). *private communication*.

Pauling, L. (1935). *J. Am. Chem. Soc.* **57**, 2680.

Paulus, M. (2006). "Röntgenstreuung an Flüssigkeits-Gas Grenzflächen." PhD thesis. Universität Dortmund.

Paulus, M.; Gutt, C., and Tolan, M. (2005). *Phys. Rev. E* **72**, 061601.

Paulus, M.; Lietz, D.; Sternemann, C.; Shokuie, K.; Evers, F.; Tolan, M.; Czeslik, C., and Winter, R. (2008*b*). *J. Synch. Rad.* 15, 600.

Paulus, M.; Gutt, C., and Tolan, M. (2008*c*). *Surf. Interface Anal.* **40**, 1226.

– (2008*a*). *Phys. Rev. B* **78**, 235419.

Perdew, J.P.; Burke, K., and Ernzerhof, M. (1996). *Phys. Rev. Lett.* **77**, 3865.

Poudrix Powder X-ray and Neutron Pattern Calculation Software. URL: `http://www.ccp14.ac.uk/ccp/web-mirrors/lmgp-laugier-bochu/`.

Prasad, P.S.R.; Shiva Prasad, K., and Thakur, N.K. (2007). *Spectrochim. Acta, Part A* **68**, 1096.

Prendergast, D. and Galli, G. (2006). *Phys. Rev. Lett.* **96**, 215502.

Pylkkänen, T.; Giordano, V.M.; Chervin, J.C.; Sakko, A.; Hakala, M.; Soininen, J.A.; Hämäläinen, K.; Monaco, G., and Huotari, S. (2010). *J. Phys. Chem. B* **114**, 3804.

Radhakrishnan, R. and Trout, B.L. (2002). *J. Chem. Phys.* **117**, 1786.

Ragot, S.; Gillet, J.M., and Becker, P.J. (2002). *Phys. Rev. B* **65**, 235115.

Rawn, C. J.; Rondinone, A. J.; Chakoumas, B. C.; Circone, S.; Stern, L. A.; Kirby, S. H., and Ishii, Y. (2003). *Can. J. Phys.* **81**, 431.

Reichert, H.; Honkimäki, V.; Snigirev, A.; Engemann, S., and Dosch, H. (2003). *Physica B* **336**, 46.

Ribberfors, R. (1975*a*). *Phys. Rev. B* **12**, 2067.

– (1975*b*). *Phys. Rev. B* **12**, 3136.

Ripmeester, J.A. and Ratcliffe, C.I. (1990). *J. Phys. Chem.* **94**, 8773.

Ripmeester, J.A.; Tse, J.S; Ratcliffe, C.I., and Powell, B.M. (1987). *Nature* **325**, 135.

Ripmeester, J.A.; Ratcliffe, C.I., and Cameron, I.G. (2004). *J. Phys. Chem. B* **108**, 929.

Rodger, P.M. (1990). *J. Phys. Chem.* **94**, 6080.

Runge, E. and Gross, E.K.U (1984). *Phys. Rev. Lett.* **52**, 997.

Sakko, A. and Hakala, M. (2009–2010). *private communication*.

Sakko, A.; Hakala, M.; Soininen, J.A., and Hämäläinen, K. (2007). *Phys. Rev .B* **76**, 205115.

Salzmann, C.G.; Radaelli, P.G.; Mayer, E., and Finney, J.L. (2009). *Phys. Rev. Lett.* **103**, 105701.

Schicks, J. (2008). *Chem. Unserer Zeit* **42**, 310.

Schülke, W. (1991). "Inelastic scattering by electronic excitations."*Handbook on Synchrotron Radiation*. Ed. by Brown, G.S. and Moncton, D.E. North-Holland.

– (2007). *Electron Dynamics by Inelastic X-ray Scattering*. Oxford University Press.

Seth, A. and Baerends, E. J. (1979). *Chem. Phys. Lett.* **64**, 165.

Seth, A. and Baerends, E.J. (1977). *Chem. Phys. Lett.* **52**, 248.

Shokuie, K.; Paulus, M.; Sternemann, C.; Fendt, R., and Tolan, M. (2007). *Thin Solid Films* **515**, 5660.

Shukla, A.; Isaacs, E.D.; Hamann, D.R., and Platzman, P.M. (2001). *Phys. Rev. B* **64**, 052101.

Sinha, S.K.; Sirota, E.B.; Garoff, S., and Stanley, H.B. (1988). *Phys. Rev. B* **38**, 2297.

Sit, P.H.-L.; Bellin, Ch.; Barbiellini, B.; Testemale, D.; Hazemann, J.-L.; Buslaps, T.; Marzari, N., and Shukla, A. (2007). *Phys. Rev. B* **76**, 245413.

Sloan, E.D. (2003). *Nature* **426**, 353.

Sloan, E.D. and Fleyfel, F. (1991). *AIChE J.* **37**, 1281.

Sloan, E.D. and Koh, C.A. (2008). *Clathrate Hydrates of Natural Gases*. 3rd ed. CRC Press Inc.

Smith, H.J.; Fahrenkamp-Uppenbrink, J., and Coontz, R. et al. (2009). *Science* **325**, 1641–1652.

Smith, J.D.; Cappa, C.D.; Wilson, K.R.; Messer, B.M.; Cohen, R.C., and Saykally, R.J. (2004). *Science* **306**, 851.

Smith, J.D.; Cappa, C.D.; Messer, B.M.; Cohen, R.C., and Saykally, R.J. (2005). *Science* **308**, 793b.

Soininen, J. A.; Mattila, A.; Rehr, J. J.; Galambosi, S., and Hämäläinen, K. (2006). *J. Phys.: Condens. Matter* **18**, 7327.

Soininen, J.A.; Ankudinov, A.L., and Rehr, J.J. (2005). *Phys. Rev. B* **72**, 045136.

Staykova, D.K.; Kuhs, W.F.; Salamatin, A.N., and Hansen, T. (2003). *J. Phys. Chem. B* **107**, 10299.

Sternemann, C. (2000). "Final state interaction and temperature effects in Compton scattering from lithium." PhD thesis. Universität Dortmund.

Sternemann, C.; Hämäläinen, K.; Kaprolat, A.; Soininen, A.; Döring, G.; Kao, C.-C.; Manninen, S., and Schülke, W. (2000). *Phys. Rev. B* **62**, R7687.

Sternemann, C.; Volmer, M.; Soininen, J.A.; Nagasawa, H.; Paulus, M.; Enkisch, H.; Schmidt, G.; Tolan, M., and Schülke, W. (2004). *Phys. Rev. B* **68**, 035111.

Sternemann, C.; Huotari, S.; Hakala, M.; Paulus, M.; Volmer, M.; Gutt, C.; Buslaps, T.; Hiraoka, N.; Klug, D.D.; Hämäläinen, K.; Tolan, M., and Tse, J.S. (2006). *Phys. Rev. B* **73**, 195104.

Sternemann, C.; Sternemann, H.; Huotari, S.; Lehmkühler, F.; Tolan, M., and Tse, J.S. (2008*a*). *J. Anal. At. Spectrom.* **23**, 807.

Sternemann, H. (2008). "A non-resonant inelastic x-ray scattering study on silicon oxides and clathrates." Dissertation. Technische Universität Dortmund.

Sternemann, H.; Sternemann, C.; Tse, J.S.; Desgreniers, S.; Cai, Y.Q.; Vankó, G.; Hiraoka, N.; Schacht, A.; Soininen, J.A., and Tolan, M. (2007). *Phys. Rev. B* **75**, 245102.

Sternemann, H.; Sternemann, C.; Seidler, G.T.; Fister, T.T.; Sakko, A., and Tolan, M. (2008*b*). *J. Synch. Rad.* **15**, 162.

Strobel, T. A.; Koh, C. A., and Sloan, E. D. (2008). *J. Phys. Chem. B* **112**, 1885.

Strobel, T.A.; Taylor, C.J.; Hester, K.C.; Dec, S.F.; Koh, C.A.; Miller, K.T., and Sloan, E.D. (2006). *J. Phys. Chem. B* **110**, 17121.

Struzhkin, V.V.; Militzer, B.; Mao, W.L.; Mao, H., and Hemley, R.J. (2007). *Chem. Rev.* **107**, 4133.

Stubbs, J.M.; Potoff, J.J., and Siepmann, J.I. (2004). *J. Phys. Chem. B* **108**, 17596.

Sugahara, T.; Haag, J.C.; Prasad, P.S.R.; Warntjes, A.A.; Sloan, E.D.; Sum, A.K., and Koh, C.A. (2009). *J. Am. Chem. Soc.* **131**, 14616.

Suortti, P. and Schulze, C. (1995). *J. Synch. Rad.* **2**, 6.

Suortti, P.; Buslaps, T.; Fajardo, P.; Honkimäki, V.; Kretzschmer, M.; Lienert, U.; McCarthy, J. E.; Renier, M.; Shukla, A.; Tschentscher, Th., and Meinander, T. (1999). *J. Synch. Rad.* **6**, 69.

Susilo, R.; Alavi, S.; Moudrakovski, I.L.; Englezos, P., and Ripmeester, J.A. (2009). *Chem. Phys. Chem.* **10**, 824.

Suzuki, T. (1967). *J. Phys. Soc. Jpn.* **22**, 1139.

Takeya, S.; Hori, A.; Hondoh, T., and Uchida, T. (2000). *J. Phys. Chem. B* **104**, 4164.

Takeya, S.; Kida, M.; Minami, H.; Sakagami, H.; Hachikubo, A.; Takahashi, N.; Shoji, H.; Soloviev, V.; Wallmann, K.; Biebow, N.; Obzhirov, A.; Salomatin, A., and Poort, J. (2006). *Chem. Eng. Sci.* **61**, 2670.

Takeya, S.; Honda, K.; Kawamura, T.; Yamamoto, Y.; Yoneyama, A.; Hirai, Y.; Hyodo, K., and Takeda, T. (2007). *Appl. Phys. Lett.* **90**, 081920.

Tanaka, H.; Tamai, Y., and Koga, K. (1997). *J. Phys. Chem. B* **101**, 6560.

Teng, H.; Yamasaki, A., and Shino, Y. (1999). *Int. J. Energy Res.* **23**, 295.

Thompson, H.; Soper, A.K.; Buchanan, P.; Aldiwan, N.; Creek, J.L., and Koh, C.A. (2006). *J. Chem. Phys.* **124**, 164508.

Tolan, M. (1999). *X-ray Scattering from Soft Matter Thin Films*. Springer.

Tombari, E.; Presto, S.; Salvetti, G., and Johari, G.P. (2006). *J. Chem. Phys.* **124**, 154507.

Tribello, G. A. and Slater, B. (2009). *J. Chem. Phys.* **131**, 024703.

Triguero, L.; Pettersson, L.G.M., and Ågren, H. (1998). *Phys. Rev. B* **58**, 8097.

Tse, J.S. (1987). *J. De Physique* **48**, 543.

Tse, J.S.; Shpakov, V.P.; Belosludov, V.R.; Trouw, F.; Handa, Y.P., and Press, W. (2001). *Europhys. Lett.* **54**, 354.

Tse, J.S.; Shaw, D.M.; Klug, D.D.; Patchkovskii, S.; Vankó, G.; Monaco, G., and Krisch, M. (2008). *Phys. Rev. Lett.* **100**, 095502.

Tuan, D.Q. and Ilangantileke, S.G. (1997). *J. Food Engeneering* **31**, 47.

Uchida, T. (1997). *Waste Management* **17**, 343.

Uchida, T.; Ebinuma, T., and Narita, H. (2000). "Laboratory studies on the formation and dissociation processes of CO_2-hydrate crystals - measurements of interfacial tension between CO_2 and water."*Proceedings of the International Symposium on Deep Sea Sequestration of CO_2*, 1–4–1.

Udachin, K. A.; Ratcliffe, C. I.; Enright, G. D., and A., Ripmeester J. (1997). *Supramol. Chem.* **8**, 173.

Udachin, K.A.; Ratcliffe, C.I., and Ripmeester, J.A. (2001). *J. Phys. Chem. B* **105**, 4200.

van den Berg, A.W.C. and Areán, C.O. (2008). *Chem. Commun.* **13**, 668.

van der Waals, J.H. and Platteeuw, J.C. (1959). *Adv. Chem. Phys.* **2**, 1.

van Hove, L. (1954). *Phys. Rev.* **95**, 249.

Vatamanu, J. and Kusalik, P.G. (2006). *J. Am. Chem. Soc.* **128**, 15588.

Verbeni, R.; Pylkkänen, T.; Huotari, S.; Simonelli, L.; Vankó, G.; Martel, K.; Henriquet, C., and Monaco, G. (2009). *J. Synch. Rad.* **16**, 469.

VMD Visual Molecular Dynamics. URL: `http://www.ks.uiuc.edu/Research/vmd/`.

Volmer, M. (2006). "Compton Scattering on Complex Materials - an investigation on the electronic structure of alkali-metak doped S-clathrates." PhD thesis. Universität Dortmund.

von Stackelberg, M. (1949). *Naturwissenschaften* **36**, 327.

von Stackelberg, M. and Jahns, W. (1954). *Z. Electrochemie* **58**, 162.

von Stackelberg, M. and Müller, H.R. (1951*b*). *J. Chem. Phys.* **19**, 1319.

– (1951*a*). *Naturwissenschaften* **38**, 456.

– (1954). *Z. Electrochemie* **58**, 25.

Waite, W.F.; Gilbert, L.Y.; Winters, W.J., and Mason, D.H. (2005). *Proceedings of the Fifth International Conference on Gas Hydrates*, 1725.

Walsh, M.R.; Koh, C.A.; Sloan, E.D.; Sum, A.K., and Wu, D.T. (2009). *Science* **326**, 1095.

Wernet, Ph.; Nordlund, D.; Bergmann, U.; Ogasawara, H.; Cavalleri, M; Näslund, L. Å.; Hirsch, T.; Ojamäe, L.; Glatzel, P.; Odelius, M.; Pettersson, L. G. M., and Nilsson, A. (2004). *Science* **304**, 995.

Wernet, Ph.; Testemale, D.; Hazemann, J.-L.; Argoud, R.; Glatzel, P.; Pettersson, L.G.M.; Nilsson, A., and Bergmann, U. (2005). *J. Chem. Phys.* **123**, 154503.

Whangbo, M.H.; Jr., V.H. Smith; Clementi, E.; Diercksen, G.H., and von Niessen, W. (1974). *J. Phys. B: Atom. Molec. Phys.* **7**, L427.

Wikipedia. URL: `http://en.wikipedia.org/`.

Williams, B.G.; Felsteiner, J.; Halonen, V.; Paakkari, T.; Manninen, S.; Reed, W.; Eisenberger, P.; Weiss, R.; Pattison, P., and Cooper, M. (1976). *Acta. Cryst.* **A32**, 513.

Yang, L.; Tulka, C. A.; Klug, D. D.; Moudrakovski, I. L.; Ratcliffe, C. I.; Ripmeester, J. A.; Chakoumakos, B. C.; Ehm, L.; Martin, C. D., and Parise, J. B. (2009). *Proc. Natl. Acad. Sci.* **106**, 6060.

Yaws, C.L. (1987). *The Properties of gases and liquids*. McGraw-Hill.

Yokohama, H.; Kannami, M., and Kanno, H. (2008). *Chem. Phys. Lett.* **463**, 99.

Yoon, J.; Kawamura, T.; Yamamoto, Y., and Komai, T. (2004). *J. Phys. Chem. A* **108**, 5057.

Zhang, J.; Hawtin, R.W.; Yang, Y.; Nakagava, E.; Rivero, M.; Choi, S.K., and Rodger, P.M. (2008). *J. Phys. Chem. B* **112**, 10608.

Zhou, X.; Fan, S.; Liang, D., and Du, J. (2008). *Energy Fuels* **22**, 1759.

Publications

Refereed articles

- Lehmkühler, F., Paulus, M., Streit-Nierobisch, S., and Tolan, M. (2008). *Determination of microscopic interaction constants by x-ray reflectivity measurements*, Fluid Phase Equib. **268**, 95.

- Sternemann, C., Sternemann, H., Huotari, S., Lehmkühler, F., Tolan, M., and Tse, J. S. (2008). *The barium giant dipole resonance in barite: a study of soft X-ray absorption edges using hard X-rays*. J. Anal. At. Spectrom. **23**, 807.

- Lehmkühler, F., Paulus, M., Sternemann, C., Lietz, D. Venturini, F., Gutt, C., Tolan, M. (2009). *The carbon dioxide-water interface at conditions of gas hydrate formation*. J. Am. Chem. Soc. **131**, 585.

- Conrad, H., Lehmkühler, F., Sternemann, C., Feroughi, O., Simonelli, L. Huotari, S., and Tolan, M. (2009). *A sample cell to study hydrate formation with x-ray scattering*. Rev. Sci. Instrum. **80**, 026103.

- Conrad, H., Lehmkühler, F., Sternemann, C., Sakko, A., Paschek, D., Simonelli, L. Huotari, S., Feroughi, O., Tolan, M., and Hämäläinen, K. (2009). *Tetrahydrofuran clathrate hydrate formation*. Phys. Rev. Lett. **103**, 218301.

- Doering, S., Schönbohm, F., Weier, D., Lehmkühler, F., Berges, U., Tolan, M., Fadley, C.S., and Westphal, C. (2009) *Standing-wave excited photoemission experiments on Si/ $MoSi_2$ multilayer mirrors in the soft x-ray regime: an analytical modeling approach*. J. Appl. Phys. **106**, 124906.

- Sternemann, H., Sternemann, C., Huotari, S., Lehmkühler, F., Desgreniers, S., Yamanaka, S., Maekawa, S., Sahle, Ch. J., Tolan, M., and Tse, J. S. (2010). *Modulation of the Ba 4d – f giant dipole resonance in complex Ba/Si compounds*. Phys. Rev. B. *submitted*.

Miscellaneous

- Lehmkühler, F., Paulus, M., Sternemann, C., Lietz, D. Venturini, F., Gutt, C., Tolan, M. (2010). *Revealing the hydrate formation process at the water-CO_2 interface*, ESRF Highlights 2009, 37.

Acknowledgments

First, I would like to thank my supervisors Dr. Michael Paulus and Dr. Christian Sternemann for many ideas and discussions and the invaluable support during the last years. Both have become good friends for me. I am very grateful to Prof. Dr. Metin Tolan for the possibility to write the thesis and the long-standing support since the start of my studies.

For many discussions during the trips to Dortmund and Helsinki and the performance of a myriad of DFT calculations I thank Arto Sakko and Dr. Mikko Hakala. Furthermore, I am grateful for Prof. Dr. Keijo Hämäläinen for discussion on a lot of physics and non-physics and his enthusiasm in setting-up Compton experiments.

I thank Dr. Dietmar Paschek for performing the MD simulations and answering every of my and the reviewer's questions.

I am indebted to "my" diploma students Heiko Conrad and Ingo Steinke for designing sample cells and providing the XRS data.

Since most of the experiments shown in this thesis were performed at the ESRF, I thank Dr. Federica Venturini, Dr. Thomas Buslaps, Dr. Diego Pontoni, Dr. Sebastian Schöder, and Dr. Veijo Honkimäki for support at ID15, and Dr. Laura Simonelli and Dr. Simo Huotari for support at ID16. Experiments at synchrotron facilities require the help of many other people. Here, I am grateful to Dr. Christian Sternemann, Dr. Michael Paulus, Dr. Kim Nygård, Dr. Szabolcs Galambosi, Lars Böwer, Sebastian Tiemeyer, Heiko Conrad, Christoph Sahle, Daniela Lietz, Omid Feroughi, Alexander Nyrow, Ingo Steinke, and Prof. Dr. Keijo Hämäläinen for support at various beamtimes in Grenoble and Dortmund.

I thank Dr. Kim Nygård for introducing me to the analysis of Compton scattering data and providing the Compton data on water and ice. Moreover, I am grateful to Tuomas Pylkkänen for discussions on XRS of water systems and comments to the XRS paper, Dr. Christian Gutt for many ideas on CO_2 hydrates, and Dr. Saman Alavi for providing distorted hydrate structures and calculations of heat capacities.

I am thankful to the construction design and the mechanical workshop at the physics department in Dortmund for design and construction of the high pressure and THF sample cells.

Dr. Christian Sternemann, Dr. Michael Paulus, Nils Wolf, Dr. Julia Nase, and Arto Sakko are gratefully acknowledged for proof-reading this thesis and their hints how a perfect comma

placement is "yielded". For financial support I thank the BMBF, DFG, and DAAD.

Beyond science, I am very grateful for the pleasant atmosphere at the chair E1. I thank in particular all my office mates during the last four years, Dr. Kaveh Shokuie, Andreas Schacht, Florian Evers, and Ingo Steinke for many discussions on fruitful topics. Pardon me for keeping you from work.

A special thank is dedicated to Marcel Arlt whose enthusiasm for the diploma in physics was the reason for me to do the same.

I thank my parents and family for support including woolen socks perfectly suited for the winter time in Helsinki and as much "Frikadellen" as I liked. I do not thank Belgians for brewing beer.

Finally, I am grateful to Katharina for support in nearly every circumstance in the past years. I thank C for being an inspiration during the last months.

Eidesstattliche Erklärung

Hiermit erkläre ich an Eides Statt, dass die vorliegende Dissertation – abgesehen von der Beratung durch meine wissenschaftlichen Betreuer – nach Form und Inhalt meine eigene Arbeit ist. Sie wurde weder ganz noch in Teilen an anderer Stelle im Rahmen eines Prüfungsverfahrens vorgelegt. Frühere Promotionsversuche wurden von mir nicht vorgenommen.

Dortmund, März 2010

(Felix Lehmkühler)